Technische Universität München
Fakultät für Chemie

Micro-scale NMR-spectroscopy using quantum-sensors in diamond

Fleming Paul Bruckmaier

Vollständiger Abdruck der von der Fakultät für Chemie der Technischen Universität München zur Erlangung eines

Doktors der Naturwissenschaften

genehmigten Dissertation.

Vorsitz: Prof. Dr. Steffen J. Glaser

Prüfer*innen der Dissertation:

1. TUM Junior Fellow Dr. Dominik Bucher
2. apl. Prof. Dr. Martin Brandt

Die Dissertation wurde am 02.09.2022 bei der Technischen Universität München eingereicht und durch die Fakultät für Chemie am 21.09.2022 angenommen.

TECHNICAL UNIVERSITY OF MUNICH

DEPARTMENT OF CHEMISTRY

CHAIR OF PHYSICAL CHEMISTRY I

Micro-scale NMR-spectroscopy using quantum-sensors in diamond

Fleming P. Bruckmaier

Munich 2022

Abstract

Nuclear magnetic resonance spectroscopy (NMR) is a widely used, non-invasive technique for the quantitative analysis of chemical samples. Furthermore, it forms the basis for a wide range of medical applications such as magnetic resonance imaging (MRI). In spite of decades of efforts, the technique is still limited by its inherently low sensitivity, constraining sample volumes to the range of 100 μl and the spatial resolution of MRI to tens of μm. One solution to circumvent this problem is the use of quantum properties of spin defects such as the nitrogen vacancy (NV) center in diamond. The high spatial resolution of NMR-experiments can reach spatial resolutions down to $\sim$1 μm enabling detailed NMR-imaging experiments of micro-structures, such as biological tissues or microfluidics. In this thesis, the first proof of principle NV-pulsed field gradient (PFG) experiments conducted by me are described. These mark a major step in understanding the fundamental mechanics of particle-transport at the micron-scale and form the basis for MRI using NV-doped diamonds. To be able to conduct these experiments a new NMR-setup had to be developed, including a superconducting magnet for higher magnetic field homogeneity, the necessary gradient-coils for the experiments themselves as well as a software frontend and backend for the communication and synchronisation of all the devices involved in the experiment. To better understand NV-NMR and especially NV-PFG experiments I created a code basis for their simulation with arbitrary sample volumes. Using the insight gained from these simulations I was able to demonstrate novel applications of magnetic field gradients in NV-NMR, enhancing the signal amplitude by a factor of $\sim$ 1.4 and enabling NV-NMR for diamond-cuts previously thought unusable.

Contents

Part I.

Introduction and Overview

1. Introduction

Since antiquity, people have tried to understand the world surrounding them, looking at the stars and building sophisticated models to predict their movements. Until today, one of the major tasks of research in Physics is describing the natural laws governing our universe. The importance of this can't be underestimated and has led to recent major discoveries, such as the first images of black holes,[1,2] the detection of gravitational waves[3] or the detection of the Higgs boson.[4]

While these milestones of basic research are among the major achievements in science within this century, they would have been impossible, without a continuous effort to build and improve modern sensors. In the cases mentioned above, sensors are multi-billion Euro projects like CERN, near Geneva in Switzerland, where the Higgs-boson was discovered[4] or the Laser Interferometer Gravitational-Wave Observatory (LIGO) in the United States, who were the first to announce the detection of gravitational waves.[3] Although the same improvements in sensitivity and resolution occurred in sensor-development to aid the research in the other natural sciences. Not only the scientific disciplines benefited from these developments, also our everyday life is heavily impacted by these technologies. One example is the plethora of different sensors used in each of our smart phones, ranging from gyroscopes, temperature sensors and magnetic field sensors to the obvious antenna for telecommunication and the capacitive sensing used to detect our fingers on the touch screens.[5]

One of the sensing techniques which turned out to be hugely beneficial is nuclear magnetic resonance (NMR) spectroscopy. It was introduced in the 1930s-1950s,[6–8] a period also known as the first quantum revolution. Today this technology and it's derivatives are a key part of

our lives. Magnetic resonance imaging (MRI) is used routinely in hospitals around the world and NMR spectroscopy is one of the key analytical tools in chemistry and the life-sciences. Obviously the development of this technique is far from over, there are 111 facilities in Germany alone doing research on NMR.[9] Problems conventional NMR is still facing mainly originate from a low sensitivity, requiring macroscopic samples. Several approaches have reduced the required volumes down to nl volumes,[10–13] though major goals like single-cell NMR or even single molecules are still far out of reach.

Maybe these last hurdles left need radical, new approaches. Quantum technologies have again emerged into the limelight over the last decades. The coherent control of quantum states has become more and more sophisticated and the clever use of quantum properties allows for hitherto unknown sensitivities and precision in many fields.[14] The nitrogen vacancy (NV) center has been a most promising candidate as a quantum-platform to perform NMR experiments with. Its atomic scale and isolated electronic spin provide optimal conditions for nano- and micro-scale NMR. Major goals have been achieved over the last decade, on the nano-scale these include the detection of sub-monolayers,[15] single molecules[16] and even of individual nuclear spins.[17,18]

Micro-scale NMR has shown spectral-resolution sufficient for the resolution of chemical-shifts[19] allowing for the chemical analysis of much smaller sample sizes as previously possible. Increasing the sensitivity further, micro-scale NV-NMR opens up the possibility of single-cell NMR experiments, a long standing goal in (NV-)NMR. In addition the high spatial resolution of NV-experiments allows for the study of diffusion on the micro-scale. This plays a major role in life sciences, e.g. the nutrient transport in our cells,[20,21] in particular in the brain, where dendrites are highly anisotropic on the micro-scale.[22] Additionally, the field of microfluidics has several unsolved problems, when it comes to the measurement of dispersion, including the apparently accelerated diffusion within microdroplets[23] or the construction of microfluidic mixers.[24] The first proof of principle NV-diffusion experiments were conducted by us, which mark a major step in understanding the fundamental mechanics of particle-transport at the micro-scale. The goal of this thesis is to give a thorough introduction to NV-NMR and these

experiments. In this thesis, I will start with introducing the basic principles of quantum sensing. Starting with basic properties of quantum mechanics and the minimal requirements posed at a quantum sensor and introducing the basics of coherent control and measurements. In chapter 3, I will introduce the NV-center, explain the general concepts described in chapter 2 applied to its specific case and give an overview over its different sensing applications. In chapter 4, I will in detail explain magnetic field sensing and in particular NMR using NV-centers. Furthermore, I will introduce different sensing schemes, which are currently used or which have been proposed and are promising to be used in the future. After introducing the theory, I will talk about previous experiments using NV-NMR in chapter 5. This includes the differences in sensing especially the particular challenges faced on the different length-scales over which the NV-center is used. In chapter 6, I will discuss the particularities of micro-scale NMR using NV-centers and how to simulate the expected signals using Monte-Carlo methods. In this chapter, I will also demonstrate a novel method for the enhancement of the NV-NMR signal amplitude using gradients. When all the theory has been explained, I will introduce our measurement-setup and how it is controlled in chapter 7. Finally, I will discuss the pulsed field gradient experiments conducted in our setup and their results in chapter 8, before I conclude this thesis and give an outlook over the future of NV-NMR on the micro-scale in chapter 9.

2. Quantum sensing

The field of quantum technologies has gained much traction over the last two decades. Quantum computing is predicted to be revolutionary in many fields in the future[25] and some quantum sensors can already be bought of the shelf.[26,27] Though related the two technologies have some major differences. While researchers in quantum computing try to isolate their systems as good as possible from their surroundings, in quantum sensing the strong coupling of a quantum state to its environment is harnessed for improved sensitivity.

In this chapter the basic concepts of quantum technologies with an emphasis on quantum-sensing will be introduced and discussed. The first section introduces basic and general requirements, imposed on any quantum-sensor. The second section introduces the basic concepts of quantum-mechanics, needed to understand quantum-sensing. In the final section the basic interaction between a quantum-sensor and its environment are discussed.

2.1. Basic concepts of quantum sensing

The technological feasibility of experimental quantum mechanics have improved incredibly over the last half century. Sixty years ago the possibility of reducing information carrying hardware, or bits, to the size of a single atom seemed hardly feasible, even though the theoretical possibility and its advantages were already noticed.[28] In 2000 first quantum computing experiments had been conducted,[29,30] interestingly using NMR, and David DiVincenzo proposed criteria, which any quantum-bit, or qubit, has to fulfil to be of use.[31] Nearly all of these criteria apply equally to any qubit used for quantum sensing:

1. A scalable physical system with well-characterized qubits
2. The ability to initialize the state of the qubits
3. Long decoherence times, with respect to logic operations
4. A "universal" set of logic gates, or coherent control also between qubits
5. The ability to read out the quantum state

Here, well-characterized means a qubit with well defined eigenstates, as described in the next section 2.2. In the excellent review by C.L. Degen, F. Reinhard and P. Cappellaro,[14] a quantum sensing analogy to these criteria is listed:

1. The necessity of a well-characterized qubit.
2. The ability to initialize the state of the qubits and the capability of reading out its state.
3. The ability to coherently control the qubit, although the authors note this is not necessary for all quantum sensing schemes.
4. The ability to interact with relevant physical parameters, which are to be measured, and this interaction leading to a shift or change in the qubit's quantum state.

Note, that the first three are quite similar to the quantum-computing case: we always want full control of our system and the ability to extract information. Of what use is a sensor (or computer) without the ability to extract information?

The difference lies in two points: 1) The scalability of quantum sensors can be of advantage, but it's not necessary. If it is the goal to measure single spins, a sensor of the same scale is required and not one much bigger. 2) In a computer (no matter if quantum or not) it is necessary to control the (qu)bits and shield them as much as possible from any external influence, which might change the result of the computation. In the case of (quantum) sensing, the interaction between the (quantum) sensor and its environment is a requirement, or else nothing can be sensed.

2.2. The qubit

The fundamental unit used for quantum sensing is called qubit. As teased in the previous section, it consists of two energy levels, E_0 with eigenstate $|0\rangle$ and E_1 with eigenstate $|1\rangle$, separated by an energy $\Delta E = \hbar\omega$. (Since in reality, the quantum systems in which qubits are implemented generally have more than two eigenstates, the first DiVincenzo criterium means in particular, that the qubits energy-level separation should be different from state to state, to avoid accidental multiple excitation in the experiment.) Due to the quantum nature of the qubit, it can be in any superposition state $|\Psi\rangle$ of its eigenstates:

$$|\Psi\rangle = \alpha\,|0\rangle + \beta\,|1\rangle\ , \tag{2.1}$$

where $\alpha = ae^{-i\omega_0 t+\phi_0}$ and $\beta = be^{-i\omega_1 t+\phi_1}$ are complex numbers, with ω_0 and ω_1 being the energy-dependent frequencies of the respective eigenstates $|0\rangle$ and $|1\rangle$ and ϕ_0 and ϕ_1 their initial phases at time t=0. The probability of finding the qubit in one of its eigenstates is given by $|\alpha|^2$ and $|\beta|^2$, respectively, which means $|\alpha|^2 + |\beta|^2 = 1$.
Notice that when evolving over time,

$$\begin{aligned} |\Psi(t)\rangle &= ae^{-i(\omega_0 t+\phi_0)}\,|0\rangle + be^{-i(\omega_1 t+\phi_1)}\,|1\rangle \\ &= a\,|0\rangle + be^{-i(\omega t+\phi)}\,|1\rangle\ , \end{aligned} \tag{2.2}$$

where we have set $\omega_0 = 0$, $\phi_1 = \phi$ and $\phi_0 = 0$ without loss of generality. This leads to a time-dependent phase difference between the two states $\Delta\phi = \omega t + \phi$, also called phase accumulation. $\Delta\phi$ depends on the energy splitting of the two quantum states, since $\omega = \Delta E/\hbar$.

A convenient way of thinking about a single qubit is the so-called Bloch sphere, seen in Fig. 2.1. The probability of finding the qubit in either of its two eigenstates is displayed along the z-axis, with the $|0\rangle$-state state being on the north pole and the $|1\rangle$-state at the south pole, given by the polar angle θ. The azimuthal angle ϕ displays the relative phase between the two eigenstates.

At this point, the qubit's Hamiltonian can be described as:

$$\hat{H}_0 = \frac{\hbar\omega}{2}\,\hat{\sigma}_z\,, \tag{2.3}$$

where $\hat{\sigma}_z$ is the Pauli z-matrix. This would lead to time independent phase accumulation on the Bloch sphere, so usually the reference frame is changed to one rotating at ω. In this frame, the time evolution of a general superposition state is constant:

$$|\Psi(t)\rangle = |\Psi(0)\rangle = a\,|0\rangle + be^{i\phi}\,|1\rangle = \cos(\theta/2)\,|0\rangle + \sin(\theta/2)\,e^{i\phi}\,|1\rangle\ . \tag{2.4}$$

A more detailed description of the rotating frame and the rotating wave approximation can be found in appendix section A.

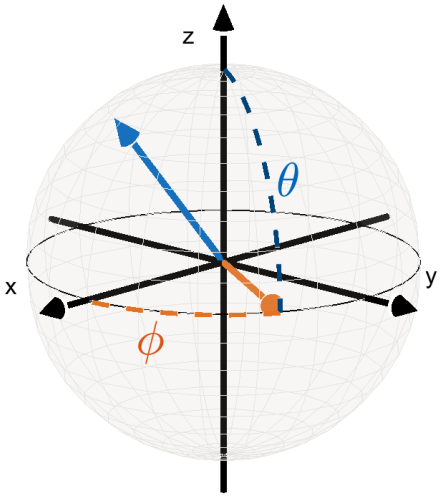

Figure 2.1.: **The Bloch sphere**
A typical image of the Bloch sphere, two quantum states are depicted, one in blue, and one in orange. The orange state's azimuthal angle ϕ is noted in red, its polar angle θ is depicted in dark blue. The orange state is parallel to the XY-plane and therefore in an equal superposition of $|0\rangle$ and $|1\rangle$, while the blue state is more likely to be measured $|0\rangle$.

2.3. Readout of a quantum two-level-system

The DiVincenzo criteria require each qubit to be initializable into one of its quantum states. In theory, the ability to read out the qubit and to coherently control its quantum state is sufficient. Considering an arbitrary quantum state $|\Psi\rangle = \alpha\,|0\rangle + \beta\,|1\rangle$, reading out the state will either collapse the wave function into $|0\rangle$ or $|1\rangle$. Now the qubit's state is known. If the goal is to initialize the state into the $|0\rangle$-state, and the result was $|0\rangle$, the goal is achieved. If the result was $|1\rangle$, the qubit can be rotated into the $|0\rangle$ state. Thus the qubit can effectively be initialized.

This method can be used for single qubits, or systems where each qubit is individually addressable, like a quantum computer. In some cases, e.g. the NV-ensembles used in the experiments described later on, all qubits are averaged and individual qubit's states remain unknown even after the measurement or they can't even be addressed individually. This means a different way of initialization is needed, e.g. laser-cooling of the qubit, as described in section 3.2.2.

It is also worth noting, that there are two different kinds of quantum readout:

- **Quantum non-demolition readout:** This means, the quantum state in which the qubit's wave function collapsed is preserved after the readout. For example, if a state $|\Psi(t)\rangle = a\,|0\rangle + be^{i\phi}\,|1\rangle$ is read out, resulting in $|0\rangle$ ($|1\rangle$), and it is read out again immediately along the same basis, it will again result in $|0\rangle$ ($|1\rangle$). An example for this would be measuring twice, along the same axis, in the Stern-Gerlach-experiment[32] or the repetitive readout described in section 4.3.3.

- **Quantum demolition readout:** Here the opposite is true, the process of reading out will collapse the state into one of the eigenstates, but the readout will always end with the qubit in the same eigenstate. As an example, imagine a qubit, where the quantum states are the existence of an electron in a capacitor $|1\rangle$ or its absence $|0\rangle$. One way of reading out this qubit would be shorting the capacitor and measuring the current. This way the qubit's state is measured to be $|1\rangle$ ($|0\rangle$) if there was (no) current. But after the readout,

the qubit will always have no electron and therefore be in state $|0\rangle$. Another example for quantum demolition readout is the optical readout of the NV^--centre described in section 3.2.1.

2.4. Qubits interacting with their environment

As mentioned in section 2.1, the qubit will always interact with its environment, which, if controlled properly can lead to formidable sensors. This interaction is in general described by:[14]

$$\hat{H}(t) = \hat{H}_0 + \hat{H}_v(t) + \hat{H}_{\text{control}}(t) \,, \tag{2.5}$$

where $\hat{H}_0$ is the qubit's internal Hamiltonian, seen in equation 2.3, which is assumed to be known. In the NV-case, it will be discussed in chapter 3. $\hat{H}_v(t)$ is the signal Hamiltonian, representing the coupling between the qubit and the signal $V(t)$ and $\hat{H}_{\text{control}}(t)$ is the control-Hamiltonian, which is also known, because it is chosen in order to manipulate the qubit. The Hamiltonian of interest obviously is $\hat{H}_v(t)$, splitting it into the part commuting with $\hat{H}_0$: $\hat{H}_{v_{||}}$ or $\hat{H}_{v_z}$ and a non-commuting part: $\hat{H}_{v_\perp}$:[14]

$$\begin{aligned} \hat{H}_{v_{||}} &= \gamma/2\, V_{||}(t)\, [|1\rangle\langle 1| - |0\rangle\langle 0|] \\ \hat{H}_{v_\perp} &= \gamma/2 \left[V_\perp(t)\, |1\rangle\langle 0| + V_\perp^\dagger(t)\, |0\rangle\langle 1| \right] \,, \end{aligned} \tag{2.6}$$

where γ is the coupling constant of the qubit and the external signal V(t). This is a first order approximation which more often than not is sufficient, but higher order effects can play a significant role, in which case this model would need to be adapted. $\hat{H}_{v_{||}}$ is the part of the signal Hamiltonian along the measurement basis and $\hat{H}_{v_\perp}$ is the orthogonal part, which can in theory drive the qubit's spin (see the next section), though in reality it will rarely be strong enough to do so.

2.4.1. Effects of a coherent drive or Rabi-oscillations

The control Hamiltonian $\hat{H}_{\text{control}}(t)$ can be chosen at will, but the question remains, what a sensible choice is. In general, a qubit will need a control field with amplitude Ω and frequency ω_d close to its transition frequency ω. We start with the Hamiltonian in equation 2.3:

$$\begin{aligned}\hat{H}(t) &= \hat{H}_0 + \hat{H}_{\text{control}}(t) \\ &= \frac{\hbar\omega}{2}\hat{\sigma}_z + \hbar\Omega\cos(\omega_d t + \phi_d)\hat{\sigma}_x \\ &\overset{rot.}{=} \frac{\hbar\Omega}{2}\left[\cos(\phi_d)\hat{\sigma}_x + \sin(\phi_d)\hat{\sigma}_y\right] ,\end{aligned} \tag{2.7}$$

where we have changed into a rotating frame after the third equal sign (see appendix section A), and have set the controlling drive frequency to be resonant $\omega_d = \omega$. The driving field's phase ϕ_d can be chosen arbitrarily. We can look at the time evolution of the last line of equation 2.7:

$$\hat{U}(t, t_0 = 0) = \exp\left(-i\frac{\Omega t}{2}\left[\cos(\phi_d)\hat{\sigma}_x + \sin(\phi_d)\hat{\sigma}_y\right]\right) , \tag{2.8}$$

then write out the Pauli-matrices and set $\phi_d = \pi$ for simplicity:

$$\hat{U}(t) = \begin{pmatrix} \cos(\frac{\Omega t}{2}) & i\,\sin(\frac{\Omega t}{2}) \\ i\,\sin(\frac{\Omega t}{2}) & \cos(\frac{\Omega t}{2}) \end{pmatrix} . \tag{2.9}$$

So a general quantum state will evolve as as:

$$|\Psi(t)\rangle = \hat{U}(t)\begin{pmatrix} a \\ b \end{pmatrix} = \begin{pmatrix} a\,\cos(\frac{\Omega t}{2}) + i\,b\,\sin(\frac{\Omega t}{2}) \\ i\,a\,\sin(\frac{\Omega t}{2}) + b\,\cos(\frac{\Omega t}{2}) \end{pmatrix} . \tag{2.10}$$

Here we see, that this coherent drive will lead to a constant, sinusoidal rotation about the x-axis (since the relative phase of the states $\phi = 0$, compare with with Fig. 2.1) at frequency

Ω. This leads to an expected readout of the $|0\rangle$ state as follows:

$$\begin{aligned} P_0(t) &= |\langle 0|\Psi(t)\rangle|^2 \\ &= |a|^2 \cos^2\left(\frac{\Omega t}{2}\right) + |b|^2 \sin^2\left(\frac{\Omega t}{2}\right) \\ &= 1/2 + \frac{|a|^2 - |b|^2}{2} \cos(\Omega t) \ . \end{aligned} \tag{2.11}$$

So the readout probability will oscillate with frequency Ω too, though the amplitude of this rotation depends on the initial state. For a, $b = 0$, i.e. starting in $|0\rangle$ or $|1\rangle$, the maximum amplitude is reached. This rotation is known under the name Rabi-oscillation[6] and is one of the key building blocks of any quantum experiment. An example of a Rabi-experiment can be seen in Fig. 2.2

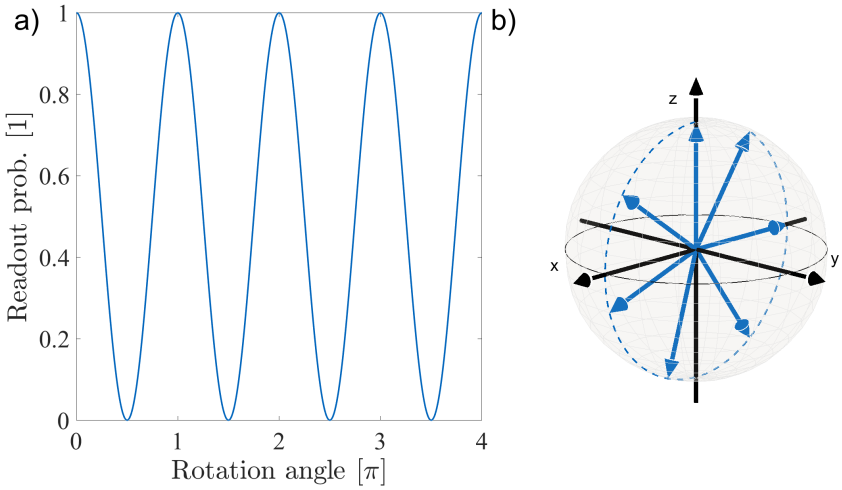

Figure 2.2.: **Rabi oscillations**
a): The probability of finding the qubit in the $|0\rangle$ state as a function of time. **b)**: The time evolution of the $|0\rangle$ state under a resonant drive. The state first evolves into an equal superposition of both eigenstates, at the XY-plane, after which it will reach the $|1\rangle$ state after a rotation of $\Omega t = \pi$.

Two special cases should be noted, first off the case where $\Omega t = \pi$, leading to an inversion of the previous quantum state. The second noteworthy angle of rotation is $\Omega t = \pi/2$, after which an initialized state $|\Psi\rangle = |0\rangle$ is rotated into an equal superposition state $|\Psi\rangle = (|0\rangle + e^{i\phi}|1\rangle)/\sqrt{2}$. These two coherent pulses build the foundation of all quantum sensing

experiments. At this point it should also be noted, that a more intuitive but less rigorous explanation of the Rabi-experiment in the case of NV-centers is given in section 3.2.2.
In the case of a non-resonant field an analytical solution can be found if starting in one of the eigenstates,[33] leading to a oscillation in the population described by:

$$P_0(t) = 1 - \frac{\Omega^2}{\Omega_g^2} \sin\left(\frac{\Omega_g t}{2}\right) , \tag{2.12}$$

where the general Rabi-frequency is defined as:

$$\Omega_g = \sqrt{\Omega^2 + (\Delta\omega)^2} , \tag{2.13}$$

with $\Delta\omega$ being the drive's detuning from the qubit's resonance frequency. So this kind of driving leads to an increase in the Rabi-frequency, while the contrast between the two poles of the Bloch-sphere is reduced.

2.4.2. Free evolution and the Ramsey-experiment

Rotations about the z-axis are a little more tricky to implement, but there exists an easy and quite elegant solution. According to the definition in equation 2.4, the y-axis is defined to be along the direction of $\theta = \pi/2$ and $\phi = \pi$. By changing our reference frame, so that the y-axis is now along $\theta = \pi/2$ and $\phi = \pi + \delta\phi$, a state that was previously along the y-axis is now rotated around the z-axis by $-\delta\phi$! This is illustrated in Fig. 2.3 a). The second way of achieving this effect is the addition of a small, time-independent field. This will slightly shift the qubit's resonant frequency by $\delta\omega \ll \omega$, leading to a constant phase accumulation of $\phi(t) = \delta\omega\, t$. This experiment is called the Ramsey-experiment and the interaction of quasi-static fields with our qubit is the second fundamental building block of quantum sensing.

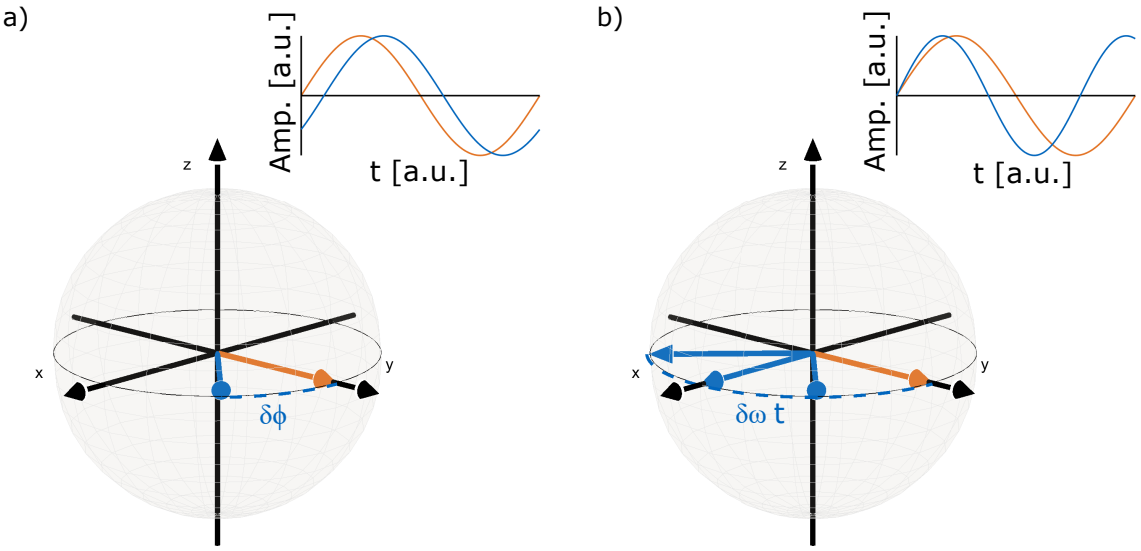

Figure 2.3.: **Rotations about the z-axis**
Two spins on the Bloch sphere, the orange spin's freqeuncy is exactly the same as the rotating frame's frequency.**a)**: Changing the reference frame's phase will lead to an effective phase accumulation in the Bloch-picture, as shown with the blue arrow. **b)**: Since we moved into a rotating frame, a small field inducing a slight frequency shift at the qubit will lead to a constant phase accumulation, as seen with the blue arrow.

2.4.3. Decoherence and relaxation

Any system in which qubits are realized is not completely isolated from its environment. External fields will interact with the qubit and influence its state in unpredictable ways, as described in this section.

Relaxation

Relaxation is the process of spontaneous decay of the qubit state, which is defined as moving from its excited state into its ground state, hence "Relaxation". It is described by the relaxation time T_1. Causes for this process are mostly of thermal nature, especially in the reverse case, i.e. "spontaneous excitation" from the ground into the excited state. Other sources of note are other qubits at similar frequencies. This can also be interpreted as the "qubit being measured

by its environment". The probability of finding the qubit in its initialized state therefore is: $\mathrm{P}(t) = \mathrm{P}(0)\, e^{-t/\mathrm{T}_1}$.

Dephasing

The dephasing time T_2^* is related to how long a superposition state stays coherent. As described in section 2.4.2, external magnetic fields have an influence on the relative phase accumulation in a superposition state. So magnetic field fluctuations, e.g. from electrons near the qubit, will lead to random phase accumulation, which will not destroy our quantum state, but change it unpredictably into one over which we have no information.

T_2^* is of high importance in most quantum technology, since both the working state of a quantum-computer and the sensing-state of a quantum-sensor generally is a superposition state. The longer T_2^*, the more operations one can run on a computer and the longer and more precise one can sense. Mostly this time-limit is set by T_2^*, since generally speaking $T_1 \gg T_2^*$. For example the the relaxation time in micro-scale NV-ensembles is on the order of ms where the dephasing time is on the order of μs. This is not always the case though and T_1 can be smaller than T_2^*.[34]

A third parameter which is of great importance is called T_2. It is related to T_2^* and described in chapter 4.

2.4.4. The quantum sensing protocol

Coming back to the excellent review by C.L. Degen, F. Reinhard and P. Cappellaro,[14] I would like to introduce their general quantum sensing-protocol, describing the steps of each quantum measurement:

1. The qubit is initalized into one of its eigenstates, generally its ground state $|0\rangle$.
2. The qubit is transformed into a desired state $|\Psi_0\rangle = \hat{U}\,|0\rangle$, in which it is most sensitive to the probed field. This is done using a set of coherent control pulses.
3. The qubit evolves under its Hamiltonian (equation 2.3), $|\Psi(t)\rangle = \hat{U}_H(0,t)\,|\Psi_0\rangle$.

4. The qubit state is transformed from a superposition in its measurement basis into the identical superposition of its readout basis. This is only necessary, if the readout basis is different from the basis, in which the qubit was evolving.

5. The final quantum state is read out.

Typically many averages are required so these steps are repeated many times, as illustrated in Fig. 2.4.

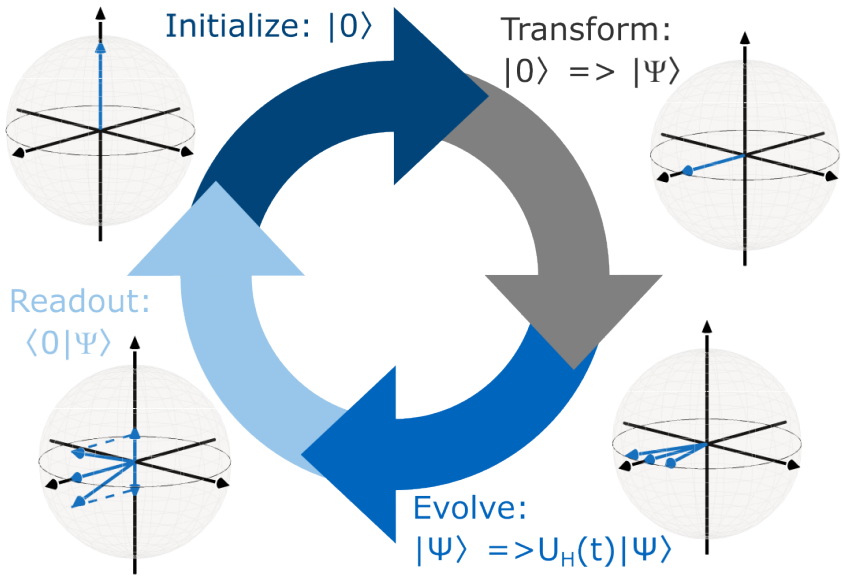

Figure 2.4.: **The quantum sensing protocol**
The main steps of each quantum sensing experiment, which are repeated and averaged many times.

3. The nitrogen vacancy center

It is the goal of this chapter, to introduce the nitrogen vacancy (NV) center in diamond and discuss, why it is a good quantum sensor and how to use it as one. In the last section of this chapter different methods of sensing using the NV-center are briefly introduced.

3.1. Diamond and defects in diamond

Throughout history diamonds have been among the most valuable gemstones. Due to the long-standing high interest in diamond, research has focused on it astonishingly early, the first known report of diamond polishing is from 1568[35] and the first synthetically grown diamond was produced in 1880.[36] Due to it being the hardest natural material, it is well suited for many industrial applications like cutting and drilling. This hardness stems from the tight packing of the face centred cubic (fcc) Bravais-lattice with basis (0, 0, 0) and (1/4, 1/4, 1/4)[37] and the strong covalent bonds between the diamonds carbon atoms. A sketch of the carbon unit-cell with defects can be seen in Fig. 3.1. The tetrahedral nature of the diamond lattice leads to each carbon atom having four neighbours with a distance of 0.154 nm, a bond angle of $\sim 109.5^\circ$ and a lattice constant of $a = 0.357$ nm. Even though it is extremely hard, diamond is not the most stable allotope of carbon, but it is still extremely stable, due to the high activation energy necessary for its graphitization.[38] The thermal conductivity is the highest known and can reach 2000 W/cm at 80 K.[39]

Diamond as a host material for defects is quite promising in various quantum technologies. This is due to its high band-gap of ~ 5.5 eV,[37,40] in which energy levels of the various defects can exist in a nearly complete isolation. Single photon emitters have been realized in diamond,

which are a key building block for quantum-communication.[41] In addition, it is a promising candidate for quantum computing, both as a processor and especially as quantum memory.[42] Lastly, defects in diamond are one of the most utilised and well understood platforms for quantum sensing.[14,43–48]

While diamond is found in nature, most diamonds used in the laboratory are synthetically made. The two main methods applied are called chemical vapour deposition (CVD) and high pressure high temperature (HPHT) treatment. They are described in more detail in appendix section F, for now it is sufficient to note, that CVD-diamonds generally are of higher purity and can be grown isotopically enriched, while HPHT-diamonds are cheaper and easier to manufacture in bulk, even though the control of number and kind of defects in the diamond is lacking.[43,49] Furthermore diamonds are categorised in "Type I" and "Type II" diamonds. Type I diamonds are ones, which have aggregated (Type Ia) or isolated (Type Ib) nitrogen impurities, HPHT diamonds are most often of this type. Type II diamonds are either pure (Type IIa), meaning they do not contain any defects, or they contain boron defects (Type IIb).[43,50] Diamonds used for quantum technologies typically are type IIa diamonds.

Defects in diamond come in all shapes and colors. This is meant quite literally, since not only do various numbers and species of atoms contribute to the different kinds of vacancies, but also do the vacancies color the diamond. This is why they are also often dubbed "color centres". In the following I will quickly introduce the two main types of color centres used in quantum technologies.

Group IV defects

Group IV defects form by two neighbouring carbon atoms being replaced by vacancies and a group IV element lying in between,[51] as seen in Fig. 3.1 b). The most prominent candidate for quantum technologies is the negatively charged silicon-vacancy (SiV) center,[52] though also the negatively charged germanium-vacancy,[53] tin-vacancy[54] as well as lead-vacancy

centres[55] have been investigated thoroughly. They are of particular interest, due to their high Debeye-Waller-factor, which describes a crystal (defect's) ability to coherently emit photons[52] as well as their high inversion symmetry, D_{3d}. This enables them to be used as high quality single photon sources, which is of strong interest in quantum-communications.[41,51]

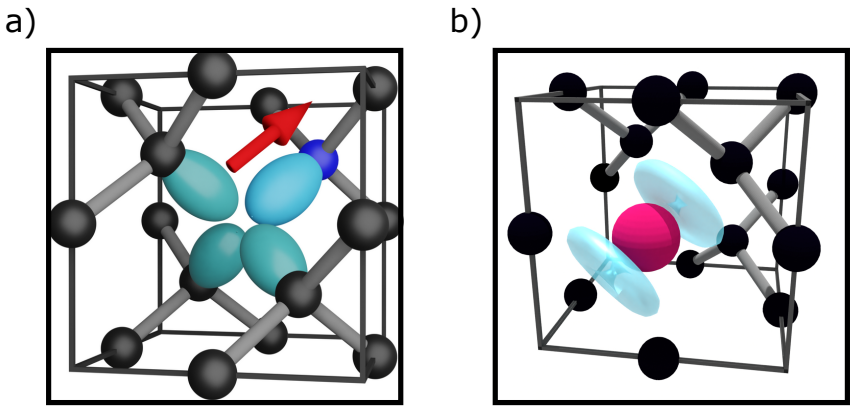

Figure 3.1.: **Defects in diamond**
a): The nitrogen vacancy center, one carbon atom (black) is replaced by a nitrogen atom (blue) and an adjacent lattice site is vacant (cyan lobes). The NV-center orientation is indicated with the red arrow. **b)**: An example of a group IV defect, the group IV element (red) sits in between two vacancies (cyan torus), creating a highly symmetric defect.

Nitrogen-vacancy centres

The nitrogen vacancy center itself consists of a nitrogen atom substituting a carbon atom and an adjacent vacancy, leading to a C_{3v} symmetry, as seen in Fig. 3.1 a). The symmetry axis connects the vacancy and the nitrogen, leading to four different possible orientations of NV-centres in the diamond lattice. It is the focus of this thesis and will be described in much detail in section 3.2. They have been discovered as early as the 1970,[56] even though their high potential for quantum applications has only been discovered about thirty years later.[57] The main reasons it is a prime candidate in all fields of quantum science are its extremely long coherence and relaxation times at room temperature.

3.2. Quantum sensing using NV-centres

In this chapter I will give a quick overview of the basic principles most quantum sensing techniques using NV-centres have in common, as well as a general overview of how an NV-experiment is conducted. Since the main focus of this thesis is on magnetometry, especially NMR, an in depth description of it can be found in the next chapter, chapter 4.

3.2.1. The NV-bandstructure

The extraordinary characteristics of diamond have been already described in section 3.1. The most important one for quantum sensing using NV-centres, is the high band-gap of ~ 5.5 eV[37,40] at the Γ-point in the first Brillouin-zone.

The NV-center appears in three different charge states, the positively charged state is exceedingly rare in diamond and doesn't play a role in NV-sensing,[43,45] therefore it will not be discussed in this thesis. The neutral NV^0-centre's electronic structure is created by the three unbound carbon electrons and the two free electrons of the nitrogen. It lacks the optical readout properties as well as spin properties of the NV^- charge state, which will be discussed later in this section and is therefore of little interest to us. It is one of the most common defects in natural diamonds, and will always be present in synthetic NV-diamonds, even though it is undesirable. This is not alone due to the fact, that there are various optical and non optical conversion methods between NV^0 and NV^-.[43,45,58] The effects of a high NV^0 concentration in diamond are discussed in more detail in appendix section G.

The main defect in diamond used for quantum sensing is the negatively charged NV^--center. Since we will mainly discuss the NV^--center from now on, I will drop the superscript and refer to it as NV-center for the rest of this work. its electronic structure is defined by the five electrons mentioned for the NV^0-center plus an additional electron from some donor in the diamond. The energy-levels of the NV center located in the diamond-band-gap can be seen in Fig. 3.2.

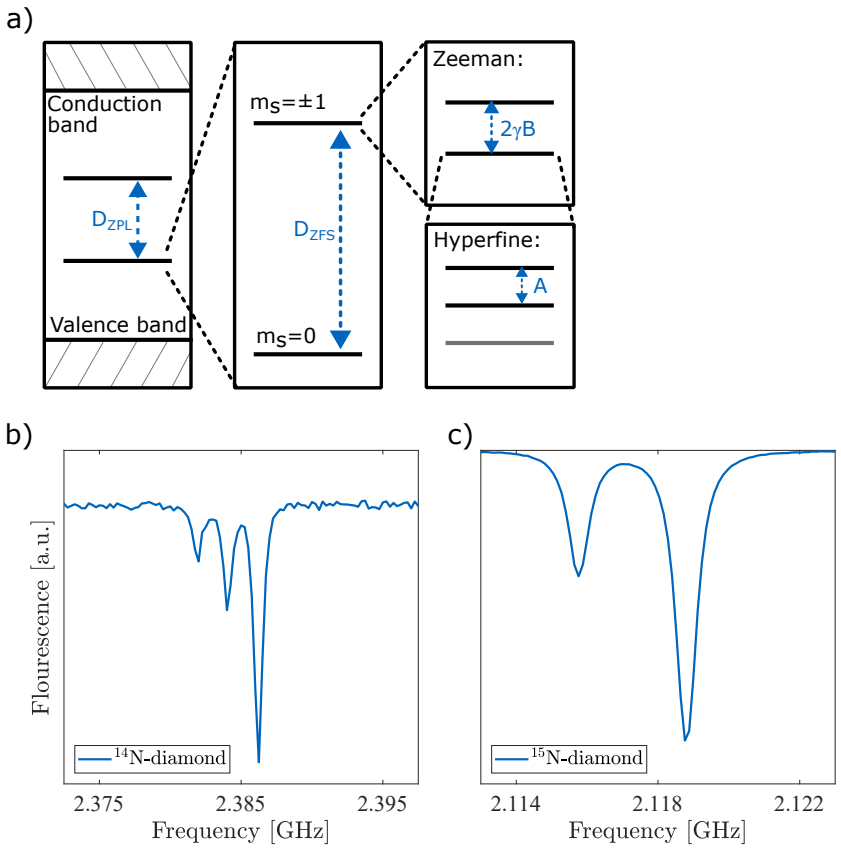

Figure 3.2.: **The energy levels of the NV-centre**
a): *Box one:* The electronic states of the NV^--center in diamond. Excited and ground-state are well isolated in the diamond's energy gap. *Box two:* The splitting of the electronic states due to the triplet spin-states of the NV^--centre's electronic spin. *Box three:* A depiction of the Zeeman-splitting of the +1 state. At zero magnetic field the $\pm$ 1 states are degenerate, but with an applied magnetic field the energy levels split. *Box four:* Even further splitting occurs due to coupling between the NV^--centre's electrons and the nitrogen nucleus. Depending on the nitrogen isotope, the splitting occurs into three our two states, separated by the isotope specific hyperfine constant A $\approx$ 3 MHz. In addition, there is the quadrupolar splitting, not depicted here. **b)**: An example of an electron spin resonance experiment (ESR) with a ^{14}N and ^{15}N diamond, respectively. The NV-driving frequency is swept and the fluorescence is recorded. There is a dip in fluorescence, if the drive is on resonance with the qubit, here the hyperfine-splitting is well resolved. The ESR experiment is described in more detail in section 3.2.2.

The Hamiltonian describing the NV-center consists of four major terms:[43,59]

$$\hat{H}_{NV} = \hat{H}_{ZFS} + \hat{H}_{ZM} + \hat{H}_{HF} + \hat{H}_{QP} \,, \tag{3.1}$$

where $\hat{H}_{ZFS}$ is the Hamiltonian describing the zero field splitting (ZFS) of $D_z \approx 2.87\,\text{GHz}$, $\hat{H}_{ZM}$ is the Zeeman-Hamiltonian, $\hat{H}_{HF}$ describes the hyperfine interaction between the electrons and the nitrogen-nucleus and $\hat{H}_{QP}$ accounts for the quadrupole interaction. The ZFS Hamiltonian is:

$$\hat{H}_{ZFS} = hD_z S_z^2 + hE(S_x^2 - S_y^2) \,, \tag{3.2}$$

where S_z is the z-component of the dimensionless electronic spin-1 operator $\vec{S} = (S_x, S_y, S_z)$ and $E = \frac{D_x - D_Y}{2}$ is dependent on the x and y-component of the zero field tensor. Since $D_x - D_Y = 0$ unless the C_{3v} symmetry is broken, this term is zero in the absence of perturbations like strains or external electric fields. The Zeeman-Hamiltonian is described by:

$$\hat{H}_{ZM} = h\frac{g_e \mu_B}{\hbar}(\vec{B} \cdot \vec{S}) = h\gamma_{electron}/2\pi(\vec{B} \cdot \vec{S}) \,, \tag{3.3}$$

where $\vec{B}$ is the external magnetic field, $g_e \approx 2.003$ is the NV-electronic g-factor, $\hbar$ is the reduced Planck-constant, μ_B is the Bohr-magneton and $\gamma_{electron} = 176.09\,\frac{\text{rad}\,\text{GHz}}{\text{T}}$ is the electron's gyromagnetic ratio.[60]

From here on I will differentiate between the gyromagnetic ratio without angular units and the one including the angular unit of 2π. I will denote this difference using the "reduced gyromagnetic ratio": $\gamma = \frac{\gamma}{2\pi}$! This means e.g. $\gamma_{electron} \approx 176.09/2\pi\,\frac{\text{GHz}}{\text{T}} \approx 28.025\,\frac{\text{GHz}}{\text{T}}$ and $\hat{H}_{ZM} = \gamma_{electron}(\vec{B} \cdot \vec{S})$.

At certain magnetic fields the Zeeman-term leads to level-crossings and interesting effects, these are discussed in appendix section H.

The hyperfine-Hamiltonian describes the interactions between the electronic spin state and

the nitrogen-nucleus close by:

$$\hat{H}_{HF} = hA_{||}S_zI_z + hA_{\perp}(S_xI_x + S_yI_y) \ , \tag{3.4}$$

where $A_{||} \approx -2.3(3.0)$MHz and $A_{\perp} \approx -2.7(3.7)$ MHz are the parallel and orthogonal hyperfine coupling coefficients for the nitrogen isotope ^{14}N (^{15}N) respectively.[59,61] Finally, $\vec{I} = (I_x, I_y, I_z)$ is the nuclear spin operator.

Since ^{14}N has a spin larger than 1/2, it has a quadrupolar moment. In this case $\hat{H}_{QP}$ is non-zero because the nuclear electric quadrupolar parameter P is non-zero:[45]

$$\hat{H}_{QP} = hP\left(I_z^2 - \frac{I(I+1)}{3}\right) \ . \tag{3.5}$$

The Hamiltonian in equation 3.1 describes the triplet states, which are predominantly used for NV-sensing. In addition to them there the singlet states are located in the band gap.[62] These play an important role for initialization and NV-readout, as discussed below. For more details, the interested reader is referred to the excellent review by M. Doherty[45] and the investigation of the NV-center by A. Gali.[58]

3.2.2. Control of the NV-center

As listed in section 2.1, C. Degen et al. have modified the DiVincenzo criteria for quantum computing to apply to quantum sensing. In the following, I will explain how the NV-center in diamond fulfils every point on the list.

A well-characterized qubit

The energy structure of the NV-center has been discussed in detail. The two energy states used to define a qubit for the NV-center are the triplet-ground state ($|0\rangle$) and one of the triplet excited states ($|1\rangle$). When a external magnetic field of a couple mT is applied, the Zeeman-splitting of the ± 1 states is sufficient to separate their energy levels far enough with

respect to the driving pulses (see below) and the NV-center resonance's linewidth. Even though the chosen states are split further due to the hyperfine and quadrupole interactions, these splittings are on the order of ∼3 MHz or less. Typical driving pulses are of strength $\Omega > 3$ MHz, so this further splitting is of no effect and the states are driven as if they were one.

Initialization and readout

Initialisation of the NV-centre's quantum state is possible via optical spin Dpolarization.[45,63] The spin transitions of interest can be seen in Fig. 3.3 a). Both the $|0\rangle$ as well as the $|\pm1\rangle$ states can be optically excited to their respective excited states, via green (typically 532 nm) laser illumination.

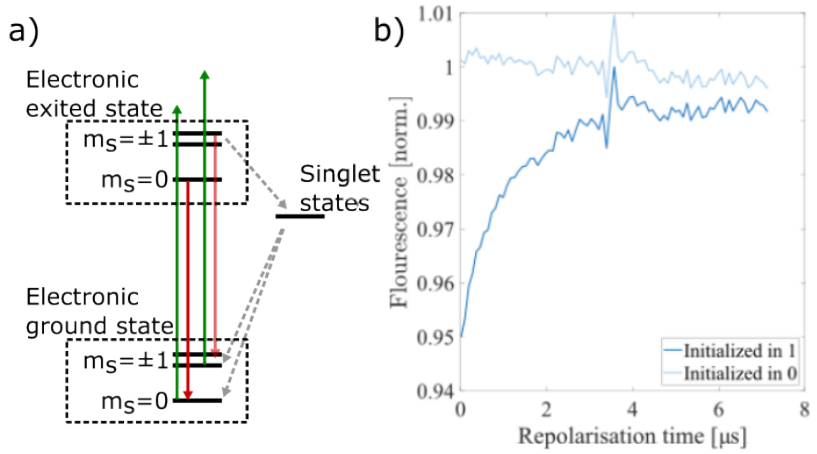

Figure 3.3.: **NV-centre repolarization**
a): The NV-centre's energy-level diagram, displaying the optical-polarization process. Green arrows indicate laser-excitation, while red arrows indicate red fluorescence-decay. The grey arrows display the ISCs, which are only radiating in the infra-red. **b)**: Normalized experimental data, displaying the state-dependent difference in fluorescence. The dark blue curve is from a quantum state initialized in the $|1\rangle$-state and the light blue curve from the $|0\rangle$-state.

The lifetimes of the excited states are comparatively short ($\ll$ 30 ns[62,64]), and all states decay back into their respective ground states in a red-fluorescence process. In addition to these spin-conserving decay processes, both excited states can decay via the singlet states,

further decaying into the triplet-ground states. This inter-system-crossing (ISC) is possible due to phonon mediated spin-orbit interactions between the triplet-excited states and the singlet states.[58] The ISC *from* the $|0\rangle$-excited state to the singlet states is much more unlikely than the one *from* the $|\pm1\rangle$-excited states. But the ISC *to* the $|0\rangle$-ground state is much more likely than the one *to* the $|\pm1\rangle$-ground states.[45,58,62] This effectively pumps the nitrogen vacancy center into the m_s=0 state, granting us the desired ability to initialize our qubit. Depending on the laser intensity, this optical-polarization process needs several iterations to fully polarize the NV-center, as seen in Fig. 3.3 b). Not only will optical-spin-polarization initialize the NV-center, the ISC also gives us the possibility of spin dependent optical readout. One of the singlet states involved in the ISC has a temperature dependent lifetime of 178-300 ns.[62,64,65] Since the lifetimes of the triplet-excited states are $\ll$ 30 ns,[62,64] during the $\sim$ 5-10 μs it takes to initialize the qubit, a qubit starting in the $|1\rangle$-state will decay through the singlet states, spending time on the order of $\sim$ 200 ns shelving in one of the dark states, while a qubit in the $|0\rangle$-state undergoes several iterations of excitation and fluorescence-decay. This ultimately leads to a spin dependent fluorescence intensity, which can be optically-detected. In addition to the optical readout, an electrical readout technique exists.[66,67] In contrast to the optical-detection, it uses a two-step photon absorption process, which has the ability to excite the NV-electron into the diamond's conduction-band,[58] which in turn leads to a detectable current through the diamond crystal. Since the $|1\rangle$-state undergoes less optical-excitation cycles, due to the shelving in the singlet states, it has a lower probability of being excited into the conduction-band, leading to a spin-state dependent current.

Applying low power ($\Omega t \ll \pi$) microwave pulses and sweeping their frequency will result in a dip in the NV-centre's fluorescence at the resonant frequency of the qubit, since the spin state is partially transferred from the brighter $|0\rangle$ into the darker $|1\rangle$ state. This experiment is called electron spin resonance (ESR) and can be seen in Fig. 3.2 b).

NV-center alignment

The NV-centre's ZFS at ~ 2.87 GHz indicates a magnetic field at the defect site in the order of ~ 0.1 T, which is in the direction of the defect's orientation in the diamond crystal.[45] External magnetic fields applied to the defect will add vectorial with this ZFS-splitting, and can change the symmetry of the defect's magnetic structure, if not also aligned along the NV-centre's direction.

Coherent qubit control

Coherent control of the NV-center is of major importance for the sensing schemes described in chapter 4. When applying an oscillating magnetic field, orthogonal to $\hat{B}_0$, at the resonant frequency ω, the qubit population oscillates between $|0\rangle$ and $|1\rangle$. Intuitively this can be understood when thinking about the non-rotating lab-frame: In this frame the qubit sees the magnet field of strength B_1 oscillating at the same frequency as itself, therefore the azimuthal-angle ϕ between the NV-centre's spin direction and the $\hat{B}_1$ field is constant, as seen in fig 3.4. Seeing this "constant"-field, the NV starts precessing around it with frequency $\Omega = \gamma B_1$, or its Rabi-frequency. Since the direction of this rotation is only dependent on the relative azimuthal angle ϕ of the axis of rotation (or the relative phase of the driving field) and the polar-angle of rotation due to the field is $\theta_{\text{Rabi}} = \Omega t$, we have full control over the NV-center. The argument presented here is obviously extremely hand-wavey, for the more rigorous derivation see section 2.4.

Certain challenges occur when trying to drive the NV-center at extremely low fields ($B_0 \leq \Omega/\gamma$) and extremely high fields ($B_0 \geq 1$ T). When driving at low fields, the qubit state is no longer well defined, since the driving-field's bandwidth is much bigger than the $|\pm 1\rangle$-states Zeeman-splitting. There are solutions to this problem,[68] relying on driving at $\omega = 2.87$ GHz, leading to an equal detuning of $\pm\Delta$ between the resonance-frequency and the driving-frequency for both $m_s = \pm 1$ states. The problems occurring at high frequencies are hardware-related, since the NV-centre's spin is of electronic nature, it has an extremely

high gyromagnetic ratio of $\gamma_e \approx 28.025$ GHz/T. With increasing magnetic field, the necessary driving-frequency increases as well, leading to power delivery-problems. Solutions to these exist in the form of expensive hardware, though some additional engineering is required.

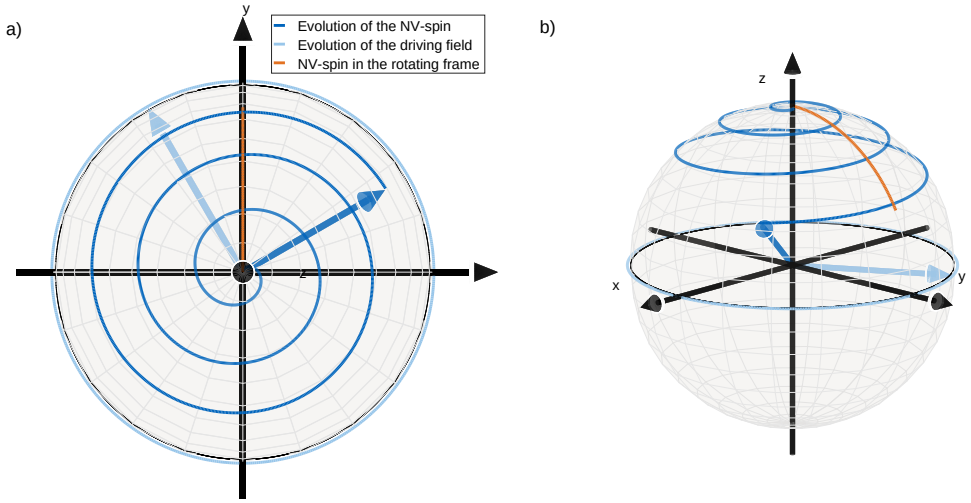

Figure 3.4.: **Effects of a resonant drive on a qubit**
a): The Bloch-sphere in the laboratory-frame, as seen from the top. The angle between the driving-field (light blue) and the NV-centre's spin (blue) stays constant. **b)**: The Bloch-Sphere seen from the side. The effect of the driving field leads to a downwards-spiralling motion of the NV-center, which looks like a rotation around the x axis in the rotating frame (orange line). The driving field has no components along $\hat{B}_0$.

General NV-experiment

Generally most NV-experiment consists of the same blocks, seen in Fig. 3.5 a). First the NV-center is repolarized, using a laser pulse, this is typically combined with the readout laser pulse of any given experiment, and is omitted in Fig. 3.5. Afterwards, the experiment is conducted, for example the ESR-experiment, also shown in Fig. 3.2 and 3.5 b), where a single micro-wave pulse is applied, whose frequency changes in each step of the experiment. Next, the NV-centre's quantum-state is read out and the state is again prepared in $|0\rangle$. Readout and repolarization can be done using the same laser pulse, since both rely on the same optical-pumping technique. Afterwards the experiment is repeated, but without microwave

pulse, resulting in the fluorescence of the previously initialized $|0\rangle$-state. The first result is then divided by the second to cancel out slowly fluctuating noise sources, mostly fluctuations in the laser intensity. The effect of this is clearly visible in the data set shown in Fig. 3.5 b).

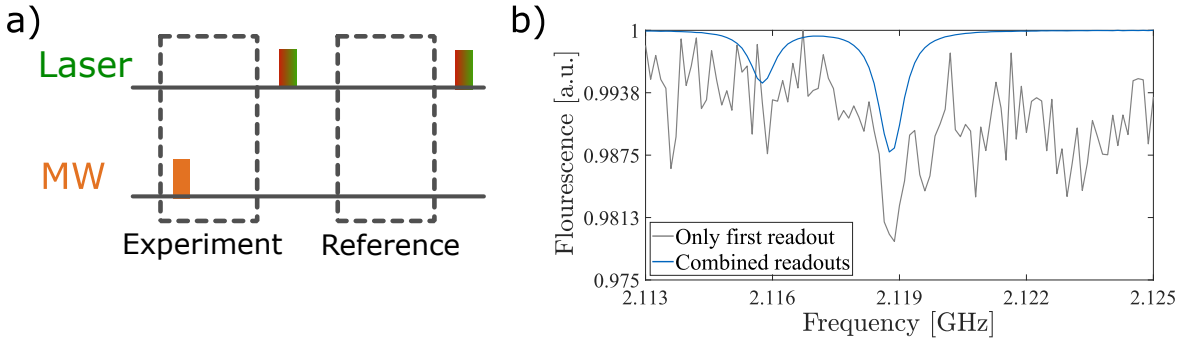

Figure 3.5.: **The general NV experiment**
a): A typical NV- experiment consisting of two blocks with similar experiments, which are then combined to remove "slow" noise. **b)**: Data from a ^{15}N ESR experiment. In gray the data collected from the first readout, in blue the data after noise-cancellation using the second readout.

A similar approach is applied for many other experiments, where the final spin-state is mapped once into $|\Psi_1\rangle = a\,|0\rangle + be^{i\phi}\,|1\rangle + \delta_{slow}$ and once into $|\Psi_2\rangle = b\,|0\rangle + ae^{i\phi}\,|1\rangle + \delta_{slow}$, where δ_{slow} denotes the laser noise. The resulting measurements will have an average fluorescence intensity $I_1 = (a-b) * C + \delta_{slow}$ and $I_1 = -(a-b) * C + \delta_{slow}$, where C is the measurement contrast between the two eigenstates. Afterwards both data sets are subtracted, removing the noise, but still containing the same amount of information as two individual measurements: $I_{mean} = 2\,(a-b)$.

3.2.3. Different use-cases for NV-sensing

As mentioned in chapter 2, we need our qubit to interact with an external quantity, effecting its quantum state, to be able to extract information from it. In most experiments using NV-centers this interaction boils down to a difference in the qubit's Zeeman-term or its ZFS-splitting. The reason, this is extremely powerful, has to to with a combination of the high electronic gyromagnetic ratio, leading to a strong response to small changes, and the fact that

the NV-center is nested in a crystal lattice. This is important, because the energy-structure surrounding the NV-center[45] will change with a plethora of parameters, ultimately leading to a change in the ZFS, which in turn can be sensed. The following examples are not a complete list of the NV-centre's applications.

Temperature sensing

NV-centres are formidable temperature sensors, they are operable over a wide temperature range, 100-1000 K,[69] reaching sensitivities of 76 $\mu K/\sqrt{\text{Hz}}$.[70] The most straight forward way of measuring temperature using NV-centre's in diamond is via the ZFS's temperature dependence. This has first been discovered in 2011[71] and has since been investigated in detail.[69] Especially interesting are wide field[72,73] and nano-scale approaches, allowing for much higher spatial resolution than conventional sensors,[72] e.g. even within single cells, using nano-diamonds.[73,74]

The NV-Gyroscope

Recently rotation and motion sensing using the NV-center has been demonstrated.[75] This is possible due to an additional term in the NV-Hamiltonian, which is dependent on rotation about the NV-axis.[75] Even though cheap and effective gyroscope solutions exist, this might pave the way to drift-free and calibration less gyroscopes.

Magnetometry

NV-magnetometry is the main focus of this thesis and especially AC-magnetometry will be discussed in detail in chapter 4. A comprehensive overview of NV-based magnetometry can also be found in the beginning of the review written by Barry et al.[43] NV-magnetometry generally boils down too a measurement of the change in the NV-Zeeman term. One example I already discussed in section 2.4.2, is the technique called Ramsey-sensing, used for DC-field measurements.

One of the mayor advantages of NV-sensing, is the possibility of imaging. By using a

camera to detect the NV-fluorescence intensity a 2D-image of the investigated quantity can be collected. The principles of this so called "Quantum diamond microscope" are described in this review by E. Levine at al.[76] In general, most quantities, which can be sensed using NV-centres can benefit form an imaging approach, though noteworthy examples include the imaging of currents in micro-chips[77,78] and 2D-materials.[79] A parallel approach of imaging using NV-centres, is by using a single NV-center on the tip of a cantilever. This method has started to gain traction outside of the NV-community in the investigation of 2D-structures, such as skyrmionic-[80] and helimagnetic-systems,[81] in-plane magentic fields[82] and domain-walls.[83]

Relaxometry

Relaxometry is the measurement of the T_1-relaxation rate of the NV-center. Since the relaxation-rate depends on the spins electromagnetic environment, this is a elegant and simple to implement way of detecting concentrations of electric or magnetic particles in the NV-centre's vicinity. Examples of the experiments conducted are the imaging of magnetic nano-particles,[84] the detection of free radicals[85] or recently the detection of μM ion-concentrations in water.[86]

4. Nuclear magnetic resonance using NV-centres

In this chapter I focus on magnetometry using the NV-centre. In the first section the basic concepts in NMR, which are also relevant to NV-NMR are introduced. In the second section it is discussed, how to measure oscillating magnetic fields, and how to do so frequency selective. And in the final section more advanced sensing-schemes are introduced.

4.1. NMR basics

NMR has been a staple spectroscopy technique in many fields, mainly related to medicine, biology and chemistry. It is non-invasive and gives quantitative results. While I will not discuss the working principles of a conventional NMR-spectrometer, I will quickly discuss the basics of what NMR-senses and how the conventional NMR-spectrometer differs from the NV-centre. It should be mentioned, that for the sake of simplicity I will always assume the NMR-sample consists of pure water, unless explicitly mentioned otherwise.

4.1.1. Dipolar fields and magnetization

Nuclei that can be sensed using NMR are limited to nuclear isotopes with a spin $\geq \frac{1}{2}$. For example ^{12}C can not be sensed using NMR, while ^{13}C is NMR-active. This can be explained by the dipolar nature of a spin half system, or the main transition of a half-integer spin system in general.

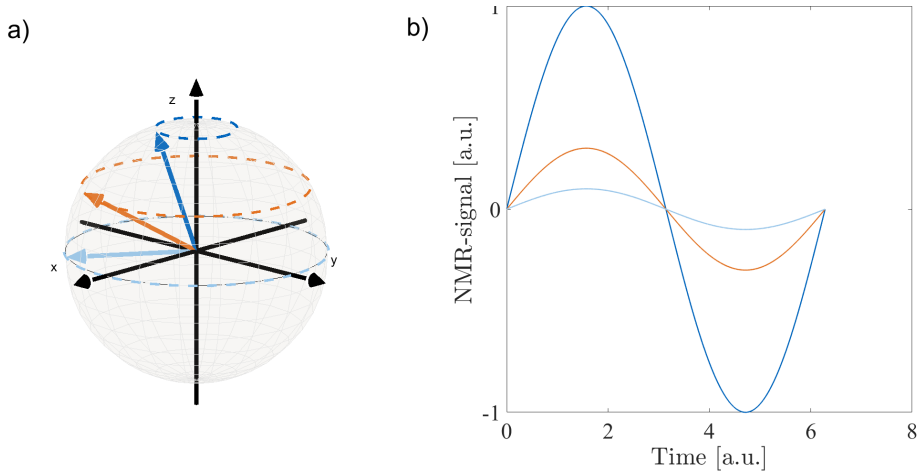

Figure 4.1.: **NMR-signal amplitude depending on $\hat{m}_\perp$**
a): Different spins in the laboratory-frame Bloch-sphere. A spin in the initial state $|\Psi\rangle = |0\rangle$ is parallel to $\hat{B}_0$ and will not precess. The larger the spins component perpendicular to $\hat{B}_0$, $\hat{m}_\perp$, the stronger the amplitude of the spins precession. Leading to a stronger change in magnetic field at the sensor, as seen in **b)**.

When measuring NMR, the sample will generally be an ensemble of sample spins and not all of them will be in the same state. There will always be a difference in the state-population, this can be due to thermodynamic reasons or, in the case of small ensembles, purely statistical. Both cases are described in 4.1.2. This difference is called the polarization of the sample and leads to a net magnetization. In conventional NMR, this magnetization precesses around the external magnetic field after an applied $\pi/2$-pulse, in turn inducing a current in a coil wound around the sample. The sample's dephasing time will lead to an exponential decay of the oscillation amplitude, leading to a phenomenon called free induction decay (FID).
In NV-NMR, we have no detection coils, but the NV-centre's Zeeman-term. Each sample spin can be modelled as a small magnetic-dipole[87,88] with magnetic field at point $\vec{r}$:

$$\vec{B}_{spin} = \frac{\mu_0}{4\pi} \frac{3\hat{r}(\vec{m} \cdot \hat{r})}{r^3} , \tag{4.1}$$

where $\vec{m}$ is the direction and amplitude of the magnetic dipole, μ_0 is the magnetic permeability and $\hat{r}$ and r are the direction and magnitude of $\vec{r}$ respectively. The sum of the $\hat{B}_{||}$-components of these magnetic fields will lead to a shift in the NV-centre's Zeeman-splitting, which can be

detected. The $\hat{B}_\perp$-components of the sample spins are too small to lead to any measurable effect. Here two things should be noted **1)** the field of a magnetic dipole in equation 4.1 strongly depends on the relative direction between the dipole and the place it is measured, in this case the NV-centre. This will be discussed in detail in chapter 6. **2)** As long as the dipole orientation is not parallel to $\hat{B}_0$, the dipoles will be precessing and therefore the magnetic field at the NV-centre will be a oscillating (AC) and decaying field also called free nuclear decay (FND), see Fig. 4.1. How these are measured will be discussed in section 4.2.

4.1.2. Statistical, thermal and hyper-polarization

The major problem with NMR is the lack of molar sensitivity. Normal NMR-experiments require millilitre sample-volumes or milligram sample mass. There have been efforts to miniaturize the pickup coils, reducing the sample volume down to ~ 0.1 nanolitre volumes,[10–13] though the picolitre and even smaller scales, which are possible with NV-NMR are far out of reach. NV-NMR uses single spins or ensembles, which lie several nano or micro-meter below the surface of the diamond. The volume in which the majority of the NMR-signal originates from, is of the same order as this NV-diamond distance, leading to much smaller sample volumes.[15,88–91] These volumes are discussed in detail for micro-scale NMR in chapter 6 and for nano-scale NMR in appendix section E. Still, micro-scale NV-NMR suffers from similar problems. The sample polarization is of a thermal nature, meaning it arises from all micro-states being equally likely (see Fig. 4.2), ultimately leading to a polarization which is dependent on the Boltzmann distribution:[92–94]

$$P(B_0,T) = \frac{N_\uparrow - N_\downarrow}{N_\uparrow + N_\downarrow} = \frac{\exp(h\gamma B_0/k_B T) - \exp(-h\,\gamma B_0/k_B T)}{\exp(h\gamma B_0/k_B T) + \exp(-h\gamma B_0/k_B T)} \approx \frac{h\gamma B_0}{2k_B T}\,, \tag{4.2}$$

where k_B is the Boltzmann-constant, T is the temperature and $N_\uparrow$ and $N_\downarrow$ are the populations of the $|\uparrow\rangle$ and $|\downarrow\rangle$ states, respectively. We have used a Taylor series to the the first order in $\frac{h\gamma B_0}{k_B T}$, since $h\gamma B_0 \ll k_B T$. For typical values in our NV-setup of T = 25° C and B_0 = 0.175 T, this leads to a polarization of ~ 0.6 ppm.

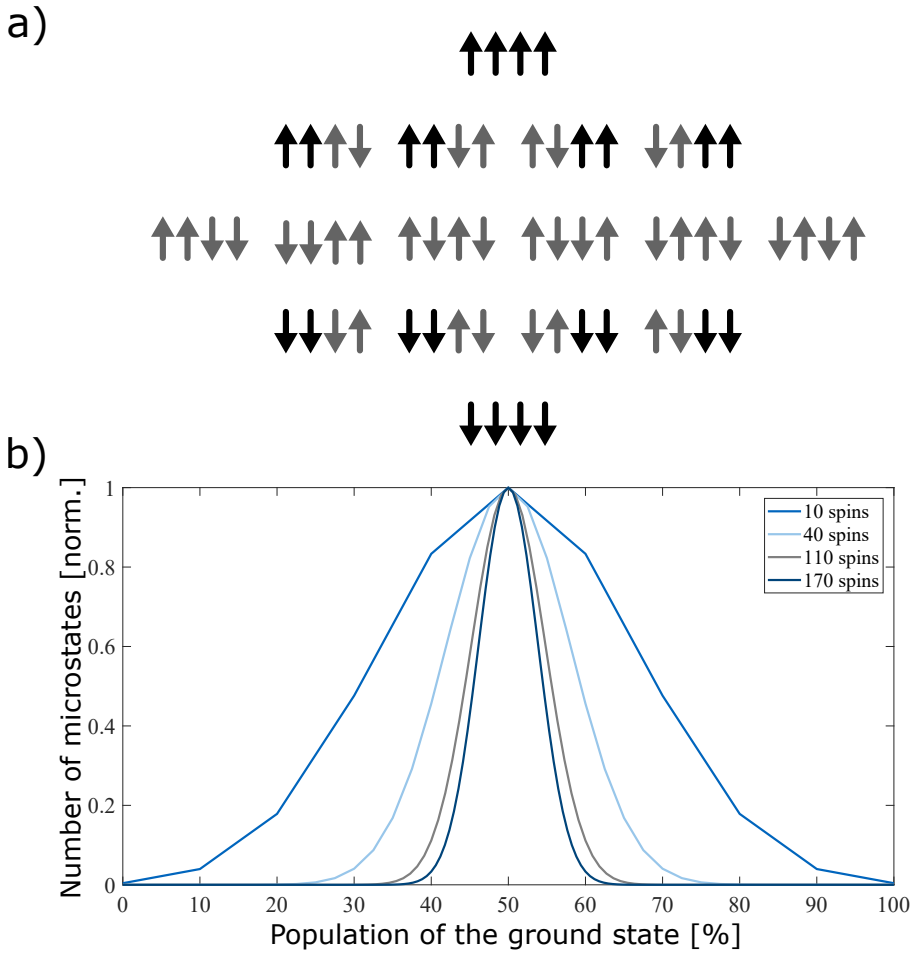

Figure 4.2.: **Sample polarization depending on the number of spins**
a): For a four-spin system there are 16 micro-states with equal probability. Black spins indicate the polarized spins, grey spins cancel each other out. Only two states are fully polarized while eight states are polarized 50 % and six states are not polarized at all. **b)**: With increasing number of spins, a totally unpolarized micro-state becomes more and more likely, while any kind of polarization becomes increasingly unlikely.

One of the advantages of nano-scale NV-NMR, is a much higher polarization. As seen in Fig. 4.3, the percentage of micro-states with a high polarization is much higher for small number of spins, so that the small sample volumes measured can reach a polarization up to the order of $\sim 3\%$.[93,95] For a spin-1/2 system, it is described by:[48,93]

$$P_{stat}(N) = \sqrt{1/N}\,. \tag{4.3}$$

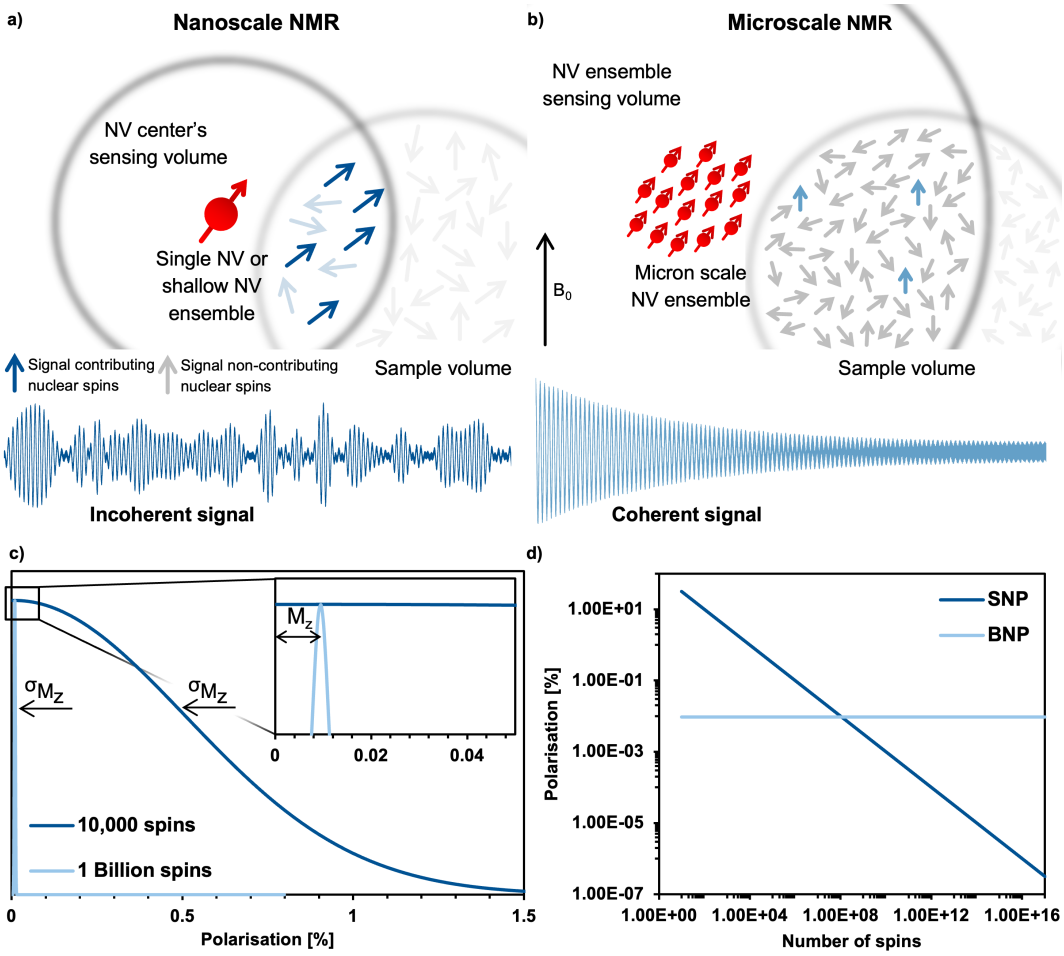

Figure 4.3.: **Statistical and Boltzmann polarization**
a): A schematic depiction of statistical nuclear polarization and its high polarization. **b)**: A schematic depiction of thermal or Boltzmann nuclear polarization, only few spins are polarized. **c)** The extreme cases of the binomial distribution, also depicted in Fig. 4.2 b). Here the number of possible micro-states, or their respective polarization is shown for 10k and 1 billion proton-spins at 28 T and 300° K. **d)**: The sample polarization as a function of number of spins, for a water sample at 28 T and 300° K. For a small number of spins statistical polarization dominates. This figure was taken from Allert et al.[48] with permission of the author under the Creative Commons Attribution-Noncommercial-ShareAlike licence.

The comparison between statistical and thermal polarization can be found in Fig. 4.3 c). A consequence of the statistical nature of the polarization in nano-scale experiments is the fluctuation of the sample-field amplitude,[48,95] since the amplitude as well as the direction

(phase) of the polarization will vary from average to average.

Since the lack of polarization has been a problem for NMR-experiments since the beginning, much thought has been put into artificially increasing the sample-magnetization, also called hyperpolarization. One method used in all micro-scale NMR experiments in this thesis is Overhauser dynamic nuclear hyperpolarization,[96] which is described in appendix section D. There are many more or less efficient and difficult to implement hyperpolarization methods, which also have been used together with NV-NMR experiments, like Overhauser hyperpolarization[19] or Parahydrogen Induced Polarization, Signal Amplification by Reversible Exchange.[97] Also the NV-centre itself has been discussed as a possible method for hyperpolarization,[91,98–100] since the electronic-spins of the NV-centre itself are able to be polarized up to 80%.[48] Though so far this high polarization has not been transferred to a sample efficiently.

4.1.3. Chemical resolution

Chemical information is extracted via magnetic field-independent J-coupling terms, dipolar interactions between nuclei within the same molecule, and the chemical shift, which is magnetic field dependent and arises from electrons shielding the nuclei.[92,94] J-coupling terms typically are on the order of several Hz, whereas chemical-shifts scale linearly with the magnetic fields used in our NV-experiments. Better resolved chemical shifts, as well as the increased polarization for micro-scale experiments, see equation 4.2, are the two main motivations to increase the magnetic field of NV-NMR experiments.

Typically the spectral linewidth is limited by either T_1 or T_2^* decay of the sample protons, in the case of nano-scale NV-NMR it can actually also be limited by the diffusion in and out of the sample volume.[15,89,90,95] Since each NV-centre couples to its own subset of sample-spins and therefore detects a different direction and magnitude of statistical sample polarization, a substantial exchange of spins during the time of a measurement will lead to a loss of information.

4.2. Dynamic decoupling

The idea of dynamical decoupling (DD) goes back to the 1950s.[8] The main idea is, to reapply π-pulses to a qubit in a superposition state to cancel out decoherence, as explained in this section. I will first introduce these basic ideas, then mention the most common DD-sequences used in NV-NMR.

4.2.1. The Hahn-echo experiment

The Hahn-echo or spin-echo experiment is one of the most relevant experiments in quantum technologies and builds the basis for every experiment discussed further on. A qubit is first initialized in the $|0\rangle$-state and rotated about the x-axis into an equal superposition state.

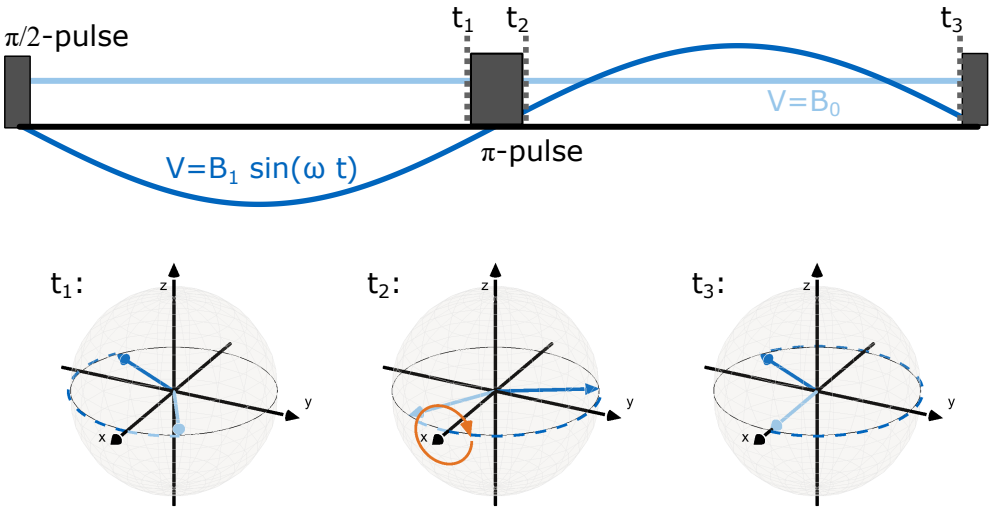

Figure 4.4.: **The Hahn-echo experiment**
In the Hahn-echo experiment is capable of cancelling constant and slow fields, but is still sensitive to AC-frequencies close to $\frac{1}{2\tau}$. Initially both spins depicted have been rotated for $\pi/2$ about the y-axis. At $t = t_1$ they have accumulated a phase due to the respective magnetic fields. At $t = t_2$ the π-pulse has inverted the accumulated phase. At $t = t_3$ the light blue spin, sensing the constant field has accumulated the same amount of phase as before, resulting in a net-0 phase accumulation. Since the oscillating field changed sign, the direction of the phase accumulation of the dark blue spin changed as well. This results in a non-zero phase accumulation.

Here it will accumulate a phase due to an external signal $V(t)$ according to:

$$\phi = \int_0^t \gamma V(t')dt' \,. \tag{4.4}$$

After a time τ, a π-pulse is applied as seen in Fig. 4.4. A constant magnetic field $V_0(t) = B_{max}$ will first lead to a phase-accumulation of ϕ_c and after the π-pulse the time evolution is reversed and a second waiting period τ will lead to a cancellation of the phase accumulation and result in a so called echo in the coherence.

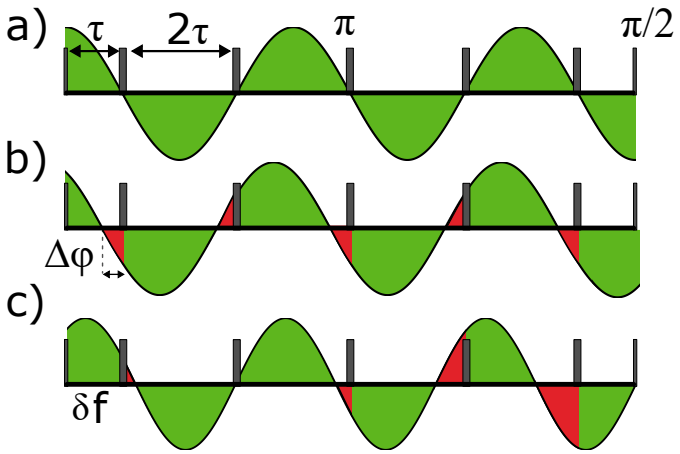

Figure 4.5.: **Phase accumulation during a CPMG experiment**
π-pulses are indicated as black vertical boxes, $\pi/2$-pulses as boxes half the width. The external NMR-signal is indicated as a sinusoidal oscillation. Green areas under the NMR-signal indicate phase accumulation of the NV-centre's spin in one direction and red areas indicate phase accumulation in the opposite direction. **a)**: In the CPMG-experiment multiple π-pulses lead to repeating reversals of the time-evolution. A frequency matching the resonance condition $f_{res} = \frac{1}{4\tau}$ will lead to continuous phase-accumulation. **b)**: If the initial phase is non-zero, the amplitude of this phase-accumulation decreases. **c)**: A detuned frequency will have the same effect of decreasing the accumulated phase compared to a).

Oscillations with frequencies in the order of $\omega \approx \frac{1}{2\tau}$, for example the one displayed in Fig. 4.4, can still lead to a net-phase accumulation. Finally a last $\pi/2$-pulse is applied, mapping the accumulated phase back onto the XZ or YZ-plane, where a difference in population depending on the accumulated phase can be read out.[43,44,101] The phase-accumulation of the

Hahn-echo experiment with a resonant magnetic field can be written as

$$\phi = \int_0^{\tau} \gamma B_1 \sin(2\pi t'/(2\tau))dt' - \int_{\tau}^{2\tau} \gamma B_1 \sin(2\pi t'/(2\tau))dt' = 8\gamma B_1 \tau \ . \tag{4.5}$$

T_2 decoherence

In chapter 2 the basic concept of the dephasing time T_2^* was introduced. Since the Hahn-echo and the DD-sequences described further on extend the spin coherence by removing the effects of constant and slowly oscillating fields, a second dephasing time called T_2 was introduced. This describes the decay of the Hahn-echo amplitude as a function of τ and is in general more descriptive of the qubit, due to DD being so ubiquitous in quantum technology.

4.2.2. CPMG and the filter function

The idea of the spin echo can be extended using multiple π-pulses.[102] The simplest instance of this is the Carr-Purcell-Meiboom-Gill (CPMG) sequence, depicted in Fig. 4.5. The initial phase of the AC-signal, as well as its frequency play a major role. The phase-accumulation can be described by:[14]

$$\begin{aligned} \phi &= \gamma B_{max} t \, W(f_{ac}, \alpha) \\ W(f_{ac}, \alpha) &= \mathrm{sinc}(\pi f_{ac} n\tau)\,(1 - \sec(\pi f_{ac}\tau))\,\cos\alpha + \pi f_{ac} n\tau \ , \end{aligned} \tag{4.6}$$

where n is the number of π-pulses in the pulse-train, $W(f_{ac}, \alpha)$ is a weighting or filter function, seen in Fig. 4.6 a) and α is the initial phase of the signal at the first $\pi/2$-pulse. For large n the filter function becomes very peaked and can be approximated as peaks with amplitude:[14]

$$W(\alpha) = \frac{2}{\pi k}(-1)^{\frac{k-1}{2}} \cos(\alpha) \ , \tag{4.7}$$

centered around the centre frequencies:

$$f_k = k/(4\tau) \ , \tag{4.8}$$

with a bandwidth:

$$\Delta f \approx 1/(n\tau)\ , \tag{4.9}$$

where k is an integer representing the k^{th} harmonic of $f_{res} = 1/(4\tau)$.

This frequency-filter is easily tunable, since its centre frequency only depends on the spacing of the pulses within the pulse train, and its bandwidth only depends on the number of π-pulses. The basic idea between all of the following DD and sensing-protocols, is to tune this frequency as close as possible to the expected NMR-signal, $\tau = 1/(4f_{res})$, to be as sensitive as possible.

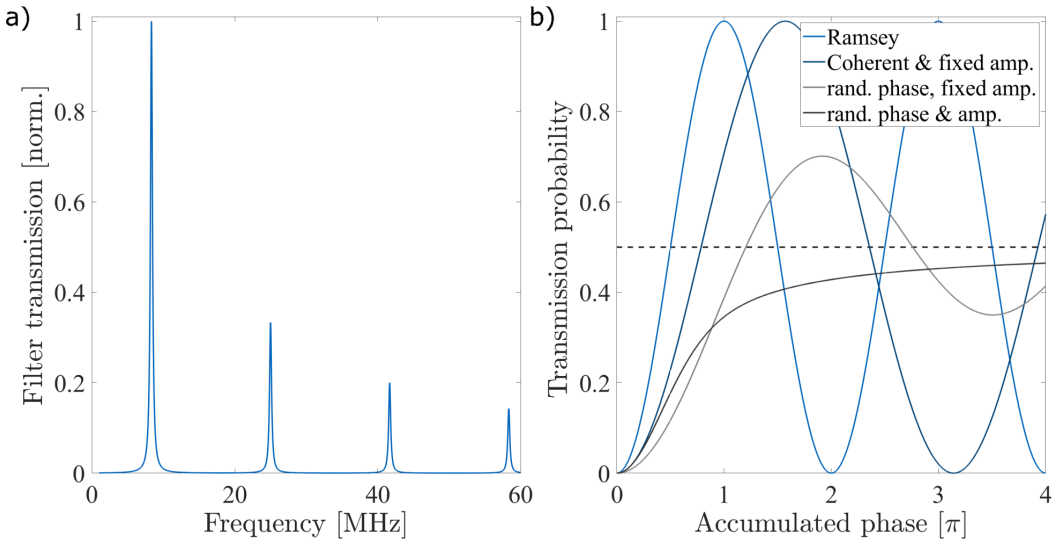

Figure 4.6.: **Frequency filter function and transmission probability of the CPMG sequence a)**: The filter function of equation 4.7 to 4.9. The pulse train is only sensitive to the target frequency and its harmonics. **b)**: The transmission probability between the initial $|0\rangle$ and the $|1\rangle$ states, for various kinds of signal when measured with a CPMG-sequence.[14] The equations for each of these curves can be found in section 4.2.3.

4.2.3. Random phases and random amplitudes: Cosine- and sine-magnetometry

The target signal is not always coherent, nor does the signals amplitude necessarily follow a well-behaved function. An example of this can be seen in the case of statistical polarization,

where both amplitude and phase of the signal underlay random fluctuations. In micro-scale NMR, a coherent signal with more or less fixed amplitude (on the time-scale of one CPMG-sequence) is measured. Therefore, the transition probability from the initial $|0\rangle$ to the $|1\rangle$-state for a resonant-frequency can be calculated directly via the known, accumulated phase[14] and is displayed in dark blue in Fig. 4.6 b):

$$p_{\text{coherent}}(t) = \frac{1}{2}\left[1 - \cos\left(\frac{4\gamma B_{max} t \cos(\alpha)}{k}\right)\right] . \tag{4.10}$$

In the case of this type of coherent signal, so called sine-magnetometry is used. The idea behind this goes back to the reason behind the second $\pi/2$-pulse ($\frac{\pi}{2}_2$). If $\frac{\pi}{2}_2$-pulse would not exist, the spin population would be in an equal superposition state (somewhere on the XY-plane) and the probability of obtaining either $|1\rangle$ or $|0\rangle$ would be equal, totally independent of the amount of phase accumulation. The $\frac{\pi}{2}_2$-pulse projects the XY-plane into a plane parallel to the z-axis, therefore transferring the difference in phase between the $|1\rangle$ and $|0\rangle$-states into a difference in transmission probability (population). Generally the NMR-signals will only lead only to a small phase-accumulation angle ϕ, so, without loss of generality assuming the first $\pi/2$-pulse ($\frac{\pi}{2}_1$) to be about the x-axis, the spin's quantum state will be close to the y-axis $|\Psi_{\text{pre}-\frac{\pi}{2}_2}\rangle = (|0\rangle + e^{\pm i\phi}|1\rangle)/\sqrt{2}$. If there is a 90° phase shift between the $\frac{\pi}{2}_1$ and $\frac{\pi}{2}_2$-pulse, i.e. the $\frac{\pi}{2}_2$-pulse is about the y-axis, the state will be:

$$|\Psi_{\sin}\rangle = \cos(\pi/4 \pm \phi)|0\rangle + \sin(\pi/4 \pm \phi)|1\rangle . \tag{4.11}$$

This means the difference between the sign of phase accumulation translates into a difference in transmission probability and we can coherently determine the NMR-signal's phase. Generally the signal response as a function of phase is sine-like, as seen in Fig. 4.7, hence the name. On the other hand, if the phase of the signal between measurements were random, the transmission probability would also randomly switch sign and averaging with this kind of measurement-scheme would reduce the signal strength continuously. Using cosine-magnetometry, where the $\frac{\pi}{2}_1$ and $\frac{\pi}{2}_2$-pulse have 0° phase shift, transforming the state

to $|\Psi\rangle = (|0\rangle + e^{\pm i\phi}|1\rangle)/\sqrt{2}$ to be:

$$|\Psi_{\cos}\rangle = \cos(\pm\phi)|0\rangle + i\sin(\pm\phi)|1\rangle = \cos(\phi)|0\rangle \pm i\sin(\phi)|1\rangle \ , \tag{4.12}$$

resulting in a signal-phase independent transmission probability from $|0\rangle$ to $|1\rangle$ of $p_{cosine}(\phi) = \sin^2(\phi)$ or in the small-angle approximation $p_{cosine}(\phi) = \phi^2$. Since the behaviour of this sign-independent measurement-scheme is quadratic, after averaging sufficiently, this is a measurement of the signal's variance $\langle\phi^2\rangle$.

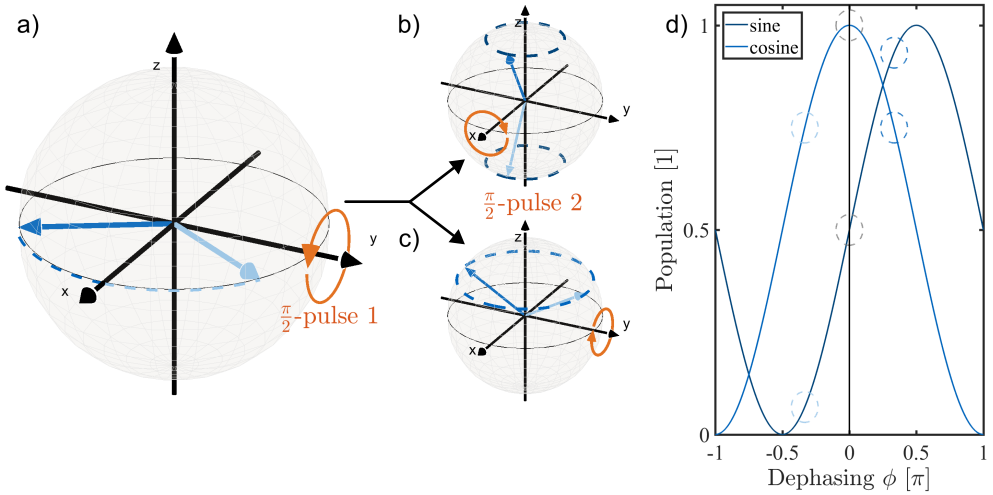

Figure 4.7.: **Sine and cosine-magnetometry**
a): Two qubits have been initialized, rotated onto the x-axis with a $\pi/2$-pulse about the x-axis. Both have accumulated the same phase but with opposite sign due to their respective evolution during a CPMG-sequence. e.g. due to the fields $B_1(t) = \cos(2\pi t/(4\tau))$ and $B_2(t) = \cos(2\pi t/(4\tau) + \pi)$. **b)**: Sine-magnetometry: In this case the last readout pulse is a $\pi/2$-pulse about the x-axis. The dark blue spin is now more likely to be read out as $|0\rangle$ and the light blue spin is more likely to be read out as $|1\rangle$, so we are able to distinguish the difference in phase of the $B_1(t)$ and $B_2(t)$. **c)**: Cosine-magnetometry: In this case the last pulse is about the y-axis. Both spins are now equally likely to be read out as $|0\rangle$. Therefore this sensing scheme is not phase-sensitive, it can not distinguish between $B_1(t)$ and $B_2(t)$. **d)**: The transition probability for cosine and sine-magnetometry. For small angles/phase-accumulations (grey dotted circles), the response for cosine-magnetometry is quadratic and for sine-magnetometry linear. The cases shown in b) and c) are circled with the respective spin-colours.

In the case of a resonant signal with constant amplitude but random phase, the transmission probability is:[103]

$$p_{\text{rand.phase}}(t) = \frac{1}{2}\left[1 - J_0\left(\frac{4\sqrt{2}\gamma B_{rms} t}{k}\right)\right] , \tag{4.13}$$

where B_{rms} is the root-mean-square of the signal-field and J_0 is the zeroth Bessel function of the first kind.

Lastly we have the case of the resonant nano-scale NMR-signal, where phase and amplitude can fluctuate on between measurements. In this case still the variance of the magnetic field is measured, but the transmission probability is:[14]

$$p_{\text{rand.phase}}(t) = \frac{1}{2}\left[1 - \exp\left(\frac{2\pi^2 \overline{W}^2 \gamma^2 B_{rms}^2 t^2}{k^2}\right) I_0\left(\frac{2\pi^2 \overline{W}^2 \gamma^2 B_{rms}^2 t^2}{k^2}\right)\right] , \tag{4.14}$$

where I_0 is the zeroth modified Bessel function of the first kind and $\overline{W}^2$ is the phase-averaged weighting function:

$$\overline{W}^2(f_{ac}) = \frac{1}{2\pi}\int_0^{2\pi} W^2(f_{ac,\alpha})d\alpha = \text{sinc}^2(\pi f_{ac} n t)/2\,(1 - \sec(\pi f_{ac}\tau))^2 . \tag{4.15}$$

All transmission probabilities as a function of accumulated phase can be seen in Fig. 4.6.

4.2.4. Advanced DD-protocols

Even though the CPMG-sequence is the basic building block of all DD-schemes described in this section, it itself is experimentally much too unstable. The following sequences all try to compensate pulse-errors, e.g. in the NV-driving fields power. This is by no means a complete list of approaches, but a selection of the author, which he deems interesting and/or important to note.

XY-N sequence

The XY-N sequence was proposed in the 1990s[104] and introduces pulses along both the y (π_y) and x-axis (π_x) within the π-pulse train. XY-N consists of N π-pulses, in total acting as an

identity-matrix on the quantum state. Therefore each of these blocks is then repeated as often as one desires, as seen in Fig. 4.8 a). The alternation of these pulses allows for much greater pulse-error compensation.[104]

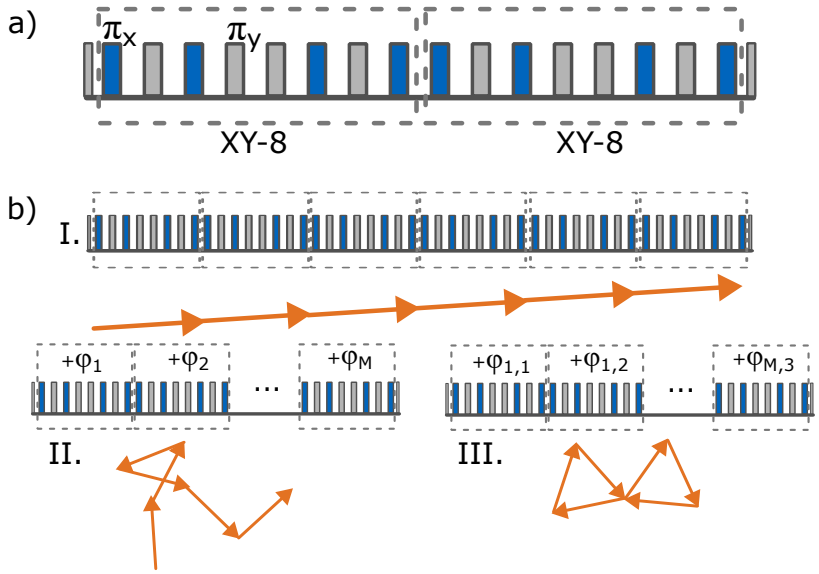

Figure 4.8.: **Improving pulse error robustness with random pulse-phases**
a) The $(XY\text{-}8)_1$ sequence, consisting of eight π-pulses with alternating phases between π_y and π_x. Each block of eight pulses acts as an identity-matrix on the NV-spin state. **b)** *I*:: Each pulse-block in the $(XY\text{-}8)_6$ sequence has the same remaining error, which in turn adds up coherently, as indicated by the orange arrows. *II*: If each block has a randomly chosen phase added to it, the errors perform a random walk and do not add coherently any more. *III*: If each subset of three blocks has randomly chosen phases, which in turn sum to zero, their pulse errors cancel out.

This problem is quite prevalent with the CPMG-sequence. If every π-pulse has an error of 1-2 %, this adds up quickly during a pulse train of only tens of pulses, rendering the resulting quantum state completely unusable.[104]

Random phases

The idea behind this approach is to cancel out the remaining pulse error of each of the XY-N blocks.[105] This protocol is a bit more complicated, so please refer to Fig. 4.8 b) for a visual

aid.

Since the relative phase of each pulse determines the axis, around which the Bloch-vector rotates, the initialization-pulse sets the frame of reference and is arbitrarily defined as a $\pi_x/2$-pulse. The first block of XY-N pulses should be in the same frame of reference and will, map the Bloch-vector back onto the y-axis, with a small error $\delta\theta$. As described for the CPMG sequence above, chaining these XY-N blocks will also accumulate pulse errors linearly. Since each block acts as an identity-matrix, the relative phases from block to block do not matter. Adding a random phase to each pulse of each block, will not change the magnitude of the rotation-error, but it will change its direction, leading to an incoherent addition of the errors akin to a random walk.

Finally one can divide the whole sequence in chains of M XY-N blocks. Then each Mth phase is chosen randomly, and the remaining M-1 phases of the chain are chosen in a way, that $\sum_{k=1}^{M} \phi_k = 0$. This results into chains of M x N π-pulses, whose errors should act as an identity matrix, even further increasing the pulse-error stability.

UDD sequence

This DD-sequence is in a way an extension of the XY-N-sequence. It is called universally robust dynamical decoupling (UDD), since in theory it can be made arbitrarily robust against pulse errors. It tries to maximize the fidelity F of the pulse sequence by introducing even more axis of rotation, according to:[106]

$$F = \frac{1}{2}|\mathrm{Tr}(\hat{U}_0^{\dagger}\hat{U}^{(n)})| \equiv 1 - \epsilon_n \,, \tag{4.16}$$

where $\hat{U}$ is the pulse sequence's propagator and ϵ_n is the fidelity error after n pulse sequence blocks. Genov et al. came up with the following phases, to cancel out errors for a UDD-N sequence with N being even:

$$\phi_k^{(n)} = \frac{(k-1)(k-2)}{2}\Phi^{(n)} + (k-1)\phi_2 \,, \tag{4.17}$$

where k denotes the k^{th} pulse in the sequence, ϕ_2 can be chosen at will and $\Phi^{(4m)} = \pm\pi/m$ or $\Phi^{(4m+2)} = \pm\frac{2m\pi}{2m+1}$ applies respectively.

Due to its great robustness and ease of implementation it was used as the basis-pulse sequence for all experiments in this thesis.

DROID

Recently the disorder-robust interaction-decoupling (DROID) framework was presented,[107] who's goal it is to give a general framework of Hamiltonian-engineering, to design a pulse-sequence best suited for the task. The whole theory is too much to discuss in this thesis, but the interested reader is referred to Choi et al.[107] for an in-depth description of this framework, and to Arunkumar et al.,[108] for experimental results.

4.3. Pulse sequences for NV-NMR

Each of the different pulse sequences discussed in section 4.2 gives us the possibility to do frequency selective ac-magnetometry. Since the bandwidth of each of the filter function is set by the number of π-pulses, it ultimately is limited by the NV-centre's dephasing time T_2. In micro-scale NV-ensembles, T_2 ranges from $\sim 1\,\mu$s to $\sim 100\,\mu$s, leading to a frequency resolution of these DD-methods of ~ 1 MHz to ~ 10 kHz, which is far from sufficient for the resolution of the chemical structure of molecules. In this section more sophisticated approaches of ac-magnetometry are discussed, which again reflect the author's choice of important and/or interesting magnetometry sequences.

4.3.1. Correlation spectroscopy

This pulse sequence has been proposed, to extend the spectral resolution from being T_2 limited to be T_1 limited. Correlation spectroscopy reduces the linewidth down to ~ 1 kHz and has found application mainly in nano-scale NMR-experiments.[15,109]

As depicted in Fig. 4.9, two full DD-sequences are repeated after one another, with a spacing

Δt between them. After the first DD-sequence, a phase ϕ_1 is accumulated and transferred into a population difference, which will then only decay with T_1. For the second DD-sequence, the initial phase α_2 of the AC-signal will depend on the spacing Δt and will vary with respect to ϕ_1 as $\alpha_2 = \alpha_1 + \Delta t \omega_{ac}$. The total transmission probability of both measurement blocks will be the product of the individual transmission probabilities of the individual results: $p_{tot}(\alpha_1, \Delta t) = p_1(\alpha_1) p_2(\alpha_1, \Delta t)$.

Sweeping the separation Δt, leads to a decaying oscillation with frequency $f_{ac}(\Delta t)$ and envelope $e^{-\Delta t / T_1}$, correlating the signal with the relative phases ϕ_1 and ϕ_2.

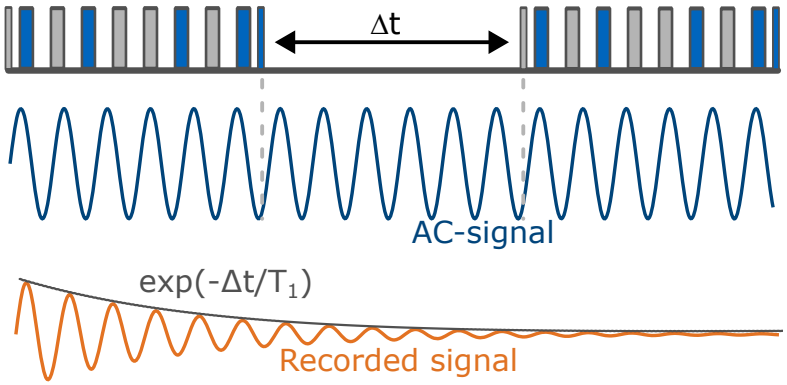

Figure 4.9.: **Correlation spectroscopy**
In correlation spectroscopy, the separation between two DD-sequences is swept. This leads to an oscillation of the second DD-block's starting phase. The resulting data is an oscillation, decaying with the NV-centre relaxation-time or the diffusion-constant of the sample.

4.3.2. Coherently averaged synchronised readout

Coherently averaged synchronised readout (CASR) is a heterodyne detection method for **coherent** signals.[87] This makes it unsuitable for the detection of statistical polarization, though a similar sequence has been used with single NV-centres for the detection of coherent, oscillating signals and even NMR.[110–112] CASR is the detection-method, which is used together with the UDD-sequence for all NMR-experiments in this publication. A detailed investigation of the ins and outs of CASR can be found in appendix section B, for this section I will only

mention the core concepts, also seen in Fig. 4.10. The core idea of CASR is the repetition of several frequency-selective DD-sequences, with a spacing of $\Delta_{CASR} = N4\tau = \frac{N}{f_{res}}$ and a target signal $f_{target} = f_{res} + \delta f$, where k is an integer and $\delta f \ll f_{res}$. The relative starting phase of f_{target} and therefore the recorded phase of each of the individual measurements, will be oscillating with δf.

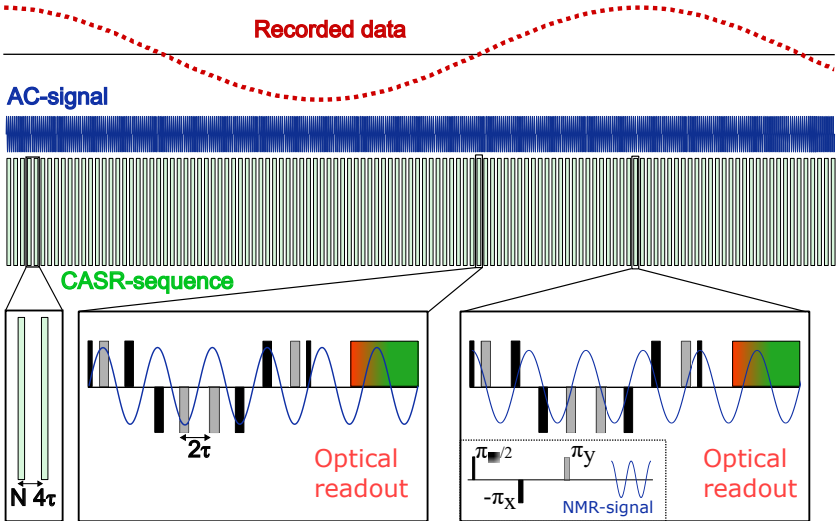

Figure 4.10.: **Coherently averaged synchronised readout**
A Sketch of the CASR sequence. The spacing of the individual DD-sequences is a multiple of a frequency close to the target AC-frequency (blue). The relative difference between the initial phase of the AC-frequency with respect to the start of each individual CASR-block (green rectangles), leads to an oscillation in the phase accumulation during each block. This in turn leads to an oscillation in the recorded fluorescence-data. The two inlets in the bottom right illustrate the two extreme cases: the first having a relative phase leading to minimal signal amplitude, the second leading to maximum signal amplitude.

The linewidth of this heterodyne approach is in principal limited by the accuracy of the DD-sequence spacing, which in turn depends on the stability of the clock used for separating these pulses. In the case of NMR-signals though, it is limited by the coherence of the target nucleus. This in turn depends on the homogeneity of the magnetic field seen by the sample, and has reached $\sim T_2^* = 0.1$ s or ~ 0.2 ppm in our experiment, which is sufficient for chemical-shift resolution.

4.3.3. Repetitive readout

Repetitive readout has been introduced some time ago[113] and shows great promise in more recent results.[108,114] The idea is to replace the averaging of multiple lengthy DD-sequences or the correlation spectroscopy sequence, with one lengthy measurement and multiple quick and repeated non-destructive readouts of the nearby nitrogen nuclear spin.

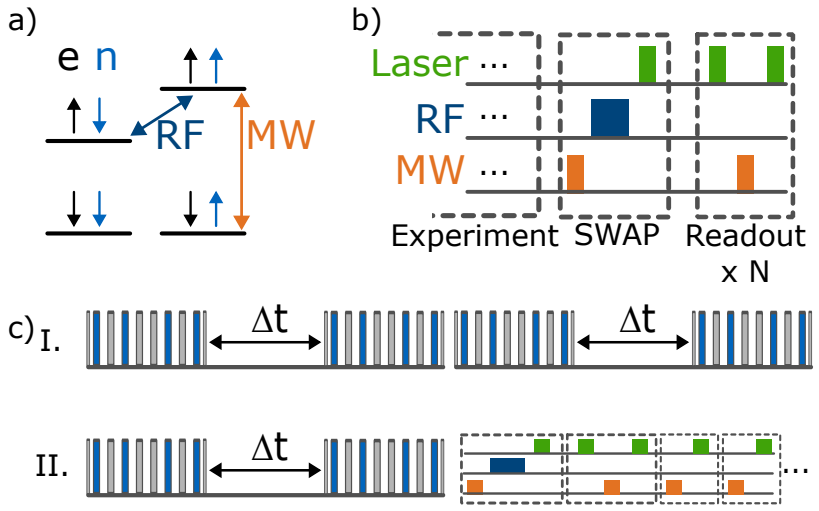

Figure 4.11.: **Repetitive readout**
a): The different hyperfine transitions can be driven selectively allowing the transfer of spin states between the ^{15}N nuclear (n) and the NV-electronic spins (e). **b)**: The sequence used for repetitive readout, all pulses are π-pulses. First the NV-centre is initialized, then a microwave pulse selectively drives the $|e_\downarrow, n_\uparrow\rangle$ and $|e_\uparrow, n_\uparrow\rangle$ transition, acting as a CNOT-gate, controlled by the nuclear spin. Afterwards the radio frequency transition between the electron excited-state hyperfine lines is driven, again acting as a CNOT-gate, but this time controlled by the electron spin. Both gates together act as a spin-SWAP. Finally the electronic spin is re-polarized and the micro-wave hyperfine transition is driven, to map the previously stored state back onto the electron. **c)**: Sketch of the measurement speed up. Correlated spectroscopy takes much longer (I.), than the repetitive readout step (II.), therefore the experiment can be sped up using the technique.

As shown in Fig. 4.11, it is possible to swap the NV-centre's spin state with the ^{15}N's spin state, by selectively driving the hyperfine transitions and the nitrogen's spin-transition.[108,113,114] This information can then be repeatedly mapped from the nucleus back onto the NV-centre's spin, readout, and mapped back again. As long as this process is shorter than the the time

of a single measurement, the experiment can be averaged more often during the same total measurement time.

4.3.4. Nano-NMR using entanglement

The first time, that chemical-shifts were resolved using NV-NMR experiments was using a correlation approach including entanglement with the nearby ^{15}N nucleus.[114] In addition, this sequence also uses repetitive readout for faster averaging. The selective NV-^{15}N transitions are the same as in Fig. 4.11.

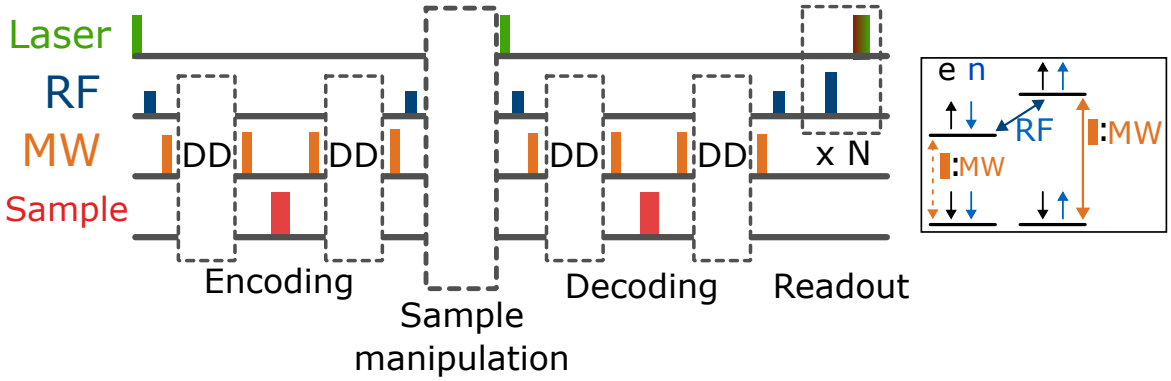

Figure 4.12.: **Entanglement enhanced spectral resolution**
The pulse sequenced used by Aslam et al.,[114] which is described in detail in this section. Blue RF-pulses of half height denote $\pi/2$-pulses. The blocks labelled DD are replaced by any CPMG-like DD sequence.

The measurement sequence consists of four parts seen in Fig. 4.12. First the NV-centre's spin is initialized and the nuclear spin brought into a superposition state via a $\pi/2$-pulse. Afterwards the NV-centre's spin is flipped, depending on the nuclear spin-state, entangling the two:

$$|\Psi\rangle = (|e_\downarrow, n_\downarrow\rangle + |e_\uparrow, n_\uparrow\rangle)/\sqrt{2}\,. \tag{4.18}$$

Now the sample signal is encoded on the spins. There are two phase-accumulation steps, the second one is to cancel additional noise, so they can effectively be treated as one

phase-accumulation step:

$$|\Psi\rangle = (|e_\downarrow, n_\downarrow\rangle + e^{i\phi_1}|e_\uparrow, n_\uparrow\rangle)/\sqrt{2}\,. \tag{4.19}$$

A second set of CNOT-gates stores this quantum state on the memory spin. After this there is a phase for sample manipulation, which in this paper is used for a delay time, probing the samples T_2^*. This time is limited by the ^{15}N relaxation time, which can be on the order of minutes, leading to extremely high spectral resolution. In the next steps, the NV-spin is reinitialized and encoding steps are repeated, leading to a total state of:

$$|\Psi\rangle = (|e_\downarrow, n_\downarrow\rangle + e^{i(\phi_1+\phi_2)}|e_\uparrow, n_\uparrow\rangle)/\sqrt{2}\,, \tag{4.20}$$

where ϕ_1 and ϕ_2 are the phase accumulations of the first and second encoding steps respectively. Lastly this is read out using repetitive readout.

4.3.5. Proposed pulse sequences

Many of the major hurdles NV-NMR had to face have been circumvented by the development of these pulse sequences. Especially for micro-scale NMR, one challenge remains: To increase the external magnetic field for better signal amplitude and a higher chemical-shift resolution. One of the major challenges in doing this, is acquiring fast enough π-pulses, to be able to reach the inter-pulse-spacing necessary for the NMR-frequencies at these fields. For example, at a magnetic field of 1 T the NMR-resonance frequency of a proton will be:[115]

$$\begin{aligned} f_{\text{proton}} &= \gamma_p B_0 = 42.577\,\text{MHz} \\ \Rightarrow\ \tau &= 1/(4 f_{\text{proton}}) \approx 6\,\text{ns} \\ \Rightarrow\ \Omega &\approx 0.17\,\text{GHz}\,. \end{aligned} \tag{4.21}$$

Here we have assumed, that the π-pulses have to at be at least of the order of the interpulse spacing. Such fast pulses pose high technical challenges, though some solutions have been

proposed.

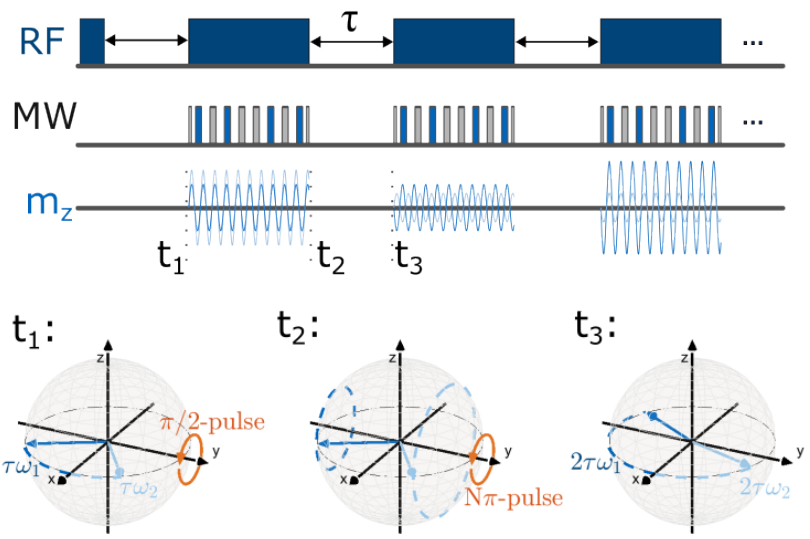

Figure 4.13.: **Amplitude-Encoded Radio Induced Signal sensing**
In regular intervals the sample-spins are strongly driven, leading to an oscillation of the sample-spin's m_z-component at the frequency Ω_{nuc}. Similar to CASR, equally spaced measurement blocks lead to identical phase-evolution in between measurements, and therefore an oscillation in the sensed field. This shown by the example of two spins with different frequencies ω_1 (dark blue) and ω_2 (light blue).

AERIS-sensing

The Amplitude-Encoded Radio Induced Signal (AERIS) sensing method has recently been proposed as a way of down-converting fast signals,[116] though it could also be used for up-conversion of extremely slow signals. The idea is to strongly drive the sample spins, to create an oscillating m_z-component, as seen in Fig. 4.13 a). This oscillation will be at the frequency of the nuclear Rabi-drive $\Omega_{nuc} \ll 10$ MHz. The amplitude of this oscillation will depend on the sample spin's initial azimuthal angle or phase. Multiple of these measurement blocks are spaced with equal separation τ. During this time, the sample spins evolve, which will shift the initial phase from measurement block to measurement block, which in turn leads to an oscillation in the recorded signal.

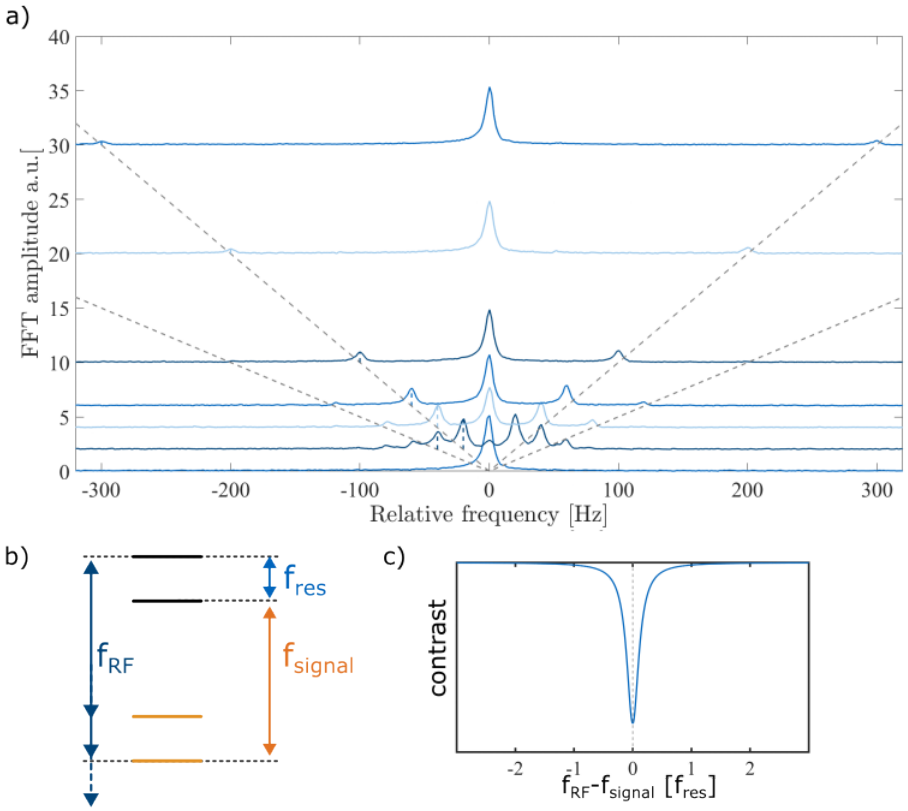

Figure 4.14.: **The quantum frequency mixer**
a): The Fourier-transform of several Floquet-driven water-NV-NMR experiment conducted in our experimental setup. The amplitude is held constant, at about 0.3 μT thought the driving frequency varies between 0 and 300 Hz. At lower driving frequencies several side-bands appear though the number and amplitude of visible side-bands decreases with the frequency. **b)**: The idea behind the quantum frequency mixer. Two strong driving fields f_{signal} and f_{RF} are necessary to utilize this technique. **c)**: A sketch of the experiment described in this section, sweeping f_{RF} yields a dip in the readout fluorescence at $f_{RF} = f_{signal} + f_{res}$.

Interestingly the components of $\vec{m}$ perpendicular to $\hat{m}_z$ will continue to oscillate with $\omega \gg \Omega$, and therefore cancel out during the measurement. So far this sequence has not been tested experimentally, which likely is due to the technical challenges of reaching fast enough nuclear Rabi-drives compared to the NV-centre's dephasing time. AERIS is discussed a little further in chapter 6, since, in the eyes of the author, it is the most promising technique for achieving high-field NV-NMR.

Quantum frequency-mixing

Several approaches to increase the bandwidth of possible measurement frequencies have been proposed building on Floquet-theory.[117–120] The most sophisticated scheme is the quantum frequency-mixer.[117] The idea is to exploit side-bands of strongly driven systems, as depicted in Fig. 4.14 a). If a spin-system, resonant at frequency f_{res} is driven with a frequency $f_{drive} \ll f_{res}$ which is parallel to B_0. This leads to an oscillation in the B_0-amplitude, and therefore a frequency-modulation of the spins-resonance. In the frequency-domain, this corresponds to multiple side bands, which are spaced $\pm k\, f_{drive}$ from f_{res}, where k is an integer,[118,120–122] as seen in Fig. 4.14. The amplitudes of these side-peaks, corresponding the transition probability, are dependent on the driving field strength $p_k = J_k(\Omega_{drive}/\omega_{drive})$ where J_k is the kth Bessel-function of the first kind.[118] This can be seen in Fig. 4.14 b), where a proton-NMR signal measured using the CASR sequence undergoes Floquet-driving with varying frequencies at constant amplitude.

In the quantum frequency-mixer the NV-state is driven both by the signal-frequency as well as a radio frequency f_{RF}, the latter being swept. If the resonance condition $f_{RF} = f_{signal} + f_{res}$ is met, a dip in the NV-fluorescence is seen.

Sadly this approach is likely not useful for NV-NMR, due to the necessary condition of $\Omega_{drive} \geq \omega_{drive}$. It is still an interesting approach and might spark new ideas for similar schemes applicable to NMR.

Continuous wave heterodyne sensing

This approach is quite different compared to every other measurement sequence discussed so far, since it is a continuous wave (CW) approach. This means the NV-drive as well as the re-polarizing laser are applied continuously, leading to a steady-state population, which is a result of the different constants, like the (in this experiment) constant Rabi-amplitude, T_1 and T_2 decay and the re-polarization rate.[123]

As seen in Fig. 4.15, if there is a signal-frequency f_{signal} close to the driving frequency

f_{drive}, the frequency seen by the NV-centre is a amplitude modulated driving frequency, whose amplitude modulation in turn modulates the CW-fluorescence. This happens, since the Rabi-contrast will fluctuate over time due to the modulated Rabi-drive amplitude. The recorded fluorescence-oscillation's amplitude depends on the signal's amplitude and the modulation-frequency on the signal-frequency.[123]

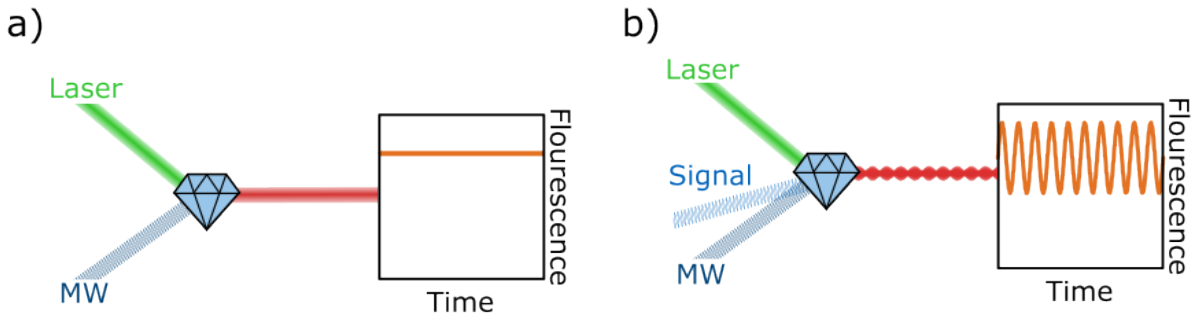

Figure 4.15.: **Continuous wave heterodyne sensing**
a): A CW sensing approach, where NV-drive and laser are constantly on, leading to a steady-state NV-fluorescence. **b)**: If in addition there is a oscillating signal-field, close to the drive frequency, the drive seen by the NV-centre will be amplitude modulated. This will lead to a oscillating steady-state fluorescence, which can be detected.

This sensing scheme is only of use to NMR-experiments, due to the challenge of having the signal frequency close to the NV-drive's frequency. Nevertheless, in my eyes the extremely loose hardware-constraints and the novel approach to AC-sensing make it an interesting candidate for a basis of future sensing schemes.

5. Previous NV-NMR experiments

In this chapter I introduce the three types of NV-sensors which have been used for AC-magnetic field sensing, discussing their fabrication, advantages, disadvantages and use-cases. I'll start from single NV-defects, talk about nano-scale NV-ensembles and finally turn to the micro-scale ensembles used in the experiments discussed in chapter 8.

5.1. Single NV-centres

The first experiments using NV-centres were conducted using individual defects a few nanometers below the surface.[46,57] Since they are literally of atomic size, single spins or small collections of spins can be probed, which gives unprecedented spatial resolution.

5.1.1. Fabrication

Since NV-centres occur naturally in diamond, any type can be used, scanning the surface until a NV-centre with good coherence-properties is found. For type I diamonds, the general density of impurities will still lead to bad coherence times, also the presence of the NMR-active ^{13}C isotope can skew the measurement-results. Therefore the targeted implantation of nitrogen-ions is desirable and has been shown to work with high accuracy.[124–127] Subsequent annealing of the diamond leads to NV-centre creation. Hereby vacancies, introduced during the highly energetic ion-implantation, diffuse towards the nitrogen.[48,49,128]

5.1.2. NMR-experiments

In 2012, Ohno et al. were the first to detect an NMR-signal using NV-centres,[129] even though it was one from the close by ^{13}C-nuclei within the diamond itself. One year later Mamin et al. and Staudacher et al. conducted the first NV-NMR experiments using external samples.[89,95] They measured the nano-scale NMR signal of various organic compounds, from the $\sim$ 5 nm detection volume of their sensors.

One year later the spatial resolution of NV-centres was brought to its maximum potential, when first the NMR-signal of four silicon nuclei[17] and afterwards the signal of a proton-spin were detected.[18] Two years later a single protein was tethered to the diamond surface and the NMR-signal of deuterium and ^{13}C-markers were measured.[16]

All these measurements suffered from the broad linewidth, connected with the solid-state nature of their samples as well as the NV-T_1 limited linewidth of nano-scale NV-NMR experiments.[92,94] As explained in the previous chapter Aslam et al. managed to increase the spectral resolution by several orders of magnitude, by using a clever scheme, in which NV-centre an nitrogen spin are entangled and the long lifetime of the nucleus is exploited.[114]

Single NV-centres have a unprecedented spatial resolution, but they suffers from long averaging times, due to the low photon count per measurement.[45,48,130] Also the spectral resolution-problem has not been fully solved. Even though the limitations due to the coherence-times involved has been solved,[114] the spectral lines are still limited by sample diffusion,[43,48,130,131] though different solutions have been proposed.[130,131]

5.2. Shallow NV-ensembles

Moving from single NV-centres to ensembles of NV-centres, which are positioned a couple nm below the surface means trading spatial resolution for averaging time. The sample-volume is now defined by the size of the laser-spot as well as the depth of the NV-layer, which typically ranges from ∼1-100 nm. In these measurements, millions of NV-centres can be controlled and read out simultaneously, effectively averaging them and therefore reducing the total measurement time by about $\sim \sqrt{N_{NV}}$. Compared to single NV-centres, the readout-fidelity or contrast between the two NV-centre states per NV-centre is much less ($\leq$ 14% compared to $\sim$ 30%),[43,48] mostly due to the four possible orientations of the NV-centre of which three only produce background fluorescence. Also the spin life- and decoherence-times will be smaller, due to the increased concentration of spin's in the diamond.

5.2.1. Fabrication

The fabrication of shallow NV-centre layers is akin to the one of single NV-centres. A (generally type IIa) diamond is implanted with N-ions. Finally annealing guides the vacancies towards the implanted nitrogen, mostly due to the stress caused by the nitrogen-atoms.[49,128] The thickness of the NV-layer is determined by the ion-implantation energy.[49,132]

5.2.2. NMR-experiments

The first achievement of shallow NV-ensembles was the detection of multiple nuclear species simultaneously,[133] while drastically reducing the averaging time compared to single NV-centres. In addition they introduced the wide-field approach, when performing optically-detected MRI for the different samples.[133] Further experiments improved on this microscopy technique.[76,134] Recently efforts have been made, to further sharpen the diffusion limited lines. Here Liu et al.[15] studied the time dynamics of a self assembled mono-layer, which was tethered to the diamond surface. This approach leaves the target molecules mobile enough, to average the dipolar-coupling broadened lines,[15,92,94] while their motion is still to limited to

diffuse out of the NV-centre's area of sensitivity.

Similar to shallow NV-ensembles still have to beat the diffusion limited line-widths, to improve their spectral resolution by orders of magnitude for chemical-shift resolution. Never the less, in the case of inherently 2-dimensional samples, like 2D-materials or surface interactions, the ability of probing the dynamics during chemical reactions with NMR-active nuclear-species, with or without chemical-resolution, can be of great advantage.

5.3. Micro-scale NV-ensembles

Single cell studies using NMR have been a continuous goal for the NV-community.[19,87,135,136] Most mammalian cells are of the order of $\sim$10 μm, therefore similar sized NV-layers have been utilized to work towards this goal. Due to the, increased number of defects in these layers, the fluorescence light or equivalent number of averages compared to shallow NV-ensembles is increased quite drastically. Nevertheless, due to their detection of Boltzmann nuclear polarization, detecting NMR-signals needs a comparable amount of time as nano-scale NMR, if the sample is not hyperpolarized.[19,87,97]

5.3.1. Fabrication

The fabrication of these ensembles differs drastically form the shallow and single NV-centres. Due to the much thicker NV-layers on the diamond surface, the energy necessary for ion-implantation would cause too much damage to the diamond and would render them useless for magnetometry experiments.[49] Instead the micro-scale layers are grown in a CVD process on top of the typically type IIa diamond, and later polished to the desired thickness of $\sim$1-100 μm. Since no vacancies were introduced during a ion-implantation step, electron-irradiation of the diamond is necessary to do so. Finally the annealing step is still necessary to bring vacancies close to the nitrogen incorporated in the diamond.

5.3.2. NMR-experiments

The major advantage of the micro-scale NV-NMR experiments is its high spectral resolution, which has been shown for the first time in 2018 by Glenn et al.[87] This allows for chemically resolved NMR-spectroscopy of pl (10^{-12} l) volume samples.[44,87,97] In addition to this, the technique lends itself to be used with micro-fluidics. First attempts have been promising,,[136,137] and the first well defined microfluidic-NV-setup showing chemical resolution has been used in our group with great success.[86,138]

If the goal of single-cell NV-NMR is to be reached, some major challenges still have to be overcome. The reported sensitivities[87,108,136] are still not good enough to detect metabolites, even in high concentrations.[139] Additionally, it has not been shown how and if cells will survive the high microwave and laser-powers used in NV-NMR experiments.

Part II.

Results

6. Simulating NV-NMR

Micro-scale NMR-detects the sum of all B_z-components of the dipolar field of each sample-nucleus. Since the dipolar field is highly geometry dependent, it is to be expected, that the NV-NMR signal is too.[88] The geometry dependence of these fields has been studied in conventional NMR, where the setup normally is insensitive to these dipolar-effects,[140,141] though it can be made sensitive to dipolar interactions via clever pulse-sequence design.[142,143] A similar geometry-dependence exists though, which is defined via the pickup-coil and has been well investigated.[144] In addition, NV-NMR is not the first technique to use one spin-ensemble as a sensor for a secondary spin-ensemble,[145,146] in which similar dependences were investigated.

In this chapter I will first explain the origin and importance of this geometry dependence, afterwards I will explain a numerical way of simulating the signal strength. I will discuss the results for several geometries of importance and extend the simulations into the time domain. Finally I will introduce gradients and their effect on our signal including some unexpected ways to exploit them.

6.1. Sample geometry in NV-NMR

The NV-NMR signal obviously depends strongly on factors like sample-spin concentration and polarization, but also the geometry of the experiment plays an important role. One example, that has already been mentioned is the detection volume of the NV-centre, which is on the order of the NV-centre's depth below the diamond surface. In this section I will give an analytical explanation of the influence sample geometry can have on the signal and then

explain how to simulate this using a Monte Carlo approach. This section is partially adapted from Bruckmaier et al.[88]

6.1.1. Analytical derivation of the geometry factor

The complex interplay between the NV-orientation, i.e. the angle between the direction of measurement and the diamond surface, as well as the direction of the sample-magnetization is hard to grasp intuitively (as seen in Fig. 6.1 a)). The NV-orientation can vary, depending on the diamond cut and the sample magnetization oscillates about $\hat{B}_0$. The basic interaction originates from the magnetic field of a dipole, which can be written as already seen in equation 4.1:

$$\vec{B}_{spin} = \frac{\mu_0}{4\pi} \frac{3\hat{r}(\vec{m} \cdot \hat{r})}{r^3} , \tag{6.1}$$

where μ_0 denotes the magnetic permeability, $\vec{m}$ is the magnetic moment of the precessing sample-spin and $|r|$ and $\hat{r}$ are the distance and direction between the sample spin and the NV-center measuring. Since, in the end the NV-center measures the difference in Zeeman-splitting between the $|\pm 1\rangle$ and $|0\rangle$ state, we are only sensitive along the $\hat{B}_0 \equiv \hat{B}_z$ direction:

$$\vec{B}_{\text{spin},||} = \frac{\mu_0}{4\pi} \frac{3\hat{r}(\vec{m} \cdot \hat{r})}{r^3} \cdot \hat{B}_0 . \tag{6.2}$$

Assuming the sample is uniformly polarized, we can integrate the dipolar field over the sample volume to obtain our NMR-signal $S(t)$:

$$\begin{aligned} S(t) &= \int \rho_{\text{therm}} \left(\vec{B}_{\text{spin},||}(\vec{r}, t) \cdot \hat{B}_0 \right) dV \\ S_{\max} &= \frac{\mu_0}{4\pi} \rho_{\text{therm}} \overline{|m_{\max}(t)|} \int \left[\frac{3\hat{r}\,(\hat{r} \cdot \hat{m}_{\max}) - \hat{m}_{\max}}{r^3} \right] \cdot \hat{B}_0 \, dV , \end{aligned} \tag{6.3}$$

where ρ_{thermal} is the concentration of thermally polarized spins within our sample and $\hat{m}_{\max}$ is the direction of the magnetic moment, at which the signal amplitude is maximal. $\overline{|m_{\max}(t)|}$ is the magnetic moment's mean magnitude along $\hat{m}_{\max}$.

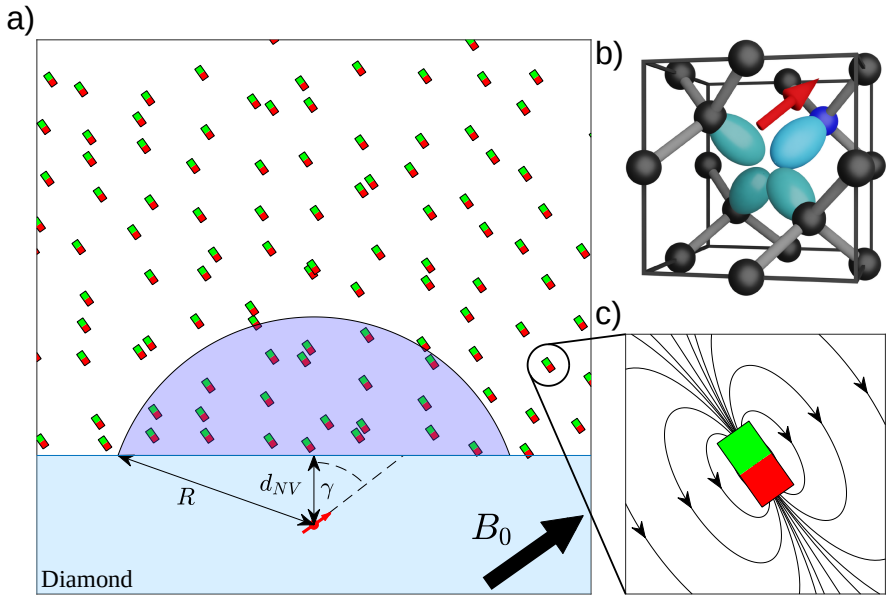

Figure 6.1.: **Schematic of a micro-scale NV-NMR experiment**
a): The diamond is shown as a light blue area with a red arrow indicating the NV center, which is located at a depth d_{NV} below the diamond surface. The darker blue circular-cap of radius R is the area out of which $> 50\%$ of the NMR signal originates. The miniature bar magnets depict the polarized portion of the precessing nuclear sample spins. **b)**: A model of the NV-center in diamond, with the NV-orientation displayed as a red arrow. **c)**: The dipolar field of one of the precessing sample spins.
This figure was taken from Bruckmaier et al.[88]

Now the NMR-signal can be split up into two parts $S = K \cdot G$, the first contains the geometry-independent information about the experiment like the spin density or the magnetic field amplitude:

$$K = \frac{\mu_0}{4\pi} \rho_{\text{therm}} \overline{|m_{\max}(t)|} \,. \tag{6.4}$$

The second is the geometry-factor, containing all the information about the sample geometry, as well as the interplay of the spin-orientations:

$$G = \int \left[\frac{3\hat{r}\,(\hat{r}\cdot\hat{m}_{\max}) - \hat{m}_{\max}}{r^3} \right] dV \ . \tag{6.5}$$

Since the magnetic moment precesses after a $\pi/2$-pulse, $\hat{m}_{\max}$ and $\hat{B}_0$ are orthogonal:

$$\begin{aligned} G &= \int \left[\frac{3\hat{r}\,(\hat{r}\cdot\hat{m}_{\max}) - \hat{m}_{\max}}{r^3} \right] \cdot \hat{B}_0 \, dV \\ &= 3 \int \frac{(\hat{r}\cdot\hat{B}_0)(\hat{r}\cdot\hat{m}_{\max})}{r^3} \, dV \ . \end{aligned} \tag{6.6}$$

At this point the resulting signal depends on the sample geometry, and the analytical evaluation might be quite tedious if at all possible, which is the motivation for the numerical simulations discussed later in this section. Further evaluating the simple case of an infinite sample volume, we can integrate over the spherical cap depicted in Fig. 6.1:

$$\begin{aligned} G_{\text{halfspace}} = 3 \int_{d_{NV}}^{R} \int_{0}^{\theta_{\max}} \int_{0}^{2\pi} & \sin\theta \\ & \frac{(\sin\gamma\sin\theta\cos\phi + \cos\gamma\cos\theta)(\cos\gamma\sin\theta\cos\phi - \sin\gamma\cos\theta)}{r} \, d\phi\, d\theta\, dr \\ = \pi \ \sin\gamma \ \cos\gamma & \ \frac{2R^3 - 3d_{NV}R^2 + d_{NV}^3}{R^3} \ , \end{aligned} \tag{6.7}$$

where we have defined $\hat{B}_0 = \begin{pmatrix} \sin\gamma \\ 0 \\ \cos\gamma \end{pmatrix}$ and therefore $\cos(\theta_{\max}) = d_{NV}/r$. Here d_{NV} is the NV-centre's distance below the diamond surface and γ is the angle between the NV-center orientation end the diamond surface normal. When taking the geometry-factors limit for $R \to \infty$, it converges to:

$$\begin{aligned} G_{\text{halfspace},\infty} &= \lim_{R\to\infty} \pi \ \sin\gamma \ \cos\gamma \ \frac{2R^3 - 3d_{NV}R^2 + d_{NV}^3}{R^3} \\ &= 2\pi \ \sin\gamma \ \cos\gamma \ . \end{aligned} \tag{6.8}$$

One example of the strong sample geometry dependence can easily be seen here: If $\theta_{\max}$ would be constant, the resulting geometry would be cone-shaped and our geometry-factor would be:

$$G_{\text{cone}} = \pi \ \sin\gamma \ \cos\gamma \ \sin\theta_{\max}{}^2 \ \cos\theta_{\max} \ \log\left(\frac{R}{d_{NV}}\right). \tag{6.9}$$

Again taking the limit for $R \to \infty$, the geometry factor diverges logarithmic, emphasising the strong geometry-dependence of micro-scale NV-NMR experiments:

$$G_{\text{cone},\infty} = pi \ \sin\gamma \ \cos\gamma \ \sin\theta_{\max}{}^2 \ \cos\theta_{\max} \ \log\left(\frac{R}{d_{NV}}\right) = \infty. \tag{6.10}$$

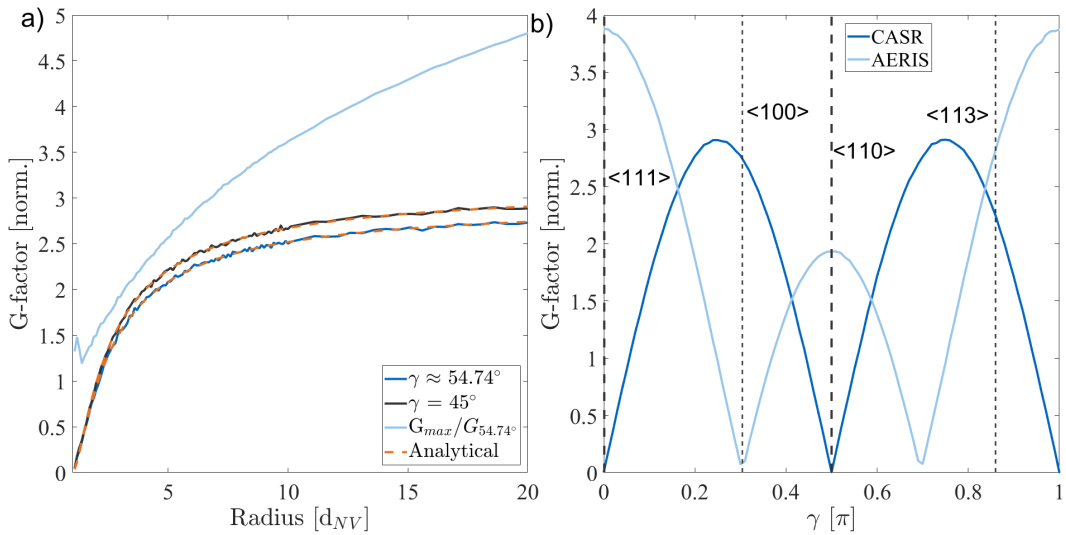

Figure 6.2.: **The geometry factor of a half space filled with sample volume**
a): Analytical (dashed) as well as simulated (solid lines). Once with $\gamma = 54.74°$, $\gamma = 45°$ and once the signal enhancement due to a theoretical maximum geometry factor described in section 6.3.1. **b)** Simulations of the geometry factor as a function of the angle γ, once for the sample filled half-space described here (light blue) and once for the AERIS-protocol (dark blue) described in section 4.3.5.

6.1.2. Dipolar fields and diamond cuts

Looking at equation 6.8, which displays the most commonly used micro-scale geometry, a couple of things are to note:

1. The NMR signal converges (grows logarithmic) as a function of R so increasing the sample-volume yields drastically diminishing returns.
2. For $R \gg d_{NV}$, the signal size is independent of the depth of the NV-center.
3. There is a strong dependence on the angle between the NV-orientation and the diamond surface, which is dependent on the diamond cut, reaching its maximum at $\gamma = 45°$.

A consequence of this angle dependence can also be seen in Fig. 6.3. $\langle 110 \rangle$ and $\langle 111 \rangle$-diamonds are not able to sense thermal polarization with the normal detection schemes, i.e. the CASR-scheme described in section 4.2. Interestingly, as seen in Fig. 6.2, the AERIS-scheme is most sensitive for $\langle 111 \rangle$-diamonds. This stems from the fact, that during this scheme the fast oscillating x and y components of the magnetization do not contribute to the detected signal.[116] For the $\langle 100 \rangle$-diamonds used in the experiments in this thesis, the signal due to thermal polarization can now be calculated with $G = 2\sqrt{2}\pi/3$. Assuming a water sample at $T = 300$ K and $B_0 = 0.2$ T, with $\overline{|m_{\max}(t)|} = h\gamma_p/\pi$, the geometry-independent part can be estimated to be:

$$K = \frac{\mu_0}{4\pi} \frac{h\gamma_p}{\pi} \frac{\gamma_p h \mathrm{B}_0}{2 k_B T} \rho_{\text{proton}} \approx 80\,\mathrm{pT}\,, \tag{6.11}$$

where T is the temperature, μ_0 the magnetic vacuum permeability h is the Planck-constant and k_B is the Boltzmann-constant leading to a total signal of $S \approx 240\,\mathrm{pT}$.

As mentioned, in the reality of our experiments we use Overhauser-nuclear-polarization to enhance the signal amplitude. Since the amplification of this procedure is strongly dependent on multiple variables like the external magnetic field, concentration of radicals and target molecules,[19] the resulting signal strength can only be estimated. Previous publications estimated the hyperpolarized signal in similar conditions as in our experiment to be a factor 100-200 greater than that of the thermal polarization in pure water at room temperature.[19]

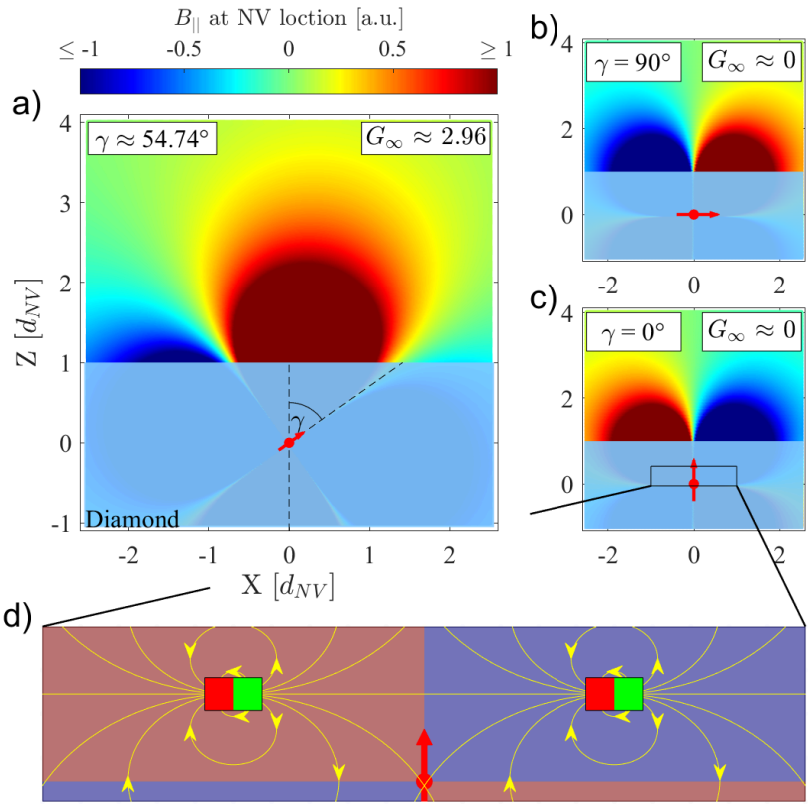

Figure 6.3.: **The diamond-cut dependence of NV-NMR signals**
A sensitivity map of a single NV-center sensing thermal polarization. The color indicates the signal contribution from the respective areas. **a)**: The case of a $\langle 100 \rangle$-diamond, close to maximum signal. **b)-c)**: For $\langle 110 \rangle$ and $\langle 111 \rangle$-diamonds, the same amount of spins have positive and negative B_0-contributions at the NV-center, cancelling each other out. **d)**: A sketch visualizing the magnetic field cancellation of the red and blue areas.

6.1.3. Monte-Carlo simulations of dipolar fields

For the estimation of more complex structures, the analytical derivation of the geometry factor is not as straight forward. A powerful tool to solve this problem is the Monte-Carlo approach. Just by defining a sample-volume V_{sample} and a NV-VolumeV_{NV}, we can simulate the analytical result to arbitrary accuracy. The method relies on the random sampling of N

target locations within V_{sample} and M NV-center locations within V_{NV}. Now the magnetic field projection along $\hat{B}_0$ from each target at the location of each NV-center can be calculated and averaged. Since the task of simulating each individual spin for a sample volume of this size is computationally daunting, each of these targets refers to a set of spins within a volume V_{sample}/N behaving identically. With increasing N, the simulation will become more and more accurate. With this the geometry factor can be approximated as:

$$G = 1/K \sum_{k=1}^{K} \left[\frac{V_{\text{sample}}}{M_k \, N_k} \sum_{m=1}^{M_k} \left(\sum_{n=1}^{N_k} \frac{3\hat{r}_{m,n} \left(\hat{r}_{m,n} \cdot \hat{m}_{\text{max}} \right) - \hat{m}_{\text{max}}}{r_{m,n}^3} \cdot \hat{B}_0 \right) \right] , \tag{6.12}$$

where $r_{m,n}$ is the distance between target n and NV-center m and $\hat{r}_{m,n}$ the normalized direction between the two. K indicates the number of averages, in between which the individual N_k target and M_k NV-center locations are randomized.

6.1.4. Different geometries

The geometries investigated here are each motivated by different samples of interest in NV-NMR, the results of which can be seen in Fig. 6.4. The cone-shape is the only exception, it has already been discussed briefly in the previous section.

Spherical volumes

The sphere is motivated by two distinct samples of interest. On one side single suspension cells are of approximately spherical shape. In the case of mammalian cells they have a typical diameter of of ~ 10 μm.[147] The second sample of interest are micro-droplets, small droplets of a sample-water solution in a fluorinated oil. Due to their robustness and high controllability, both in size and within microfluidic channels, they are widely used in life sciences.[148] As seen in Fig. 6.4 b), if the sphere is placed above the NV-centres, it avoids the areas of negative signal contribution, overall increasing the geometry factor.

Cylindrical volumes and sheets

Adherent cells can be approximated using a cylindrical shape, neglecting the cell-nucleus. In addition to adherent cells, NV-hyperpolarization can create such sample geometries. There has been continuous interest in using NV-centers for hyperpolarization[91,98–100] and the resulting hyperpolarized sheet of the sample volume is estimated to by ~ 1 μm thick,[98,99] due to diffusive spreading of the hyperpolarized molecules and of course of the size of the laser spot used.

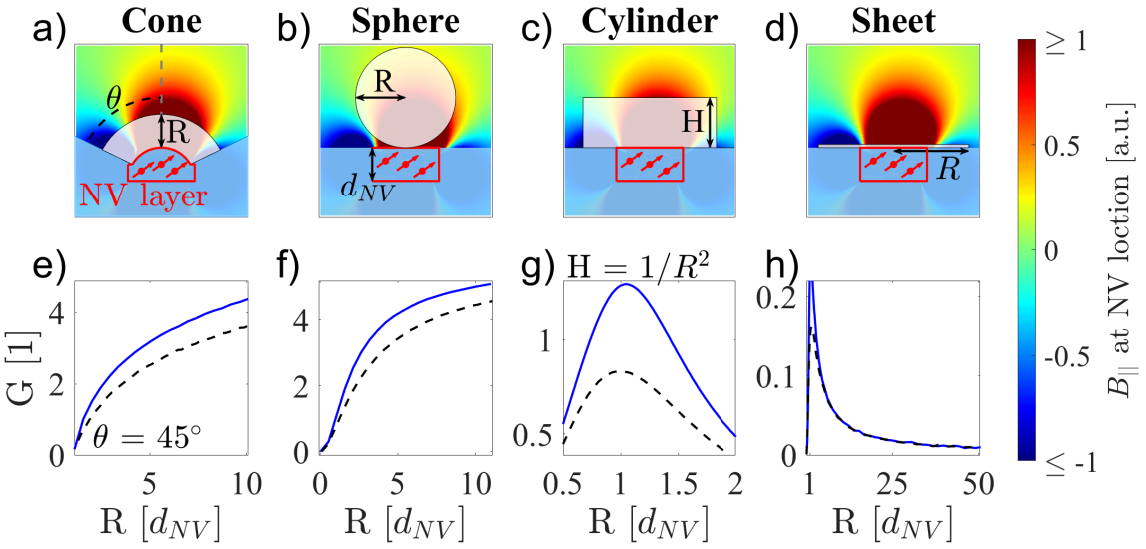

Figure 6.4.: **The geometry factor for different sample geometries**
a) -d): Schematic display of the simulation geometry. The radius R is swept and the NV-ensemble is contained within a cylindrical volume of radius 1 d_{NV} and depth 1 d_{NV}. **e) -h))**: Results of the simulations, in blue the average geometry-factor for the ensemble case is displayed and the dashed black lines are the results for a single NV-center. The NV-ensemble improves the average geometry-factor compared to the single NV-center case, since the average NV-center is closer than d_{NV} to the surface and the limit of $R \gg d_{NV}$ is not reached in most of these simulations.

In Fig. 6.4 c) and d) these two cases are displayed. The cylinder's volume in g) is kept constant while for the cylinder in h) the height is kept constant and the radius is swept.
Due to the smaller volumes in these samples, the geometry factor tends to be smaller than that of the half-space. In the limit of $H, R \to \infty$, the geometry factor converged to a similar

value as that of the half-space at $G_{\text{cylinder},\infty} \approx 3$.

NV-ensemble depth and laser spot size

Not only the signal size but more importantly the signal to noise ratio (SNR) is to consider when talking about NMR experiments. The SNR is a measure of how strong the NMR-signal is and is defined as the ratio of the amplitude of a spectral component and the standard deviation of the noise floor, discussed in more detail in section 7.1.2. The number of averages N improves the SNR as SNR$\propto \sqrt{N}$. Since each individual NV-center read out simultaneously can be considered averaging: SNR$\propto G_{\text{average}}\sqrt{N_{NV}}$, so assuming the average geometry factor being constant, increasing the number of NV-centres is highly beneficial.

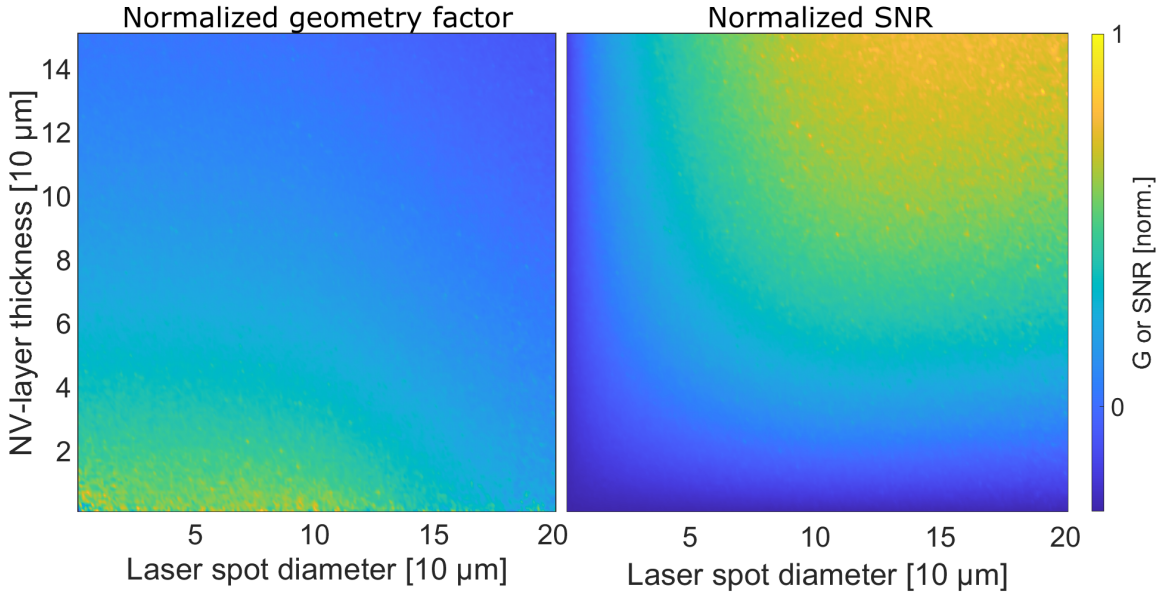

Figure 6.5.: **The different scaling of the geometry factor and the SNR with the number of NV-centres**
The normalized relative geometry factor (**a)**) and SNR (**b)**) of our microfluidic channel as a function of the laser spot diameter and NV-layer thickness.

In Fig. 6.4 the average geometry-factor is displayed, which corresponds to the average signal size. If we want to optimize the geometry to improve the SNR, we need to consider the increased averaging as a function of the excited NV-volume. An example can be seen in Fig.

6.5, where the once the geometry factor (a)) and once the SNR (b)) of a microfluidic channel of dimension 1000 μm x 80 μm x 100 μm is investigated as a function of a varying laser spot size and NV-ensemble depth. The difference is quite astonishing, while the geometry factor decreases fast as a function of both the NV-layer thickness as well as the laser spot diameter, the SNR increases with both. Depending on the experiment, spatial resolution might be of importance to, which will of course be the highest for small laser spots and NV-layers. In the end the optimal conditions for each individual experiment have to be decided on a case by case basis.

6.2. Time-domain simulations of NV-NMR

In a next step the geometry factor simulations can be extended into the time domain. Continuing from equation 6.12, assuming a homogeneous polarization this equation is valid for all orientations of $\hat{m}$, not only $\hat{m}_{max}$. Using the above definition of $\hat{B}_0 = \begin{pmatrix} \sin(\gamma) \\ 0 \\ \cos(\gamma) \end{pmatrix}$ we can substitute:

$$\hat{m}_{max} \rightarrow \hat{m}(t) = \begin{pmatrix} \cos(\gamma)\cos(2\pi\, t B_0 \gamma_{proton}) \\ \sin(2\pi\, t B_0 \gamma_{proton}) \\ -\sin(\gamma)\cos(2\pi\, t B_0 \gamma_{proton}) \end{pmatrix} . \tag{6.13}$$

Meaning, $\hat{m}(t)$ is oscillating in the plane perpendicular to B_0. If we want to simulate an experiment using the CASR approach, we can only look at the beating between the NMR-frequency and our π-pulse spacing τ:

$$\hat{m}(t) = \begin{pmatrix} \cos(\gamma)\cos(2\pi t(B_0\gamma_{proton} - \frac{1}{4\tau})) \\ \sin(2\pi(B_0\gamma_{proton} - \frac{1}{4\tau})) \\ -\sin(\gamma)\cos(2\pi t(B_0\gamma_{proton} - \frac{1}{4\tau})) \end{pmatrix} = \begin{pmatrix} \cos(\gamma)\cos(\phi(t)) \\ \sin(\phi(t)) \\ -\sin(\gamma)\cos(\phi(t)) \end{pmatrix} . \tag{6.14}$$

The resulting oscillation can be seen in Fig. 6.6 a), the four lobes, seen in the two dimensional

plots before are now visible in the three dimensional oscillation in b).

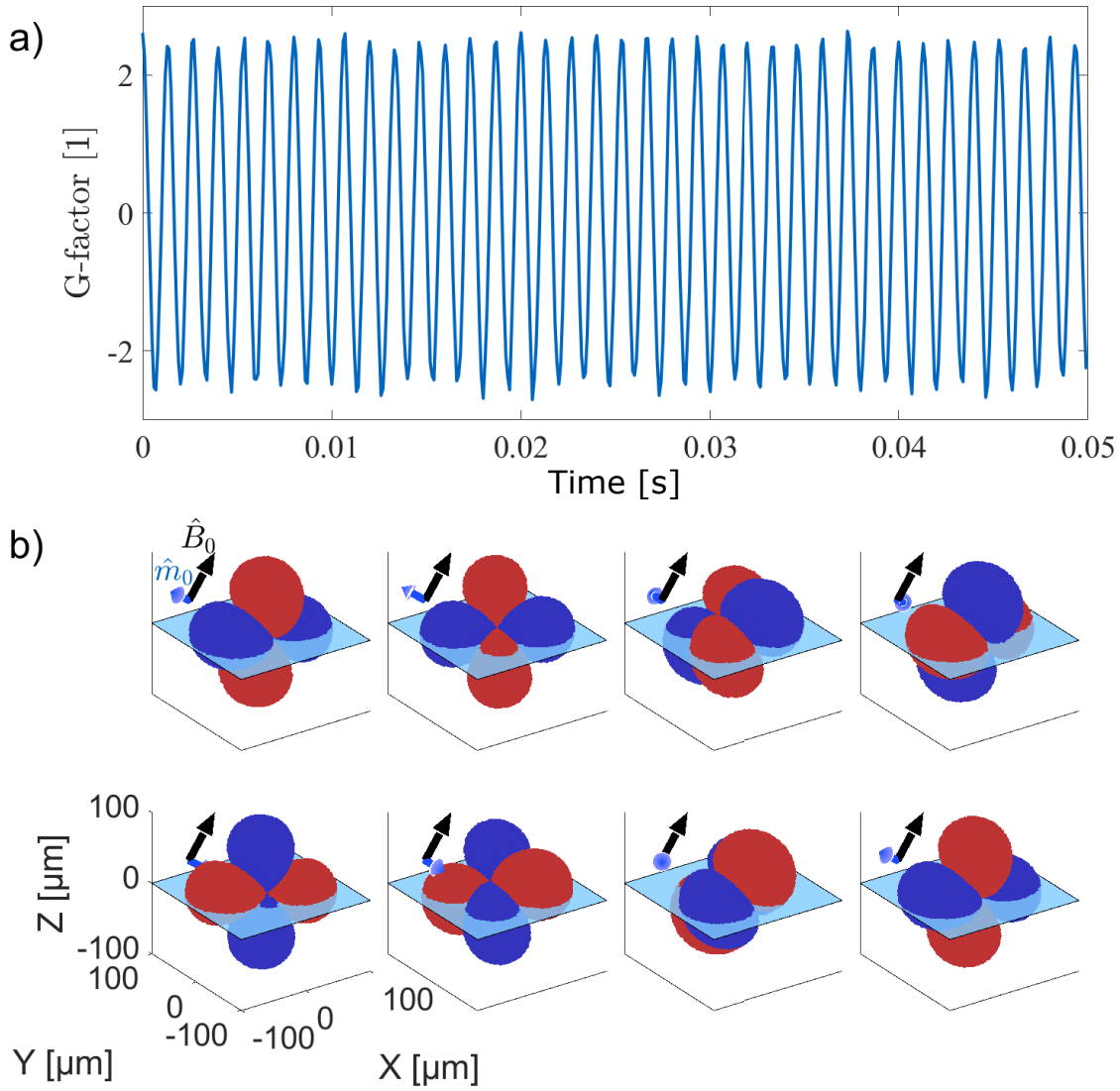

Figure 6.6.: **The oscillation of the geometry factor visualized**
a): The oscillation of the geometry factor due to the oscillating magnetization as a function of time. **b)**: The total sample volume is divided into four quadrants with opposite sign looking similar to a d-orbital, originating from the double dot-product in equation 6.2. Positive signal contribution is displayed in red and negative signal contribution in blue. These quadrants rotate with time about the NV-orientation, leading to an oscillating geometry factor. Only the 10 % of all randomly sampled positions with the highest contribution ($|\vec{B}_{i,0}|$) are shown at different times t.

Introducing gradients

Since the experimental goal of this thesis are pulsed field gradient (PFG) experiments, the next natural step is to simulate the effect of a linear B_0 gradient. For this each individual target volume is assigned its own magnetization-vector $\hat{m}_i(t)$ with phase $\phi_i(t)$, which depends on the external gradient $\vec{g}$ as:

$$\phi_i(t) = 2\pi t((B_0 + \vec{g} \cdot \vec{r}_i)\gamma_{proton} - \frac{1}{4\tau}) \, . \tag{6.15}$$

Since each sample volume's magnetization $\hat{m}_i$ now rotates at its own frequency, they will start to dephase, leading to an decaying envelope of the the oscillating geometry factor, as seen in Fig. 6.7. The effect of a gradient of duration δ is characterized by its b-value $b = 2\pi\gamma\delta$g which describes the relative dephasing of the whole sample. It should be noted, that this dephasing happens in a "coherent" way, which can be seen in Fig. 6.7 b) where a double-helix like structure of different signed geometry-factor is created by the gradient along its direction. The frequency of this helix depends on the relative dephasing. It can be "unwound" again, by applying a gradient with the same amount of dephasing but opposite sign.

A second way of rephasing the spins is the Hahn-echo experiment. Including a π-pulse, after the signal has decayed will negate all the dephasing due to constant gradients. The π-pulse can be implemented in the simulation by:

$$\phi_{\text{after}\,\pi} = -(\phi_{\text{before}\,\pi} + 2\alpha) \, , \tag{6.16}$$

where α is the azimuthal angle of the axis of rotation in the Bloch-picture, relative to the x-axis.

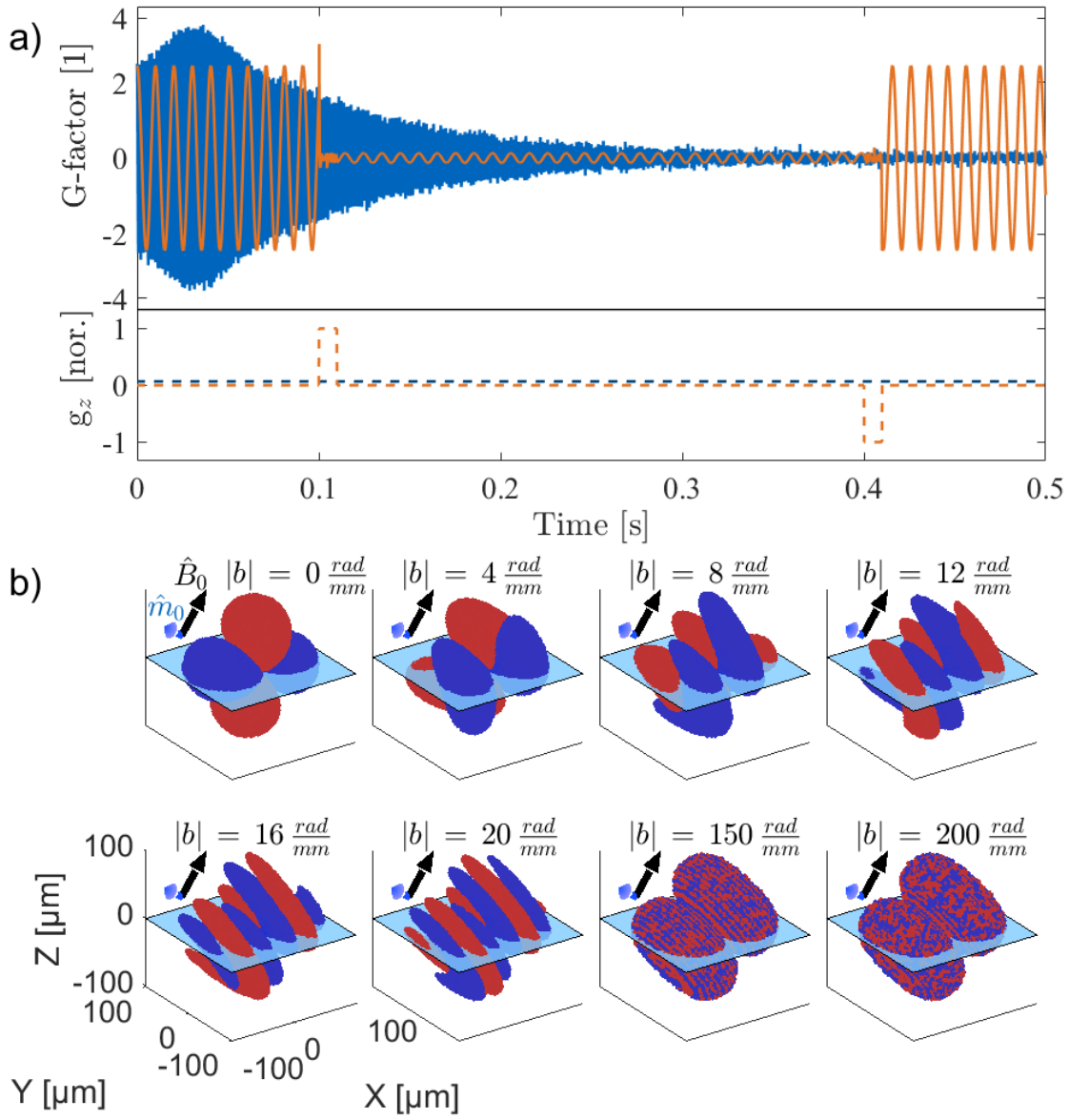

Figure 6.7.: **Effects of a linear $\hat{B}_0$ gradient on the geometry factor**
a): Simulation of a decaying oscillating geometry factor of a NV-NMR experiment as a result of an applied z-gradient, of strength 0.015 T/m (dark blue). The geometry factor is reduced to ∼0 by a short but strong gradient pulse, after 0.3 s the same gradient pulse with opposite sign is applied, reviving the signal (orange). The two oscillations have different frequency for better visibility. **b)**: With time, the spins dephase along a constant gradient (here $\hat{g}||\hat{B}_0$), resulting in a double-helix like structure with each helix having a geometry factor of opposite sign. It should also be noted, that the images are in the rotating frame of $\hat{m}$, so the effects seen are solely due to the gradient.

Simulating a pulsed gradient spin echo experiment

This controlled rephasing is only possible, if all sample-volumes stay in their respective places. In a real NMR-experiment, this will not be the case, since any liquid sample will have self-diffusion. This can be modeled by implementing a random walk for each of the target volumes.[92,149] For this, each of the sample volume moves a certain amount $\Delta\vec{r}_{i,n}$ in each discrete time step t_n:

$$\vec{r}_{i,n} = \vec{r}_{i,n-1} + \Delta\vec{r}_{i,n} = \vec{r}_{i,n-1} + \hat{r}_{i,rand} r_{i,gauss} \sqrt{6\mathrm{D}t_n} \,, \tag{6.17}$$

where D is the free diffusion constant of the sample, defined as $D = \frac{\langle \Delta x^2 \rangle}{t}$, where $\langle \Delta x^2 \rangle$ is the mean-squared particle displacement. $r_{i,gauss}$ is a randomly chosen number of a Gaussian distribution with standard deviation $\sigma = 1$ and $\hat{r}_{i,rand}$ is a random uniformly distributed direction.[149] In addition to this discrete random walk, border constraints of the total sample volume can be chosen, at which the diffusing sample is reflected inwards, limiting the maximal distance particles can diffuse.

Here the question arises, how much each randomly diffusing volume dephases during each time step, since it is diffusing through a magnetic field gradient. Luckily, the dephasing can be made time step-independent[149] and the total phase accumulation for each individual sample during one time step is:

$$\phi_{i,n} = \phi_{i,n-1} + \Delta\phi_{i,\text{const.}} + \Delta\phi_{i,\text{gradient}} + \Delta\phi_{i,\text{corr.}} + \Delta\phi_{i,\text{CASR}} \tag{6.18}$$

$$\Delta\phi_{i,\text{const.}} = 2\pi t_n \gamma_{\text{proton}} B_0 \tag{6.19}$$

$$\Delta\phi_{i,\text{gradient}} = 2\pi t_n \gamma_{\text{proton}} (\vec{g} \cdot (\vec{r}_{i,n}/2 - \frac{3}{2}\vec{r}_{i,n-1})) \tag{6.20}$$

$$\Delta\phi_{i,\text{corr.}} = 2\pi t_n \gamma_{\text{proton}} (|\vec{g}|\, r_{i,gauss} \sqrt{\mathrm{D}/2\, t_n^3}) \tag{6.21}$$

$$\Delta\phi_{i,\text{CASR}} = -2\pi t_n/(4\tau) \,, \tag{6.22}$$

where $\Delta\phi_{i,\text{const.}}$ is the phase accumulation due to the constant field B_0, $\Delta\phi_{i,\text{gradient}}$ is the

gradient induced dephasing of the average sample position during the time step, $\Delta\phi_{i,\text{corr.}}$ is a correction of the gradient induced dephasing due to the strong time-step dependence following Gudbjartsson et al.[149] and $\Delta\phi_{i,\text{CASR}}$ gives the relative phase accumulation in the CASR sequence.

With this a whole pulsed gradient spin echo (PGSE) experiment can be simulated as seen in Fig. 6.8. In this experiment two identical gradient pulses of dephasing b are separated by a time Δ and a π-pulse in between. The echo in the experiment diminishes as the dephasing of the gradient pulses increases, depending on the displacement of the sample volumes. The experiment is explained in detail in chapter 8.

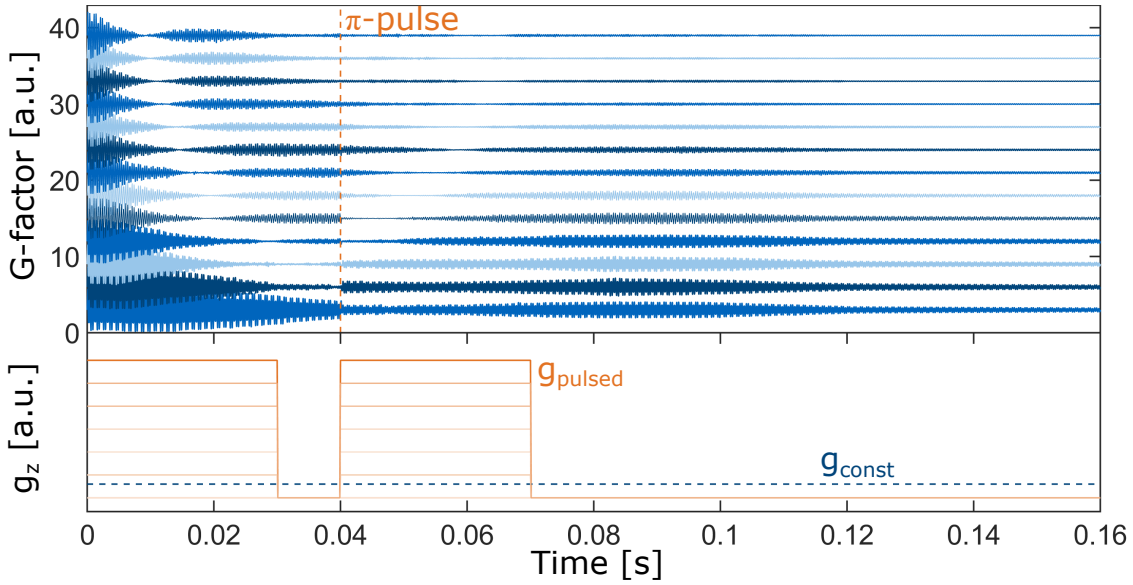

Figure 6.8.: **Simulation of a PGSE experiment**
a): The oscillating geometry-factor of a PGSE-experiment. The echo amplitude diminishes as the gradient strength increases, since the sample volumes rephase less. The applied π-pulse is indicated with a orange, dashed line. **b)**: The applied gradients during the experiment, in shades of orange, the pulsed gradients of varying amplitude, in dark blue a constant background gradient.

6.3. Gradient-enhanced NV-NMR and other interesting results

Several interesting observations have been made using these simulations. Some of these have been investigated qualitatively in NV-NMR experiments, but non of them have been understood quantitatively or been published at the time of this thesis.

6.3.1. Maximal geometry factor

The geometry factor can be improved, by dephasing the spins in a controlled manner. This can be easily seen from equation 6.2:

$$\vec{B}_{spin} = \frac{3(\hat{r} \cdot \hat{B}_0)(\vec{m} \cdot \hat{r})}{r^3} \, . \tag{6.23}$$

Applying a gradient, shifts the magnetization vector at each position $\vec{r}$. To find an upper bound, a position dependent, maximum contribution is needed. When maximizing $\hat{m} \cdot \hat{r}$:

$$\vec{B}_{spin,max} = \frac{3(\hat{r} \cdot \hat{B}_0)|\hat{r} - \hat{B}_0(\hat{B}_0 \cdot \hat{r})|}{r^3} \, , \tag{6.24}$$

the contribution is maximal in amplitude, but the direction will vary according to $\hat{r} \cdot \hat{B}_0$, this can be compensated, by flipping $\hat{m}$ according to the sign of this dot product, though taking $|\hat{r} \cdot \hat{B}_0|$ is equivalent. This leads us to the maximum achievable geometry factor:

$$G_{max} = \int \frac{3|\hat{r} \cdot \hat{B}_0| \, |\hat{r} - \hat{B}_0 \, (\hat{B}_0 \cdot \hat{r})|}{r^3} dV \, . \tag{6.25}$$

A comparison between the maximum and the current geometry factor can be seen in Fig. 6.2. It should be noted that this geometry factor hardly seems achievable, since the relative phase does not vary smoothly as a function of position, but has a sudden phase flip to cancel out the change in sign from the first dot-product $\hat{r} \cdot \hat{B}_0$.

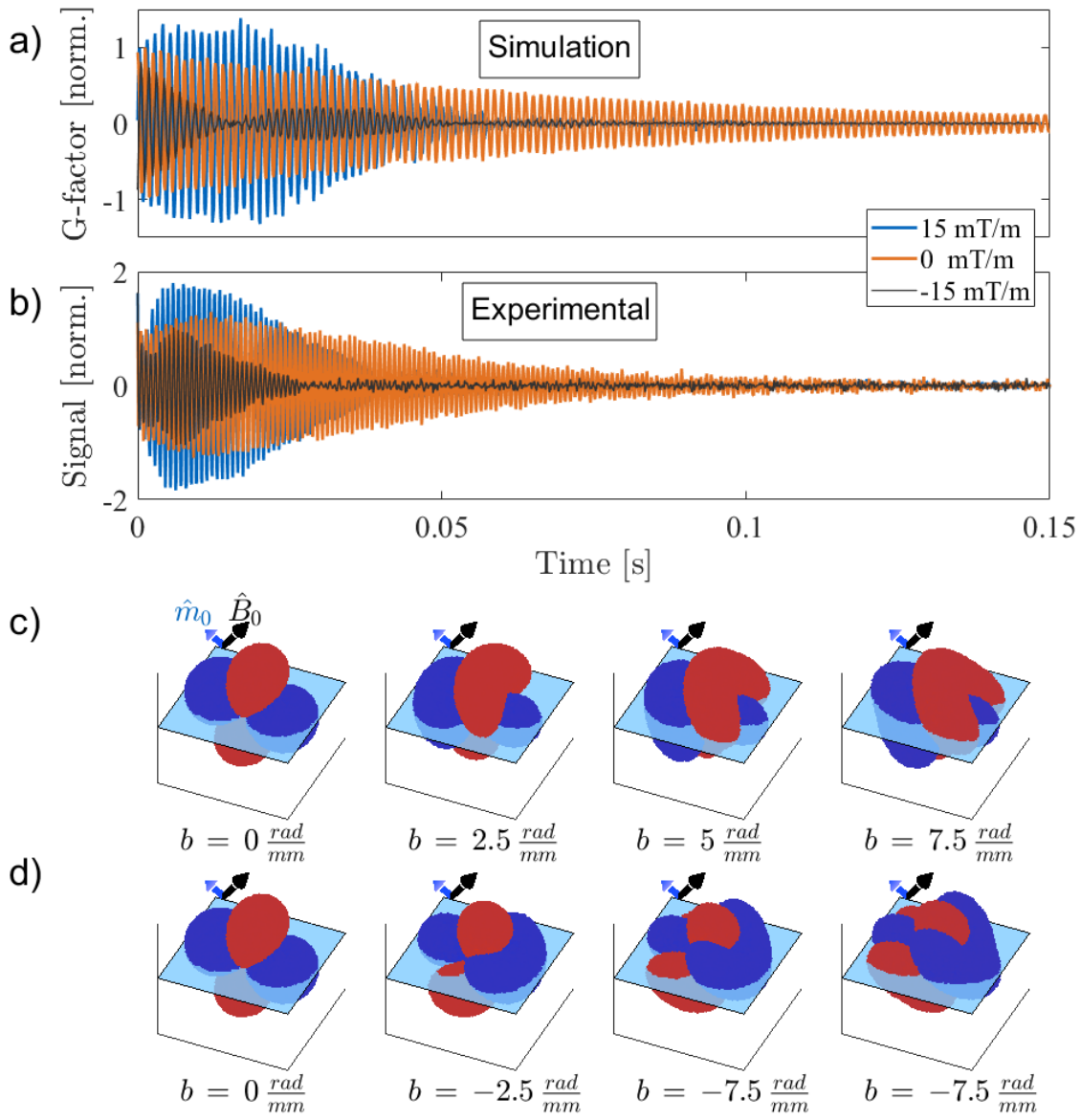

Figure 6.9.: **The dependence of the geometry factor on the gradient direction**
For small dephasings b, the direction of the gradient plays a major role. If the gradient shows in the same direction of the rotation of the "lobes" (**c)**), the rotation is slowed down, since the spins on the "far" end oscillate slower, while the spins on the "near" end speed up. In the case of the opposite gradient direction (**d)**), the effect is reversed and the rotation is sped up. The simulated FNDs of both cases for a constant gradient of 0.015 T/m can be seen in **a)**. Experimental results can be seen in **b)**.

6.3.2. Asymmetric dephasing and the non-exponential envelope of micro-scale NV-NMR

In the presence of a linear B_0-gradient, the sensitivity map of the NV-NMR experiment transforms from a shape similar to a d-orbital into a double helix with more and more windings along the gradient direction $\vec{g}$, seen in Fig. 6.7. Both shapes rotate about the axis of NV-orientation, as seen in Fig. 6.6. For short times, there is a transition period between the two shapes, which can strongly depend on the gradient direction. In Fig. 6.9 a) (b)) the cases of a gradient against (in) the direction of the "orbit-rotation" is seen the far end of sample spins is oscillating slower (faster), while the near end is sped up (slowed down). This leads to a increased (decreased) geometry factor on short time-scales, which can be explained by the effect described in section 6.3.1. In Fig. 6.9 simulation results for three oscillations, with opposing gradients and once without gradient, can be seen. The difference in amplitude is quite drastic. Similar results have been obtained in experimental data, as seen in Fig. 6.9 b).

6.3.3. Flipping the sensitivity map

If the gradient is *against* the direction of the magnetization's rotation above the diamond, hypothetical sample spins below the diamond surface see a gradient *in* the direction of their magnetization's rotation. This is made obvious when applying π-pulses after a short gradient pulse (see Fig. 6.10), since they invert the time evolution of the individual sample spins. Different axis of rotation lead to different sensitivity maps and therefore different amplitudes in the geometry factor. Similar behaviour can be seen in experimental results, with two π-pulses about random axis, see Fig. 6.10 c).

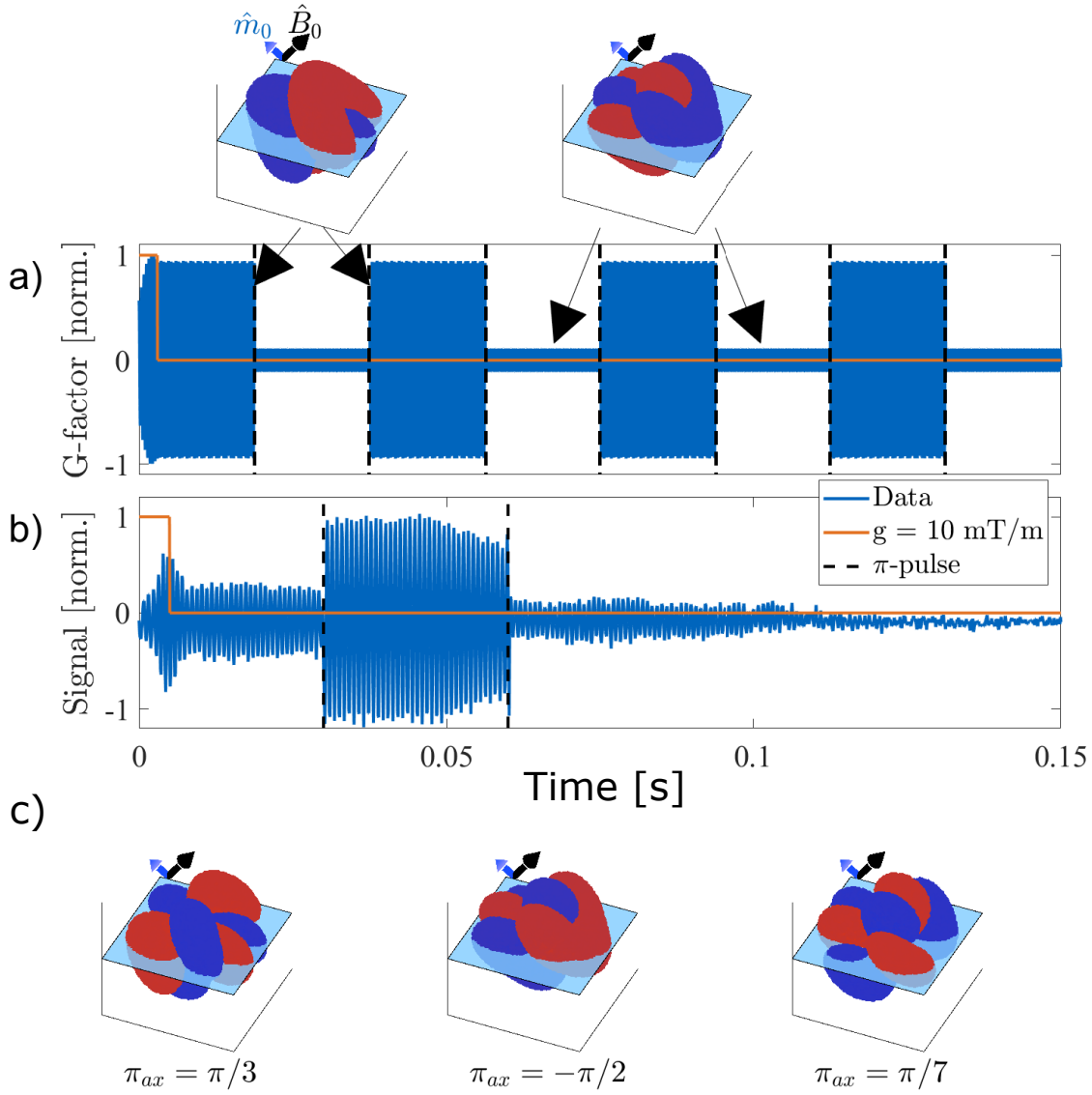

Figure 6.10.: **Flipping the sensitivity map using π-pulses**
a): After a short initial gradient, several π-pulses are applied, each changing the sensitivity map drastically. **b)**: Experimental results of the simulation described in a). **c)** Different π-pulse axes can lead to a different geometry factor.

6.3.4. Gradient-enhanced NV-NMR

This behaviour of NV-NMR can be exploited in several ways. First of the geometry factor for $\langle 100 \rangle$-diamonds using CASR can be enhanced by a factor of ~ 1.4, if the magnetic field is

sufficiently homogeneous and a controlled initial gradient is applied, as seen in Fig. 6.11 a). In addition to signal enhancement, some otherwise impossible experiments can be enabled. As discussed in section 6.1.3 due to symmetry reasons diamonds whose surface are cut along the ⟨111⟩-direction normally can not be used for NV-NMR utilising CASR. Applying a gradient parallel to the diamond-surface breaks the "d-orbital" symmetry and allows for the detection of an NMR signal, see Fig. 6.11 b).

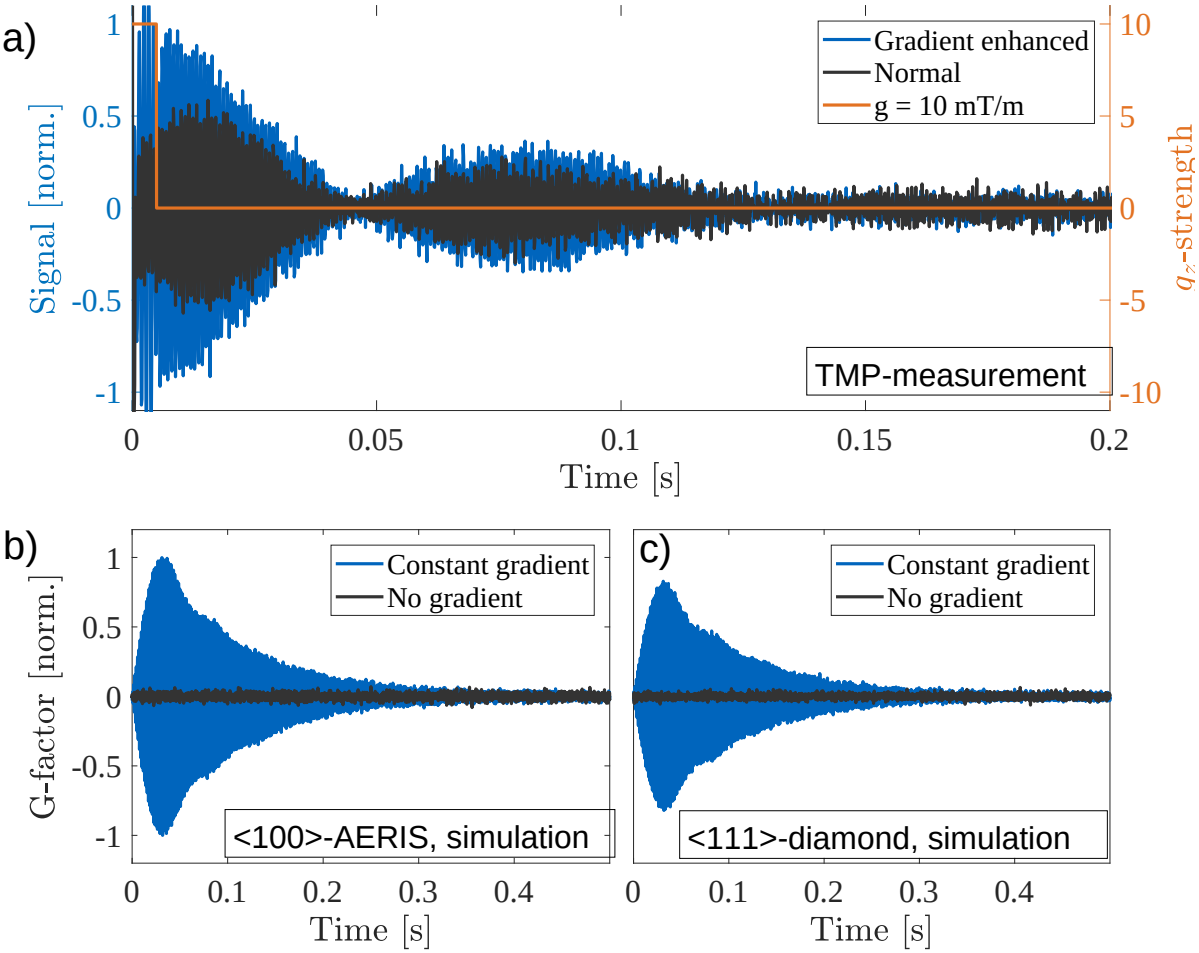

Figure 6.11.: **Enhancing NV-NMR experiments with short gradient pulses**
a): An experimentally measured FND of Trimethylphosphat (TMP) with and without gradient enhanced signal amplitude. **b)**: Simulation of an FND using the AERIS sequence and a ⟨100⟩-diamond, once without gradient and once with gradient. **c)**: Simulation of an FND using the CASR sequence and a ⟨111⟩-diamond, once without gradient and once with gradient.

In total contrast, the AERIS-detection scheme is not applicable to the commonly used $\langle 100 \rangle$-diamonds, see Fig. 6.2. This poses a problem, since $\langle 111 \rangle$-diamonds are hard to obtain and slow to grow.[48,49] Again, applying a gradient orthogonal to the diamond surface has the ability to solve this problem, see Fig. 6.11 d).

Both of these hypotheses have not been tested experimentally.

7. The NV-NMR setup

During my work as a PhD student, my NMR-setup went through many iterations. In this chapter, I will describe the final version of our setup, on which the experiments described in chapter 8 were conducted. In addition to the continuous improvement on the experimental hardware, I developed a software frontend and backend to flexibly switch between the different experiments necessary on a day to day basis, though introducing this software development in detail would go beyond the scope of this thesis. First off, I will introduce the sensitivity of our setup, which is arguably the most important parameter of all.

7.1. Sensitivity and SNR

7.1.1. NV-NMR sensitivity

Sensitivity describes the ability of an NV-NMR experiment to measure a certain quantity, for us magnetic field strength, within a given time and is of the unit $[\frac{\mathrm{T}}{\sqrt{\mathrm{Hz}}}]$. The spin-projection-limited sensitivity of a magnetometer consisting of an ensemble of N non-interacting electronic spins, as our NV-ensemble, is given by:[43,150–152]

$$\eta_{\mathrm{opt}} \approx \frac{\hbar}{\Delta m_s g_e \mu_B} \frac{1}{\sqrt{N\tau}} \,. \tag{7.1}$$

Here $\Delta m_s = 1$ is the difference in spin quantum number, μ_B is the Bohr magneton, g_e is the electronic g-factor and τ is the free precession or interaction time per measurement.

In the case of ODMR-measurements using CPMG-based DD-sequences, the total sensitivity

is given by:[43]

$$\eta_{\mathrm{sp-limit}} \approx \eta_{\mathrm{opt}}\, \eta_{\mathrm{readout}}\, \eta_{\mathrm{overhead}}\, \eta_{\mathrm{decoherence}} \,. \tag{7.2}$$

η_{opt} has been described above, η_{readout} is a term depending on from the imperfect readout fidelity:[43,153,154]

$$\eta_{\mathrm{readout}} = \sqrt{1 + \frac{1}{C^2 n_{avg}}} \,, \tag{7.3}$$

where the readout contrast $C = \frac{a-b}{a+b}$ and $n_{avg} = (a+b)/2$, a and b denoting the average number of photons detected from the $|0\rangle$ and $|1\rangle$ state respectively.

η_{overhead} is a term, that originates from the readout overhead, initializing the NV-ensemble and reading out the quantum state takes a significant amount of time, in which there is no interaction between the spins and the sample. It can be written as:[43]

$$\eta_{\mathrm{overhead}} = \sqrt{\frac{t_I + \tau + t_R}{\tau}} \,, \tag{7.4}$$

where t_I and t_R denote the initialization and readout time, respectively.

Lastly $\eta_{\mathrm{decoherence}}$ describes the amount of decoherence in the qubit state while measuring with a pulse train of k pulses and is modeled by:[43]

$$\eta_{\mathrm{decoherence}} = 1/\exp(-[\tau/(k^S T_2)]^p) \,, \tag{7.5}$$

where p is a stretched-exponential parameter, which stems from the ensemble-averaging over many different decoherence-times and s depends on the noise spectrum in the NV-spin bath. In most cases the sensitivity is not limited by the spin projection, but rather by the photon shot-noise of the measurement setup. A detailed derivation of this can be found in Barry et al.:[43]

$$\eta_{shot} \approx \left(\gamma_{electron}\, C\, \exp(-(\tau/T_2^*)^p)\, \sqrt{N\, n_{avg}\, \tau}\right)^{-1} \,. \tag{7.6}$$

Increasing the sensitivity is of vital importance to measure NMR-signals of smaller size than the signal of highly concentrated water.[48] Looking at equations 7.1-7.6, the two parameters,

which can be controlled the best are 1) The difference in number of photons detected per readout $C^2 n_{avg}$, for example through more efficient light collection or higher NV-concentration. 2) The NV-ensembles decoherence time T_2 , which in turn effects the interaction time τ between the NV-centres and the sample spins. This can be done through better diamond-engineering.

7.1.2. Signal to noise ratio and averaging time

The signal to noise ratio (SNR) of an NMR-experiment is determined by the ratio between the signals peak amplitude A_{peak} and the standard deviation of the complex noise spectrum,

$$\mathrm{SNR} = A_{peak}/\sigma_{noise} \, . \tag{7.7}$$

To reach SNR_{target} using a setup with sensitivity η, a signal of strength B_{signal} has to be averaged over a time $t_{avg} = (\eta / B_{signal}\,\mathrm{SNR}_{target})^2$. Typical sensitivities quoted for micro-scale NV-NMR experiments are of the order of $\eta_{\mathrm{CPMG-like}} \approx 20\,\mathrm{pT}/\sqrt{\mathrm{Hz}}$. How the experiment is calibrated is discussed in appendix section B. As discussed in chapter 6, the maximum amplitude of an expected NMR-signal is on the order of $S \approx\sim 200$ pT. The narrowest full width half maxima (FWHM) of NV-NMR spectral lines quoted in literature[44,87,97,136] and the ones in our setup (e.g. Fig. 6.11) are of the order of $\sim 1-5$ Hz Using 5 Hz, $T^*_{2,proton} = 1/(\pi\, FWHM) \approx 0.0637$ s leading to an average signal amplitude of 42 pT over the first 0.2 s. For a target SNR of 10, this leads to an averaging time of:

$$t_{average} \approx (\eta / B_{avg,signal}\,\mathrm{SNR}_{target})^2 = 22\,\mathrm{s} \, , \tag{7.8}$$

so a total of $t_{average}/0.2\,s \approx 113$ averages are needed.

It should also be mentioned, that the repetition rate of the NMR-experiments is limited by the sample spins relaxation time (T_1), since the sample should be in thermal equilibrium at the beginning of each measurement. For a sample of pure water the relaxation time of the

hydrogen's nuclear spin is on the order of ∼3 s,[19] though the TEMPO solution added to the sample for Overhauser DNP has the beneficial side effect of lowering the sample-T_1 time to ≈0.3 s.[19]

7.2. Optics

A major part of each NV-centre setup are its optics. Not only does the laser used for NV-centre initialization and readout need to be controlled, there is also the question of how to collect the NV-fluorescence in the most efficient way.

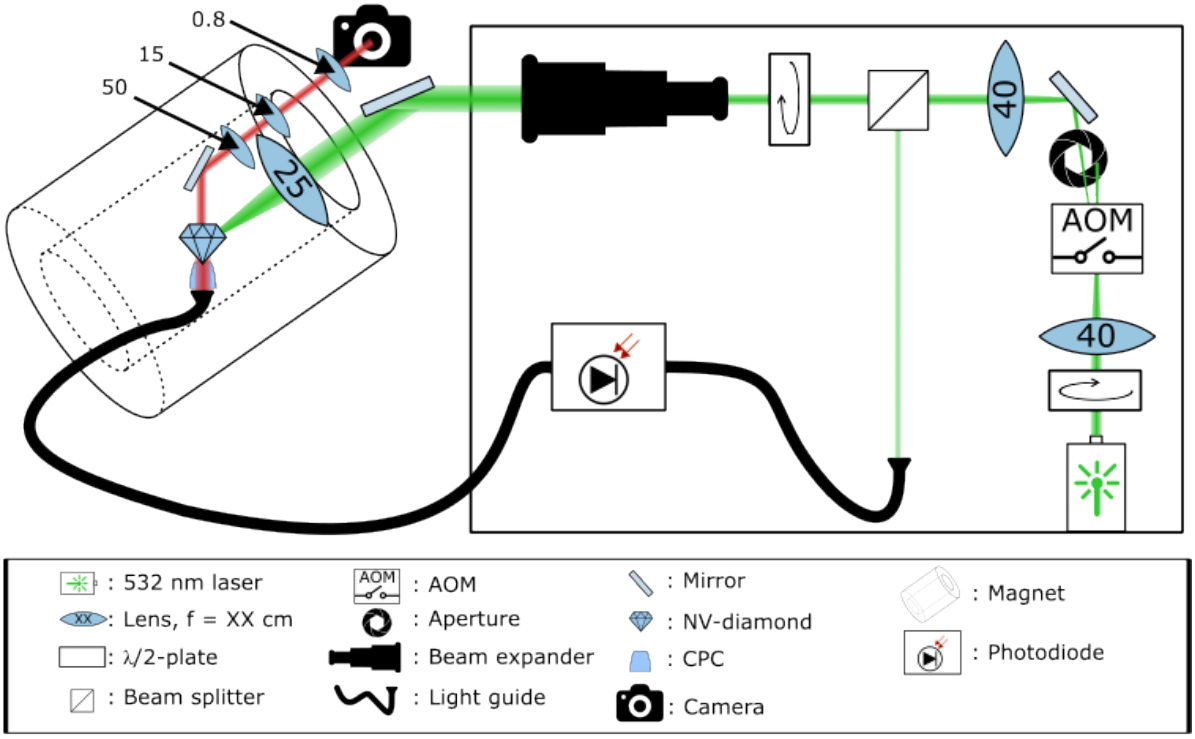

Figure 7.1.: **The optical equipment in our experiment**
A sketch of the optical equipment used for the experiments in this thesis. A detailed description of the equipment shown in this figure can be found in section 7.2.1.

7.2.1. AOM and optics

The optical equipment used in our experimental setup is sketched in Fig. 7.1. The laser used in our setup (Laser Quantum Opus 53) has a wavelength of 532 nm. Typical laser powers for readout and initialization are 380 mW, repolarizing the NV-centre spins within $\sim 5\,\mu$s. We would achieve better sensitivities at high laser power, both due to a higher photon count as well as a shorter repolarization, the limiting factor is the fact, that the maximum output power is shared between different experiments. After the laser, the beam passes a $\lambda/2$-plate (ThorLabs), which rotates the laser's polarization, to match the acousto optic modulator (AOM) used shortly after. Between the AOM (Gooch and Housego, model 3260-220) and the $\lambda/2$-plate, there is one f = 400 mm lens (ThorLabs), focusing the beam onto the AOM.

The AOM itself is used for defining the laser pulses and is controlled by our arbitrary waveform generator (AWG), discussed in section 7.4.1. It contains a piezoelectric crystal, on which acoustic waves can be created using an applied AC-current at 250 MHz. The laser beam diffracts on this wave-pattern leading to several diffraction maxima. If the laser beam and its polarization are aligned correctly, up to 71 % of the incoming beam's intensity can be reached in one of the first maxima.[155] As sketched in Fig. 7.1, the 0^{th} maximum is stopped via an aperture, on which one of the first maxima is centred. Using AC-pulses the AOM can be used to create laser pulses in the order of $> 0.1\,\mu s$.[155] From the AWG's controlling signal to the AOM-response, there is a delay of ~ 600 ns.

400 mm after the AOM there is an identical lens as the first, collimating the laser beam. A non-polarizing beam-splitter cube (ThorLabs) splits the laser beam into two, with intensities of 90% and 10% respectively. The lower intensity beam is reduced further using a reflective filter (ThorLabs), until it is of the same intensity as the collected NV-fluorescence. Then it enters a liquid light guide (Lumatec) which is connected with our photo diode (PD, PDB210A, ThorLabs). This is for real-time laser-noise cancellation, since our PD has two direct input channels, and one reference channel, who's output is the difference of the two input channels.

The higher intensity beam is led through an optical beam expander (ThorLabs BE02-05-A),

increasing the width of our Gaussian laser beam. This helps focusing the laser onto a smaller laser-spot, since the minimum laser diameter after a focusing lens is inverse proportional to the initial diameter. Finally the beam enters the magnet and is focused onto the diamond using a f = 250 mm lens (ThorLabs).

7.2.2. Light collection

The laser is coupled into our trapezoid diamond via a total internal reflection geometry, seen in Fig. 7.2 a). In our current setup, the fluorescence light leaving the diamond is collected using a compound parabolic concentrator (CPC) designed by us and fabricated by Süd-Optik Schirmer GmbH, which increases the numerical aperture of our system by collimating the light from originating from our laser spot.

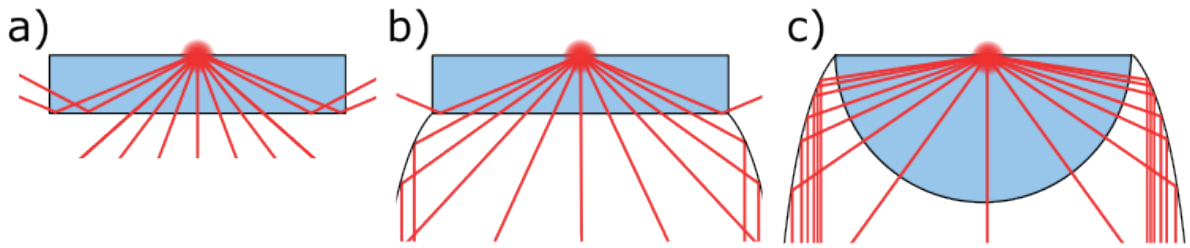

Figure 7.2.: **Sketches of different light collection setups**
The diamond is shown in blue, with a red fluorescence spot in the middle. Red lines indicate light-rays from the point source. **a)**: The fluorescence light escaping a cuboid diamond. The yield of the fluorescence light collection is rather low, since much is escaping the diamonds side, due to its high refractive index. **b)**: A CPC is glued directly under the diamond, the numerical aperture of the system is greatly increased. **c)**: A hemispherical diamond is used in conjunction with a hollow CPC. Nearly all of the fluorescence light is collected.

There are more optimal solution for light collection, for example the hemispherical NV-diamond in Fig. 7.2 c), but we opted for the CPC due to its ease of use.
The fluorescence light is collected by a liquid light guide, after which it is collimated again using a condenser lens (ThorLabs). The remaining 532 nm laser light is filtered out using an optical filter (Semrock) and it is finally focused onto one of the inputs of our PD.

7.3. The magnet and the sample holder

Optics equipment can readily be bought, but most of the parts used surrounding our diamond needed to be a custom design, due to some unusual constrains in the NV-NMR setup. The most significant one being the necessity to align the magnets magnetic field with the NV-axis, which leads to a $\sim 35.26^\circ$ angle of the magnet and the floor of our laboratory. In this section I will discuss the custom parts used in our setup.

7.3.1. The superconducting magnet

The superconducting magnet (Superconducting Systems INC., 3T-215-RT) is designed for rodent MRI and has a bore size of 22 cm diameter. It is mounted on a custom stage, capable of rotating in all directions for the alignment of the magnetic field. Since we are using $\langle 100 \rangle$-diamonds in all our experiments, the magnet needs to be mounted at an angle of about 35.26° with respect to the floor, as seen in Fig. 7.3 a). This is to ensure, that the magnetic field is aligned with the NV-centre's crystal orientation. It can produce magnetic fields up to 3 T, though all experiments in this thesis were conducted at ~ 0.175 T. The sample holder containing the diamond is mounted at the end of an aluminium rod, which is lowered into the centre of the magnet's bore. The laser is guided along this rod and through the lens focusing the laser onto the diamond, as seen in Fig. 7.3 b). Lastly the camera and the lenses acting as a microscope and imaging the diamond onto the camera are mounted on top of the aluminium rod.

7.3.2. The sample holder

The sample holder is a custom design and 3D-printed using a Formalabs 3 and Formlabs grey resin. The design can be seen in Fig. 7.4, the microfluidic chip containing the sample as well as the diamond is placed in the middle of the holder. Below it the CPC guides the NV-fluorescence into the liquid light guide, which is stuck into the bottom of the holder.

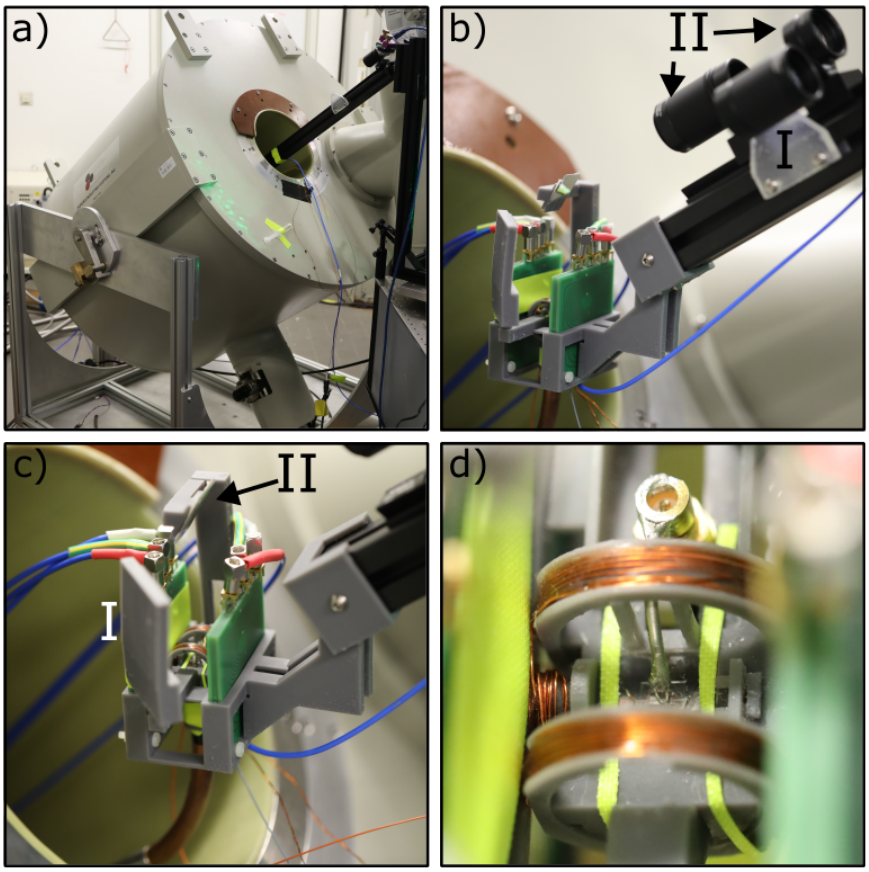

Figure 7.3.: **Photos of the magnet and sample-holder**
a): An image of the tilted superconducting magnet used in our experiments. A aluminium rod holding our sample-holder is entering the middle of the boar. **b)**: The top of the aluminium rod. In the top right corner one lens focusing the laser onto the diamond (I) and two lenses focusing an image of the diamond onto our camera (II) are seen. In the bottom left is our sample holder. **c)**: A close up of our sample holder. The gradient-PCBs are clearly visible, as well as a mirror used for redirecting the laser onto our diamond (I) and one mirroring the image of our diamond onto the camera (II). **c)**: A close up of the sample holder's centre. The Helmholtz-pair used for driving the proton spins as well as the calibration-coil are visible. The microfluidic chip is held tight by the MW-antenna and two strings of tape.

Next to the microfluidic chip, there are two coils forming a Helmholtz-pair, which is used for driving the sample spins with a homogeneous field. A third, smaller coil is placed orthogonal to the Helmholtz-pair, which is used for calibrating the measurement setup as described in appendix section B. The gradient coils are on the printed circuit boards (PCB)

next to the Helmholtz-pair.

The laser is coupled into the diamond through one of the Helmholtz-coils using a mirror. The loop used for the NV-centre control is fixed using a bulkhead SMP-connector and is in direct contact with the microfluidic chip, asserting some pressure and keeping it in place. Finally the mirror used for monitoring the experiment is directly above the diamond.

7.3.3. The diamond

The diamond sensors used for experiments in this thesis are of type IIa, based on electronic grade single crystal diamonds (2.0 x 2.0 x 0.5 mm^3) with a bulk nitrogen concentration of < 5 ppb (Element Six Technologies Limited). The bulk diamonds were overgrown homoepitaxially by CVD, with nitrogen-doped diamond layers (Fraunhofer Institute for Applied Solid State Physics). The doped layers are estimated to contain 5 ppm nitrogen impurities and were subsequently irradiated with electrons at a flux of $\sim 5 * 10^{17} cm^{-2}$ (US Diamond Technologies). Finally, they were high-temperature annealed in a custom oven at 1000° C for 2 h under vacuum conditions, resulting in a dense NV ensemble layer. Next, the diamonds were cut so that the top face containing the NV ensemble is in the $\langle 100 \rangle$ crystal orientation and two sides of the diamonds were polished at a 45° angle resulting in a trapezoidal-shaped diamond where the top face is 2.0 x 1.0 mm in size (MEDIDIA GmbH). The trapezoidal shape allows us to enter the diamond in a total internal reflection geometry, see Fig. 7.4, resulting in a higher laser power at the diamond surface, while reducing laser power within the sample itself, mitigating laser induced sample heating.

7.3.4. The microfluidic chips

Two different designs of microfluidic chips were used, though the basic working principle and fabrication is the same,[138] they can be seen in Fig. 7.5. The microfluidic chips are produced from fused silica by selective laser-induced etching (SLE). SLE uses ultra fast, high energy laser pulses focused on voxels of 3D space. These pulses damage the structure of the

fused silica enough, that subsequent wet-etching is able to selectively remove the damaged structures, resulting in highly resolved 3D structures.[156]

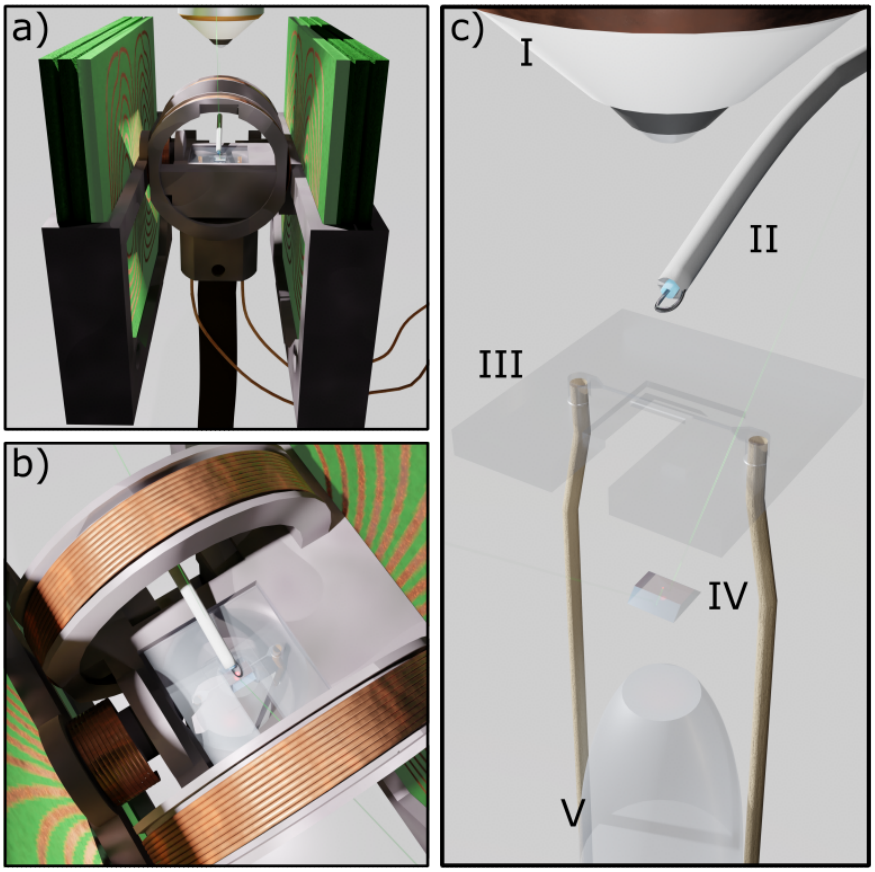

Figure 7.4.: **Renders of our sample-holder**
a): The pairs of gradient coils can be seen as the green PCBs left and right of the chip in the middle. Microfluidic-tubing and the light guide leave the sample holder from the bottom. A microscope objective at the top stands in for the optics in place for imaging our experiments from the top. **b)**: A closer up render of the central part. Two big coils forming a Helmholtz-pair are used for sample-spin control. A third, smaller coil is used for calibration of the experiment.The microfluidic chip, containing the diamond sits in the middle and is held in place by the microwave antenna. **c)**: An explosion render to visualize the most important components. From top to bottom: A camera objective (I), standing in for the optical access from the top, used for microscopy. The microwave-antenna (II) for NV-control. The microfluidic chip (III) in which the diamond (IV) is glued, the laser enters and exits the diamond in a total internal reflection geometry. Finally the CPC (V) for fluorescence collection.

The microfluidic chips were designed in house and manufactured by LightFab GmbH. The diamond trapezoids were glued into the microfluidic chips using UV-curing optical adhesive (NOA68, Norland Products). The sample is delivered through two PEEK tubes, also glued into the microfluidic chip (SGEA1301005001-5F, VWR). To cure the glue optimally, the chip was placed over night at 50° C under UV illumination (Form Cure, Formlabs Inc.). Detailed pictures of the microfluidic setup can be seen in Fig. 7.4 and Allert et al.[138]

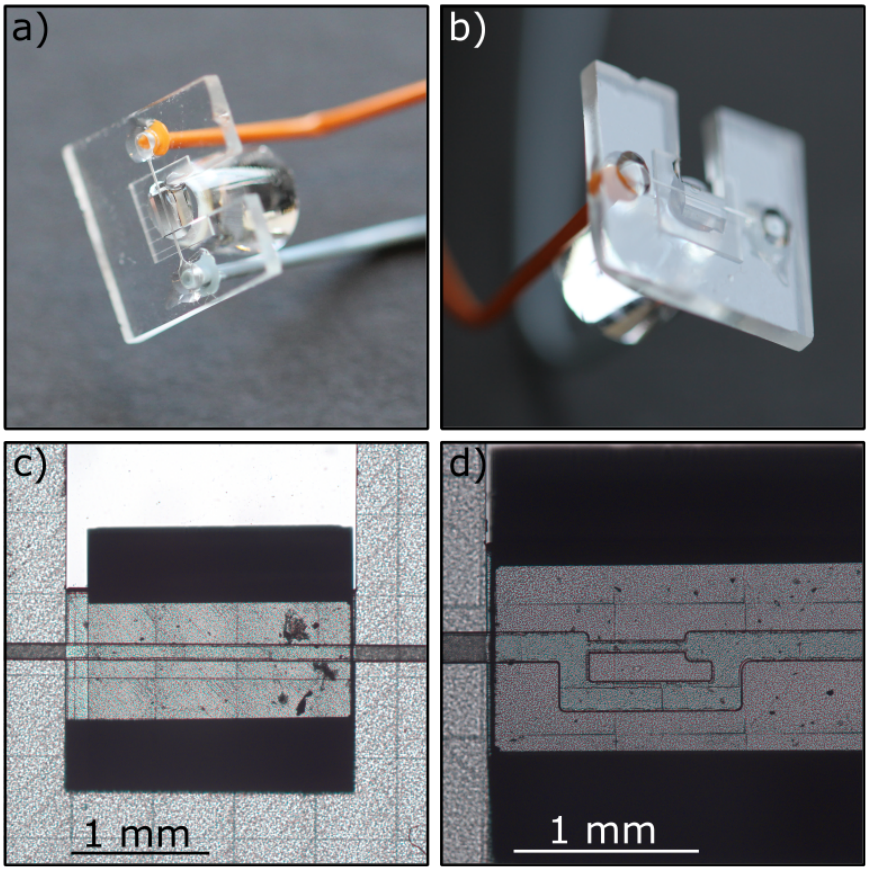

Figure 7.5.: **Photos of our microfluidic chip**
a), **b)**: Two photos of the microfluidic chip used most commonly. The diamond and the CPC are glued into the chip as well as the microfluidic tubing. **c)**, **d)**: Two photos of the standard microfluidic chip and the one used under the anisotropy experiments discussed in chapter 8 respectively. These photos were taken under the microscope without glue.

7.4. NV-microwave control

The microwave control of our setup contains some of the most expensive and most powerful machines in our setup, necessary for the precise manipulation of the NV-centres' spins. In this section I explain in detail, which device is connected to which and in what way. A detailed schematic of connections is seen in Fig. 7.7.

7.4.1. The arbitrary waveform generator

The heart of the experiment is the arbitrary waveform generator (AWG), precisely timing and synchronising microwave control of both the NV-centres themselves as well as the sample spins. In the setup described here, we use a AWG700002B by Tektronix. It has a maximum sampling rate of 25 GSa/s and two channels with one analogue output, two marker outputs and four flags outputs. Analogue outputs have a resolution of 8 bits between 0 and 0.75 V_{pp} and are used to define the individual microwave pulses as well as their relative phase. Usually these pulses are synthesised at a frequency between 100-1000 MHz. Marker outputs have the same resolution as the analogue outputs (maximal 25 GSa/s), but they are can only be set to 0 or 1.25 V. We use these as high-resolution transistor-transistor-logic (TTL) signals, controlling various devices in our experimental setup. Finally the flag outputs are also used as TTL signals, though their resolution is much smaller than that of the marker outputs. It is either on or off for each waveform uploaded to the AWG.

Each of our different experiments is uploaded to the AWG as two "sequences", containing multiple "wave-forms". Here wave-forms describe an array of X samples, each sample containing an amplitude value for the analogue output and a value for each of the marker channels. Wave-forms can be of arbitrary length, but at least 2400 samples. Sequence means a series of wave-forms w_i, each of which is repeated n_i times. Each wave-form, stored in the sequence, also has an output-amplitude set for each of the flag outputs, as well as parameters concerning which waveform to play next, either via a trigger command or after the n_i repetitions. Using this architecture, arbitrarily complex experiments can be programmed

into the AWG. A sketch of this can be seen in Fig. 7.6. In our experiment the two analogue outputs are connected to the IQ-mixer (see section 7.4.3) and the four highly resolved marker channels are used to gate the AOM, the signal source controlling the gradient pulses for the diffusion experiments (RIGOL LXI DG1022), the RF-drive controlling our sample spins (RIGOL LXI DG1022) as well as the data acquisition unit (DAQ, NI USB-6821), which needs to be timed to be synchronous with the AOM/laser pulse. The flag channels are used for gating the RF-signal used for calibration (RIGOL LXI DG1022), as an additional gate for the sample spin RF-drive and as a trigger for quickly switching the frequency of our NV-drive (R&S SMB100A).

a)

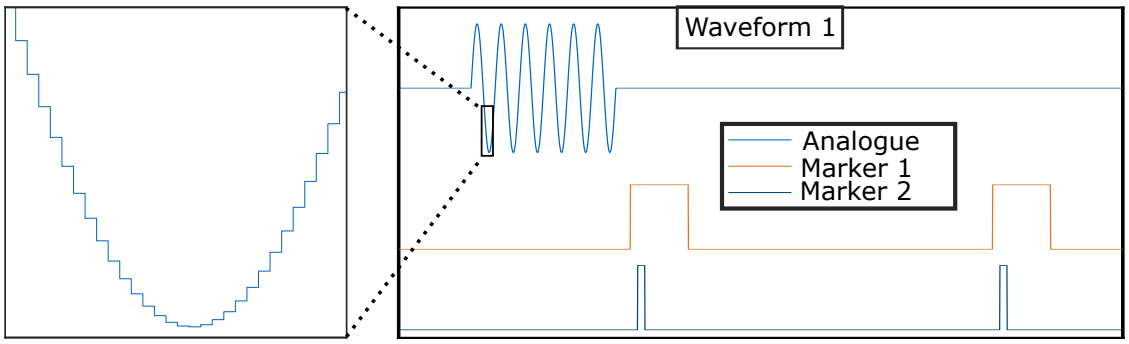

b)

Waveform name	Repetitions	Go to	Jump to	Flag channels			
Waveform 1	200	2	1	A: off	B: off	C: off	D: off
⋮				⋮			
Waveform N-1	∞	N	1	A: off	B: on	C: off	D: on
Waveform N	50	1	1	A: off	B: off	C: off	D: on

Figure 7.6.: **An experimental sequence on the AWG**
a): An examplary waveform uploaded to one of the AWG's channels. The analogue signal is displayed in blue, the marker channels are displayed in orange and dark blue. Inset: A zoom-in into the analogue waveform, the signal is uploaded in discrete samples. **b)**: An example of a sequence. Several waveforms are chained, and each is assigned additional parameters: The number of repetitions, the next waveform to play (Go to), which waveform to jump to on a trigger event (Jump to) and which flag outputs to turn on during the sequence step.

7.4.2. Signal source

The signal source used for driving the NV-centre spins is a Rhode & Schwarz SMB100A. It is capable of producing monochromatic frequencies between 100 kHz and 40 GHz. Since we use Overhauser DNP for increasing our signal strength, we need to quickly ($\sim$ ms) switch between the Overhauser driving frequency $f_{Overh} = \gamma * B_0$ and the NV-resonance frequency $f_{NV,\pm1} = \gamma * B_0 \pm D_{ZFS}$. This is feasible by triggering the SMB100A using one of the AWG's TTL signals.

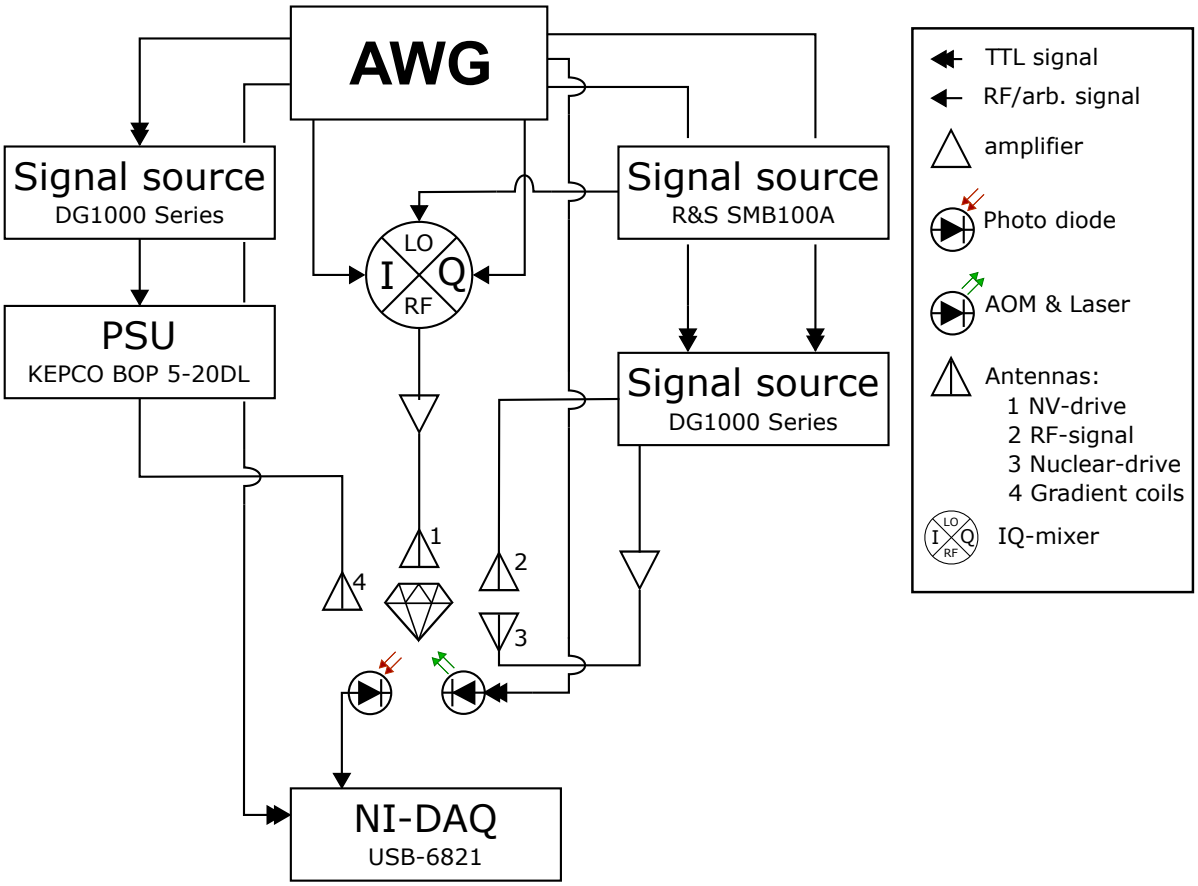

Figure 7.7.: **The microwave setup**
A detailed schematic of our microwave setup, described in this section.

7.4.3. IQ-mixing

We use an In-phase/Quadrature (IQ)-mixer for up-converting our AWG's microwave signal to the desired frequency. While this is not strictly necessary for lower magnetic fields, due to the high sampling rate of our AWG being capable of directly synthesizing frequencies up to ∼10 GHz, mixing still increases the output amplitude of our AWG at low fields.
The working principle of IQ-mixers is briefly described in appendix section I, for this section it is sufficient to state, that the three input signals I, Q (both AWG analogue outputs) and LO (R & S output) are mixed in such a way, that the resulting RF waveform has the shape:

$$\begin{aligned} RF =& \frac{1}{4} A_I \left(\cos((\omega_{LO} + \omega_{AWG})t + \phi_I) + \cos((\omega_{LO} - \omega_{AWG})t - \phi_I)\right) \\ &+ \frac{1}{4} A_Q \left(\cos((\omega_{LO} + \omega_{AWG})t + \phi_Q) + \cos((\omega_{LO} - \omega_{AWG})t - \phi_Q)\right) \ , \end{aligned} \tag{7.9}$$

where A_I, A_Q and ϕ_I and ϕ_Q are the I and Q channels amplitudes and phases respectively. Also assuming both I and Q channels have the same frequency ω_{AWG}. In the frequency domain, this corresponds to two peaks at distance $2\,\omega_{AWG}$ centred around ω_{LO}.
Choosing $A_I = A_Q$ and $\phi_I = 0$, $\phi_Q = \frac{\pi}{2}$, the above equation simplifies to:

$$RF = \frac{1}{2} \cos((\omega_{LO} + \omega_{AWG})t) \ . \tag{7.10}$$

Removing the peak at $\omega_{LO} - \omega_{AWG}$, effectively up-converting our AWG-waveform to a much higher frequency than possible to synthesize with the AWG's resolution.

7.5. Sample spin control

Since we are detecting thermally polarized NMR-signals, our setup needs the necessary equipment to coherently control the sample spins/protons. In this section I will talk about the relevant microwave equipment and future challenges.

7.5.1. The sending-coil

Since the detection of the NMR-signal is via our NV-diamond, we only need a sending coil to control the sample-protons. This is done via a pair of Helmholtz-coils with radius $R = 1.5$ cm. They have ten windings each and are connected to an RF amplifier (Mini-Circuit, LZY-22+). The RF signal is generated by a RIGOL LXI DG1022, which is gated by one of the AWG's flag outputs. In addition, between the Rigol and the amplifier there is a RF-switch (Mini-Circuit, RIGOL LXI DG1022) which is needed to preserve the initial phase of multi-RF-pulse sequences.

7.5.2. π-pulses and problems with spin control

As described above, the Helmholtz-pair used as an RF-drive is not resonant at the driving frequency of the proton spins. Previously used resonant coils had problems with drifting resonance-frequencies and were unreliable for executing precise pulses. At the moment, the fastest π-pulses achieved in our setup were around $\sim$40-80 μs which is an order of magnitude slower than usual π-pulses in conventional NMR. Especially for novel sequences, like the AERIS sequence, stronger RF-drives are necessary and either a stable, resonant circuit or a stronger RF-amplifier needs to be added to the current setup. An example of a Rabi-experiment on our sample spins and a FND in our setup can be seen in Fig. 7.8.

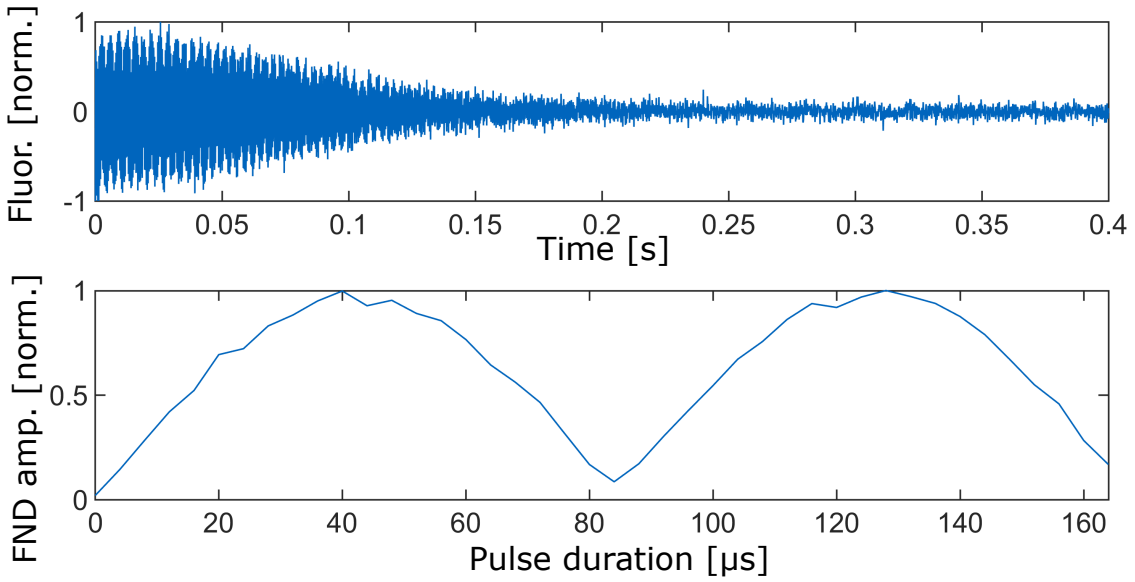

Figure 7.8.: **FND and proton-Rabi**
a): An example of a free nuclear decay in our experiment. **b)**: An example of a proton Rabi experiment in our setup.

7.5.3. Gradient coils

For the PGSE-experiments described in chapter 8, gradient coils were designed in a collaboration with the University Medical Center Freiburg. The coils were printed on printed circuit boards (PCB) and mounted on the sample holder, as seen in Fig. 7.4. Designing these coils was not straight forward for two main reasons:

1. The magnetic field is at an angle towards the PCB, necessitating unusual coil geometries.

2. Optical access was necessary for the laser beam, the fluorescence readout as well as the monitoring camera.

A more detailed description of the design process can be found in.[157,158] The resulting coils produced linear B_0 gradients of $g_x \approx 30\frac{\mathrm{mT}}{\mathrm{Am}}$, $g_y \approx 31\frac{\mathrm{mT}}{\mathrm{Am}}$ and $g_z \approx 28\frac{\mathrm{mT}}{\mathrm{Am}}$.
The coils were connected in series with the output of a bipolar power supply (KEPCO BOP 5-20DL), which in turn was gated by a RIGOL LXI DG1022 outputting the desired control voltage. The Rigol itself was gated by one of the AWG's marker outputs. A measurement of

the different gradients produced at a current of 1 A can be seen in Fig. 7.9. The measurements were conducted using a wide field approach, measuring the Zeeman splitting of the electronic $|\pm 1\rangle$ states using ESR. From this the relative magnetic fields can be calculated, using the electrons gyromagnetic ratio.

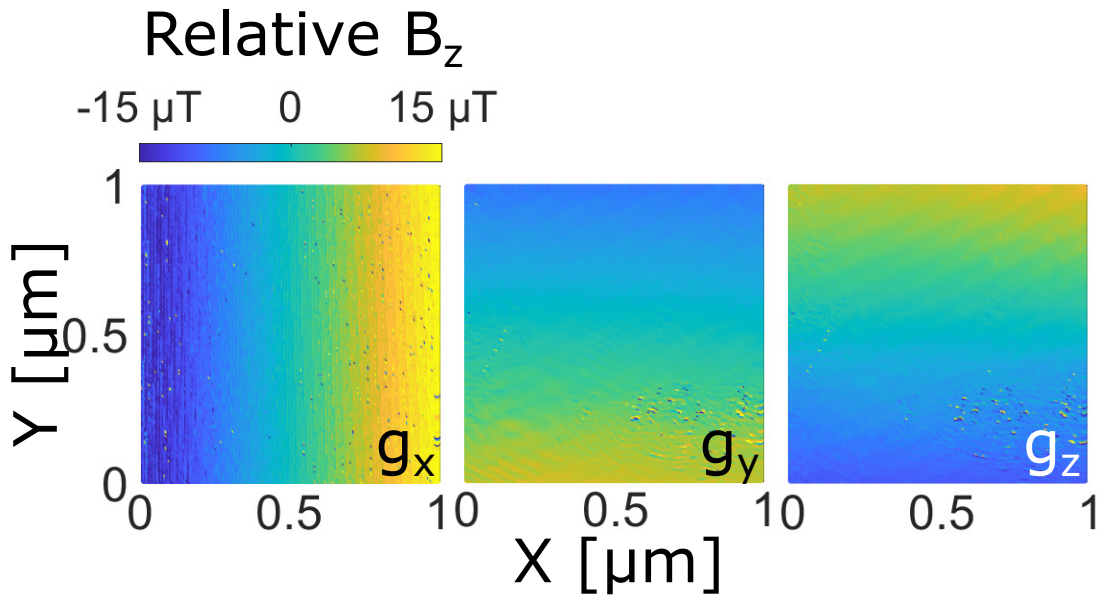

Figure 7.9.: **The gradients produced by our gradient coils on the NV-diamond surface** The measured gradients produced by the gradient coils in the diamond surface-plane. Only $g_x = 0.030\,\frac{\mathrm{T}}{\mathrm{m}}$ lies within the diamond surface-plane, so the gradients fitted along the $g_y = 0.032\,\frac{\mathrm{T}}{\mathrm{m}}$ and $g_z = 0.028\,\frac{T}{m}$ were measured and corrected with $\frac{1}{\sin(35.26°)}$ and $\frac{1}{\cos(35.26°)}$, respectively.

8. Pulsed field gradient NV-NMR

The effects of gradients on NMR experiments have been thought about since the very beginning.[8] The first pulsed gradient experiments in the 1960s proved to be of the utmost value,[92,159–162] paving the way for modern technologies like the MRI-scanner. In this section I will discuss the basics of diffusion-NMR and explain in detail the experiments conducted by me.

8.1. The diffusion tensor

The free diffusion coefficient D of a medium is defined as:

$$\mathrm{D} = \frac{\langle x^2 \rangle}{2N\,t}\,, \tag{8.1}$$

where $\langle x^2 \rangle$ is the mean squared distance a particle within this medium moves within the time t and N is the number of dimensions, the particle is diffusing in. If the diffusion is unrestricted, the diffusion coefficient is constant for all t. For pure water at about 25° C, the diffusion constant has be measured to be $D_{lit,0\%} \approx 2.3 \times 10^{-9}\,\mathrm{m}^2/\mathrm{s}$.[163–165] In the case of restricted diffusion, e.g. due to the walls of our microfluidic channel hindering the random motion of the water molecules, the system is described by the apparent diffusion coefficient (ADC). The ADC is strictly smaller than D and depends on the time of free diffusion as well as the restriction of the sample volume in each direction.[92]

For a free diffusion constant D_0, the mean squared distance travelled per molecule is on the order of $\sqrt{D_0 t}$. Following Kusumi et al.,[166] the ADC in one dimension, e.g. between two

parallel plates, can be calculated to be:

$$ADC\,(t) = \frac{\langle (x_0 - x(t))^2 \rangle}{2t} = \frac{L^2}{6} - 16\frac{L^2}{\pi^4}\sum_{n=1}^{\infty}\frac{1}{(2n-1)^4}\,\exp(-\left(\pi\frac{2n-1}{L}\right)^2 D_0 t)\,, \qquad (8.2)$$

where L is the maximum distance a particle can diffuse, e.g. the distance between the two plates, and $\langle (x_0 - x(t))^2 \rangle$ is the mean squared particle displacement. Modeling the microfluidic channel as a cuboid, the ADCs in each of the three cardinal directions, between pairs of opposing walls, can be calculated, see Fig. 8.1.

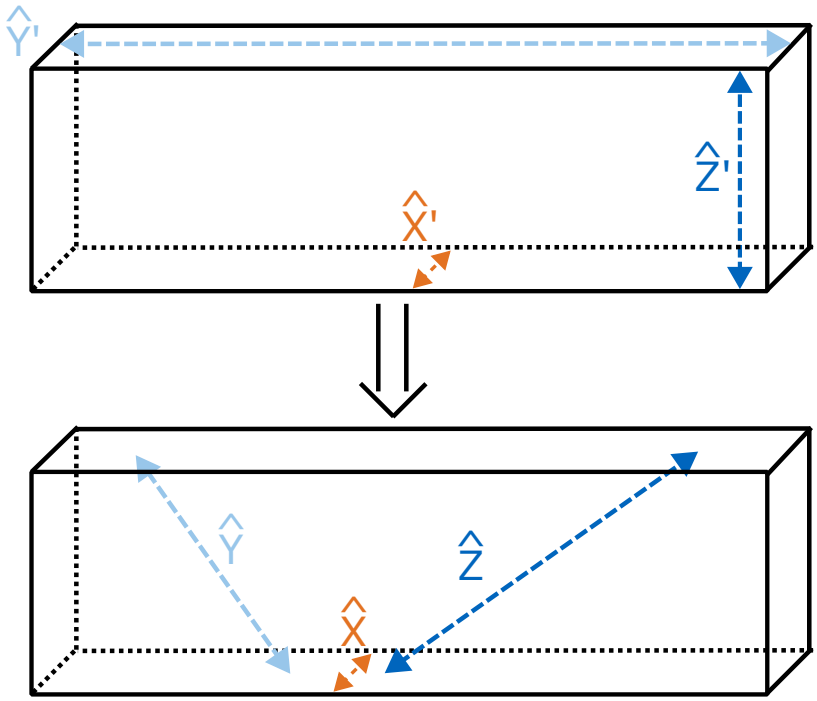

Figure 8.1.: **Coordinate transformation**
Top: The Cartesian basis in which the diffusion tensor of a cuboid is diagonal. **Bottom**: The basis used throughout this thesis, in which $\hat{z}||\hat{B}_0$ and in which our gradient PCBs produce their gradients.

In this case each of the values $ADC_{x'}$, $ADC_{y'}$ and $ADC_{z'}$ are the eigenvalues of the diffusion tensor and the tensor is diagonal in this basis. The gradients used in our experiment are in a different basis, in which $B_0||\hat{z}$, which is equivalent to a rotation of our coordinate system

around $\hat{x}$ by $\phi \approx 35.26°$, with $\hat{x} = \hat{x}'$, $\hat{y} \to \hat{y}'$ and $\hat{z} \to \hat{z}'$. Calculating the ADC in this basis leads to:

$$\begin{aligned} ADC_{\hat{x}}(t) &= ADC_{\hat{x}'}(t) \\ ADC_{\hat{y}}(t) &= \cos^2(\phi) ADC_{\hat{y}'}(t) + \sin^2(\phi) ADC_{\hat{z}'}(t) \\ ADC_{\hat{z}}(t) &= \sin^2(\phi) ADC_{\hat{y}'}(t) + \cos^2(\phi) ADC_{\hat{z}'}(t) \ . \end{aligned} \tag{8.3}$$

This analytical result can be compared with a numerical simulation, where the mean squared distance traveled of each sample volume is calculated as described in chapter 6. As seen in Fig. 8.2, both numerical simulations and theory agree very well.

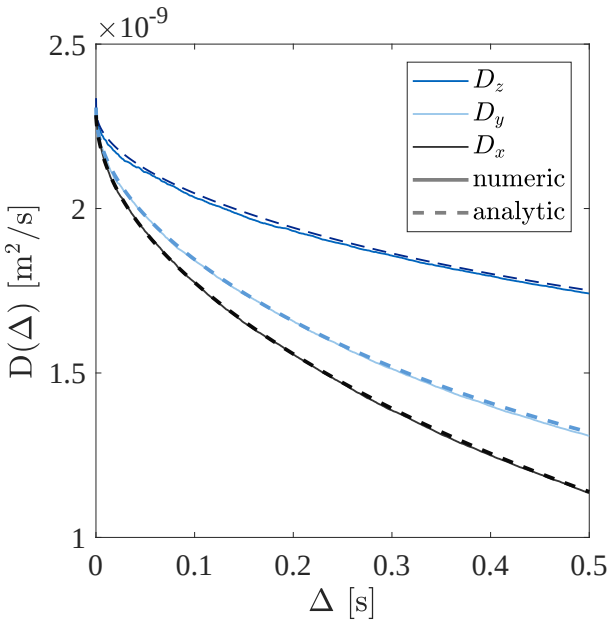

Figure 8.2.: **The ADC as a function of the diffusion time**
The diagonal values of the diffusion tensor in the coordinate system defined by the gradient coils as a function of the diffusion time Δ.

As mentioned in chapter 6, the NV-center's sensitivity has a strong dependence on the sample geometry. To exclude any effects due to this effective weighing of the sample volume, we can derive a description of the NV-center's weighting function. Since we can simulate each sample volume's contribution to the detected signal, we can use the amplitude of this as

the relative weights for the diffusion signal:

$$c(\vec{r}) = \int_0^T |\vec{B}_{\text{spin}||}(\vec{r}, t)|\, dt\, \frac{1}{C}\,, \tag{8.4}$$

where C is a normalization factor chosen such that:

$$\int c(\vec{r})\, dV_{\text{sample}} = 1\,. \tag{8.5}$$

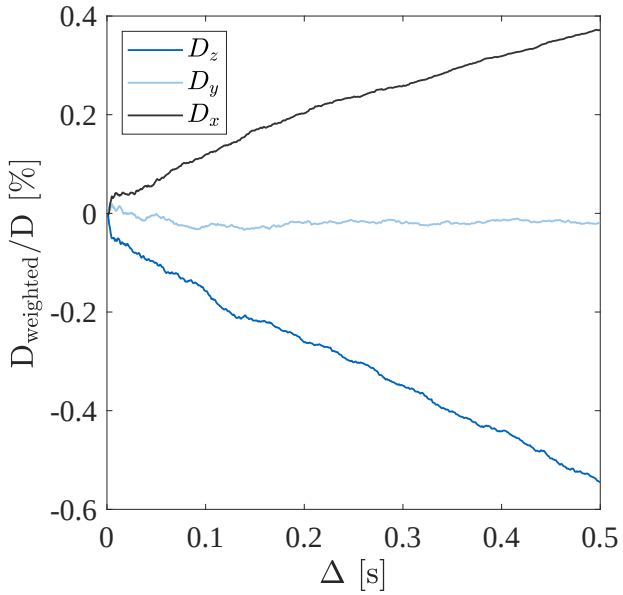

Figure 8.3.: **Expected deviation from the theoretical ADC due to the NV geometry dependence.**
The difference between the simulated weighted diffusion coefficient and the theoretical value. The difference stays below 0.5 % in all directions for the first half second.

Now we can define a position weighted diffusion coefficient according to:

$$D_{weight,\hat{x}_i}(t) = \frac{1}{2t} \int c(\vec{r})\, [\hat{x}_i \cdot (\vec{r}_0 - \vec{r}(t))]^2\, dV_{\text{sample}}\,. \tag{8.6}$$

The difference between the values is plotted in Fig. 8.3 for the standard microfluidic channel used in most experiments. The difference between the analytical and weighted values is

negligible for the duration of our diffusion experiments.

8.2. The pulsed gradient spin echo experiment

The PFG-NMR method used in the experiments in this chapter is called pulsed gradient spin echo (PGSE).[159] It is a modification of the classic Hahn-echo experiment, where before and after the refocusing π-pulse two B_0-gradient pulses inducing the same dephasing are applied along $\hat{x}$, $\hat{y}$ or $\hat{z}$.

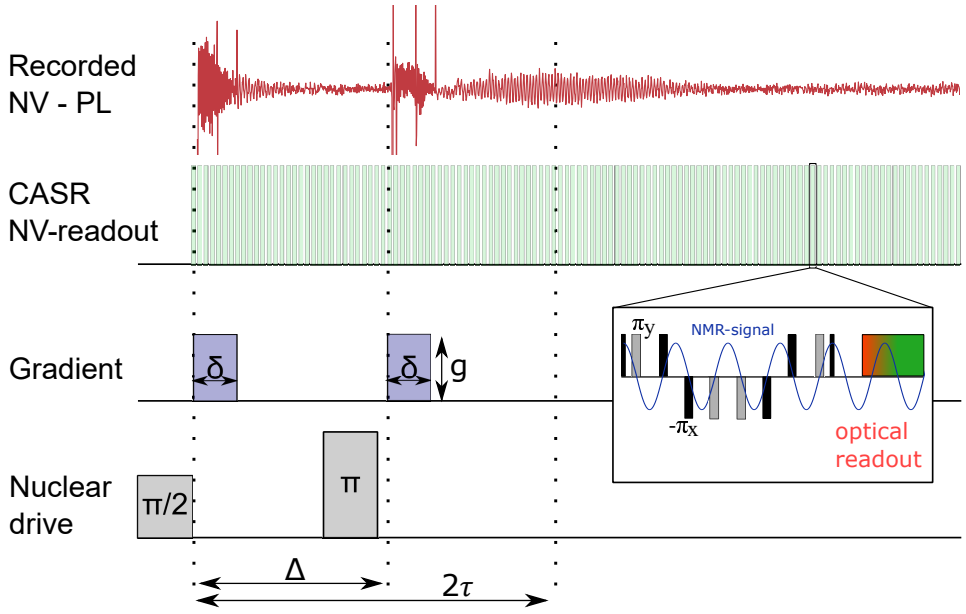

Figure 8.4.: **The PGSE sequence**
The polarized nuclear population is rotated into the Bloch sphere's XY-plane using a $\pi/2$-pulse. After a waiting time τ the spin population is inverted by a π-pulse. Before and after the π-pulse two gradient pulses are applied. Both pulses are of equal length δ and strength g and separated by a time Δ. The NMR-signal is read out starting right after the initial $\pi/2$-pulse using CASR. In the first row a red experimental PGSE-data can be seen, including B_0 offsets during the gradient pulses.

The first gradient pulse leads to a relative phase-accumulation of each individual sample spin depending on position, the latter leads to a refocusing as described in chapter 6. The refocusing of the individual phases depends on the amout each spin has diffused along the

applied gradient direction. The sequence can be seen in Fig. 8.4. In the original PGSE paper, the echo amplitude was calculated to be:[159]

$$\begin{aligned}\log(A(\vec{g})/A_0) = -\gamma^2 D\Bigg(& \frac{2}{3}\tau^2 g_0^2 + \delta^2 g^2 (\Delta - \frac{1}{3}\delta) \\ & - \delta \left[(t_1^2 + t_2^2) + \delta (t_1 + t_2) + \frac{2}{3}\delta^2 - 2\tau^2 \right] \vec{g} \cdot \vec{g}_0 \Bigg) ,\end{aligned} \tag{8.7}$$

where $\vec{g}$ and $\vec{g}_0$ are the pulsed and constant background gradient-amplitudes respectively. $A(\vec{g})$ and A_0 are the echo amplitudes of the PGSE-data sets with gradients $\vec{g}$ and $\vec{g} = 0$, respectively. δ indicates the length of the pulsed gradients and Δ their spacing. τ is the spacing of the π and $\pi/2$-pulses and t_1 and t_2 are the times before the first gradient pulse and after the second gradient pulse but before the echo respectively.
In the case of $g \gg g_0$:

$$\log(A(\vec{g})/A_0) = -D\,\gamma^2\,\delta^2\,g^2\,(\Delta - \frac{1}{3}\delta)\,. \tag{8.8}$$

As proof of principle experiments to test our setup we conducted measurements of the diffusion coefficient of different concentrations (0%, 10% and 20% w/w) of polyvinylpyrrolidone K90 (PVP) in water. The diffusion properties of PVP-water solutions has been investigated in detail[167–169] and are therefore a good base for these experiments. The ADC was measured using a varying amplitude of the g_z gradient. This direction was chosen, since the ADC should be close to the free diffusion coefficient in this direction, at least on the time scales of our experiment. The ADC of pure water at 25°C is found to be about $ADC_{lit,0\%} \approx 2.3 \times 10^{-9}\,\mathrm{m}^2/\mathrm{s}$.[163–165] Simulating the mean squared displacement using this free diffusion coefficient in a cuboid of side length 80 x 100 x 1000 $\mu\mathrm{m}^2$, we obtain with $ADC_{sim,0\%} = 2.14 \times 10^{-9}\,\mathrm{m}^2/\mathrm{s}$. This agrees well with the measured diffusion coefficient of $ADC_{meas,0\%} = 2.27 \times 10^{-9}\,\mathrm{m}^2/\mathrm{s}$, seen in Fig. 8.5.

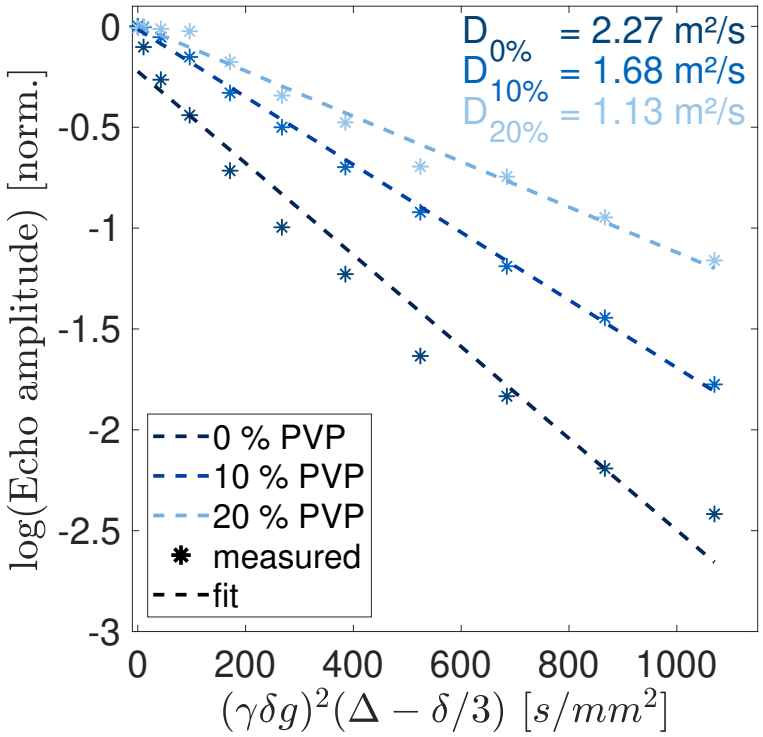

Figure 8.5.: **Proof of principle PGSE measurements**
The measured diffusion coefficient for different concentrations of PVP in water. All Echo amplitudes have been normalized to the initial measurement, without gradient.

The expected ADC for the concentrations of 10% and 20% w/w at $T = 25^\circ C$ can be calculated by:[167]

$$\begin{aligned} D_{app,10\%} &= 1.594 \, \frac{\mu \mathrm{m}^2}{\mathrm{ms}} \, \exp\left(0.02531 \, \frac{1}{\mathrm{K}} \, (T - T_0)\right) \\ D_{app,20\%} &= 1.197 \, \frac{\mu \mathrm{m}^2}{\mathrm{ms}} \, \exp\left(0.02749 \, \frac{1}{\mathrm{K}} \, (T - T_0)\right) , \end{aligned} \tag{8.9}$$

where $T_0 = 20^\circ C$, resulting in $ADC_{lit,10\%} = 1.81 \times 10^{-9} \, \mathrm{m}^2/\mathrm{s}$ and $ADC_{lit,20\%} = 1.37 \times 10^{-9} \, \mathrm{m}^2/\mathrm{s}$. Simulating the expected ADC for these mixtures, we expect $ADC_{sim,10\%} = 1.69 \times 10^{-9} \, \mathrm{m}^2/\mathrm{s}$ and $ADC_{sim,20\%} = 1.27 \times 10^{-9} \, \mathrm{m}^2/\mathrm{s}$. The measured values seen in Fig. 8.5 $ADC_{meas,10\%} = 1.68 \times 10^{-9} \, \mathrm{m}^2/\mathrm{s}$ and $ADC_{meas,20\%} = 1.13 \times 10^{-9} \, \mathrm{m}^2/\mathrm{s}$, which are in good

agreement with the theoretical predictions.

8.3. Measuring anisotropic diffusion

While most experiments in this thesis have been conducted using the straight microfluidic channel described in chapter 7, a separate channel was designed to conduct PGSE-measurements probing the channel's anisotropy. The chip can be seen in Fig. 8.7, it was probed on three distinct locations, which were imaged in parallel using our camera. Results of these measurements can be found in table 8.3. Especially the difference of the diffusion in $\hat{x}$-direction is clearly visible from the experimental data.

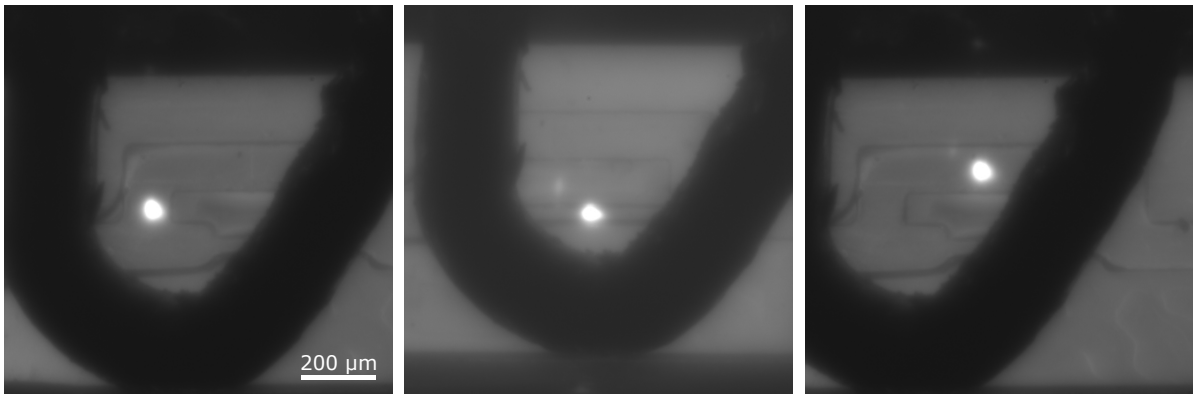

Figure 8.6.: **The laser spots measured in the microfluidic chip**
Three images taken at three of the spots measured in the microfluidic channel.

The spatial resolution of this experiment was limited by the thickness of the NV-layer on the diamond surface ($\sim 50\ \mu$m) and the width of the laser spot (fitted using a two dimensional Gaussian model to have a standard deviation of $\sigma \approx 14.5\,\mu$m). Photos of the typical laser spots can be seen in Fig. 8.6. Using shallower NV-layers and focusing the laser onto even smaller areas can easily lead to spatial resolutions on the order of $\sim 1\ \mu$m.

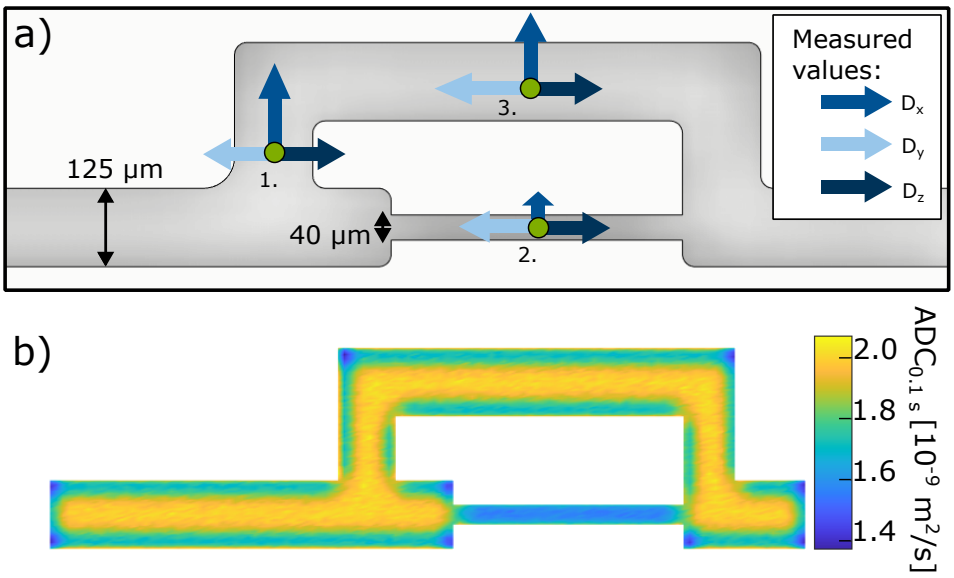

Figure 8.7.: **Experimental results and simulations of the diagonal elements of the ADC** **a)** Measurements of the diffusion coefficients at three distinct spots. The y (light blue) and z (dark blue) directions are not in the picture plane as described in Fig. 8.1. **b)** The diffusion coefficient simulated in our microfluidic channel. Close to the edges and in the small channel the diffusion coefficient is significantly smaller than in the middle of the wider microfluidic channels.

D $[10^{-9}\, m^2/s]$		spot 1	spot 2	spot 3
D_x	simulated	2.12 ± 0.1	1.25 ± 0.1	1.78 ± 0.1
	measured	2.56 ± 0.33	1.16 ± 0.18	2.11 ± 0.14
D_y	simulated	1.68 ± 0.1	1.78 ± 0.1	1.84 ± 0.1
	measured	1.97 ± 0.22	2.22 ± 0.21	2.67 ± 0.34
D_z	simulated	1.73 ± 0.1	1.94 ± 0.1	2.68 ± 0.08
	measured	1.96 ± 0.18	1.99 ± 0.06	2.0 ± 0.3

Table 8.1.: Averages of measured and simulated values for each of the three cardinal directions and each of the locations investigated with their respective uncertainties.

9. Conclusion and outlook

Quantum sensing has come a long way since the first thoughts of applying single quantum systems as sensors for external fields. The first "of the shelf" quantum sensors are commercially available[26,27] and more and more quantum sensing companies enter the market.[170] On the other side more and more research group enter the field of quantum sensing and especially the field of NV-centers.[171]

In this thesis I have introduced the NV-center and discussed the methods of AC-sensing using this defect in diamond. I have introduced the basics of quantum sensing and different dynamical decoupling sequences. I discussed the different types of NV-centers and their major achievements, such as pico-Tesla sensitivities,[19,87,162] chemically resolved NMR-spectra[19,114] and even the detection of single spins.[17,18] After the introduction into NV-NMR, I have discussed the simulation of NV-NMR experiments as well as of the PGSE experiments[157] demonstrated in this thesis. These simulations are a useful tool for estimating the optimal parameters for the geometry of NV-NMR experiments. I also described the unintuitive effects gradients can have on the NV-NMR signal amplitude. This includes improving the FND amplitude or the possibility to use new detection sequences like AERIS for ⟨100⟩-diamonds, which would not be possible without gradients. Finally I have described the PGSE-experiments themselves, which demonstrated the high potential of the NV-diamond platform. I was able to conduct first proof of principle measurements, and compare them to literature values. Then I detected the anisotropic diffusion in our microfluidic channel.

Still, to really exploit the full potential of this technology much future work is still necessary. The major goal for micron-scale NMR-experiments is to reach even better sensitivities. This is

necessary to be able to detect even lower concentrated samples e.g. individual metabolites within biological tissues.[139] In my opinion the major ways to achieve this are on one hand through engineering: Better diamond materials and fluorescence light collection could greatly benefit the NV-center's sensitivity. Also improved magnetic field homogeneity and a better understanding of the magnetic-susceptibility mismatches at the diamond-sample, diamond-glass and glass-sample interfaces are of major importance. On the other hand there have been various NMR-pulse sequences developed over the decade long NMR-research, which have not been applied to NV-NMR, which could benefit NV-NMR by counteracting the effects of the inhomogeneous fields.[139]

In addition, the experiments need to be conducted at higher magnetic fields. So far reported experiments have not been higher than ~ 0.2 T, increasing this to 1 T and above will not only increase spectral resolution of the chemical shifts, but also the signal amplitude. Again this seems to be an engineering challenge, where the high microwave frequencies necessary to drive the NV-spins pose the major hurdle.

The true potential of the micron-scale NV-NMR setup lies within the ability to highly parallelize the experiments in the wide-field approach especially combined with microfluidic techniques.[76] This can lead to much quicker and higher resolved magnetic resonance imaging than with conventional methods, since all pixels can be imaged simultaneously.[76] Also High throughput-NMR is possible using the high sample control available through the microfluidic platform.[24,138] Maybe the most important development necessary is in the ease of use. For NV-NMR to fully reach potential, researchers from different fields like biology or chemistry need to be able to get easy access to NV-NMR experiments as well as be able to work with them without being an expert. For this to happen the setups need to become much more user-friendly than they currently are.

10. Appendix

A. Time evolution operator, the rotating frame and the rotating wave approximation

A.1. Time evolution operator

In the Schrödinger picture of quantum mechanics, operators in a system are constant, while quantum-states $|\Psi(t)\rangle$ evolve over time. The mathematical description of this usually uses the time evolution operator $\hat{U}(t_1, t_0)$:

$$|\Psi(t_1)\rangle = \hat{U}(t_1, t_0)\,|\Psi(t_0)\rangle \ . \tag{10.1}$$

One important consequence is, that $|\Psi(t_1)\rangle$ still has to fulfil the Schrödinger-equation, therefore:

$$i\hbar\frac{\partial}{\partial t}\hat{U}(t, t_0)\,|\Psi(t_0)\rangle = \hat{H}(t)\hat{U}(t, t_0)\,|\Psi(t_0)\rangle \ , \tag{10.2}$$

which is nicely solvable if $\hat{H}(t_0)$ and $\hat{H}(t_1)$ commute. This is especially true, if $\hat{H}$ is time independent. Since this is the case in the Schrödinger picture of quantum mechanics, the time evolution operator can be written as:

$$\hat{U}(t_1, t_0) = \exp\left(-\frac{1}{\hbar}\int_{t_0}^{t_1}\hat{H}(\tau)d\tau\right) \ . \tag{10.3}$$

Often $t_0 = 0$ in which case it the second parameter is often dropped in the notation: $\hat{U}(t)$.

A.2. The rotating frame

As mentioned before, the rotating frame is a useful tool to describe spin systems in an external magnetic field. To change into the rotating frame, both the Hamiltonian $\hat{H}$ and the quantum state $|\Psi(t)\rangle$ have to be transformed accordingly.
We can define the transformed state as:

$$|\Phi(t)\rangle = \hat{R}\,|\Psi(t)\rangle \ , \tag{10.4}$$

where $\hat{R} = \exp\left(i\frac{\omega_0 t}{2}\hat{\sigma}_z\right)$, since we want to change into a rotating frame at frequency ω_0. Inserting this into the Schrödinger equation:

$$\begin{aligned} i\hbar\frac{\partial}{\partial t}\hat{R}^\dagger\,|\Phi(t)\rangle &= \hat{H}\hat{R}^\dagger\,|\Phi(t)\rangle \\ i\hbar\left(\frac{\partial\hat{R}^\dagger}{\partial t}\,|\Phi(t)\rangle + \hat{R}^\dagger\frac{\partial\,|\Phi(t)\rangle}{\partial t}\right) &= \hat{H}\hat{R}^\dagger\,|\Phi(t)\rangle \ . \end{aligned} \tag{10.5}$$

Multiplying with $\hat{R}$ from the left and reordering the terms, we end up with:

$$i\hbar\frac{\partial}{\partial t}\,|\Phi(t)\rangle = \left(\hat{R}\hat{H}\hat{R}^\dagger - i\hbar\hat{R}\,\frac{\partial\hat{R}^\dagger}{\partial t}\right)|\Phi(t)\rangle = \hat{H}_{rot}\,|\Phi(t)\rangle \ . \tag{10.6}$$

A.3. The rotating wave approximation

The rotating wave approximation (RWA) is an important tool for two level systems. The idea is to change into a rotating frame and neglect fast oscillating terms, resulting in an averaged Hamiltonian.

Starting with a simple two level Hamiltonian $\hat{H}_0$ and a driving Hamiltonian $\hat{H}_1$ describing a field at frequency ω_1 with amplitude Ω:

$$\hat{H} = \hat{H}_0 + \hat{H}_1 = \hbar\frac{\omega_0}{2}\hat{\sigma}_z + \hbar\Omega\,\cos(\omega_1 t + \theta)\hat{\sigma}_x \ , \tag{10.7}$$

we can change into the rotating frame, according to equation 10.6:

$$\hat{H}_{rot} = \hbar\Omega \cos(\omega_1 t + \theta) \left(\cos(\omega_0 t)\hat{\sigma}_x - \sin(\omega_0 t)\hat{\sigma}_y\right) \ . \tag{10.8}$$

Assuming $|\omega_1 + \omega_0| \gg |\Omega|$ we can use the RWA. As mentioned above, the idea is that terms rotating much faster than the driving frequency will average out:

$$\int_0^{2\pi/\Omega} \sin(\omega_x \tau) d\tau = \frac{\sin(2\pi \ \frac{\omega_x}{\Omega})}{\omega_x} \approx 0 \ , \tag{10.9}$$

where $x \in 0, 1$. An example can be seen in Fig. 10.1.

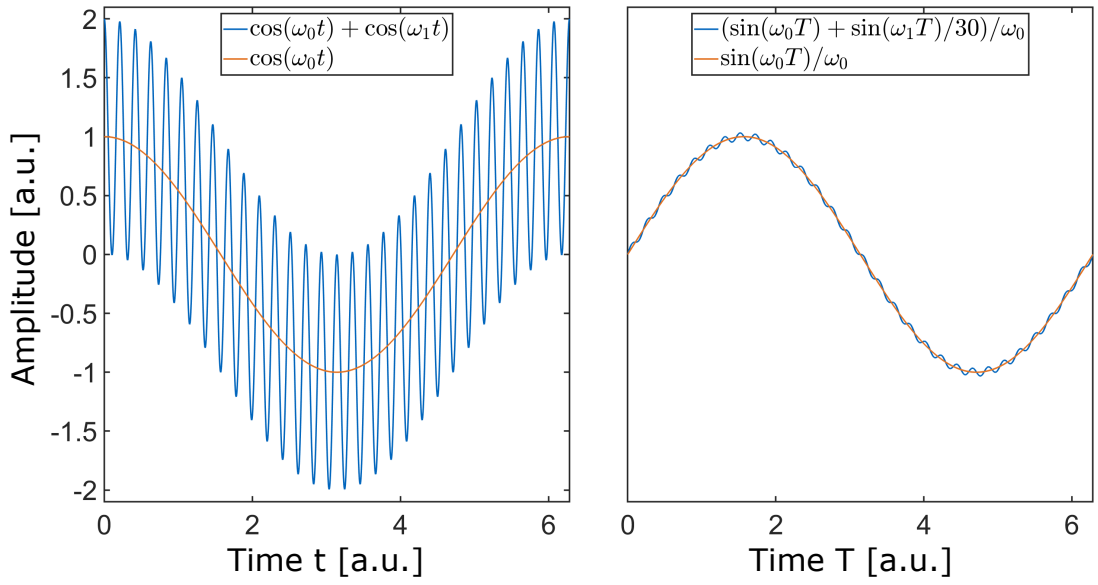

Figure 10.1.: **The rotating wave approximation**
a): The function $\cos(\omega_0 t) + \cos(\omega_1 t)$ (blue) and $\cos(\omega_0 t)$ (orange) for $\omega_1 = 30\omega_0$.
b): The integral of the two functions as function of $T = \frac{2\pi}{\omega_0}$.

Applying the RWA to equation 10.8:

$$\hat{H}_{rot} = \frac{\hbar\Omega}{2} \begin{pmatrix} 0 & \exp(-i(\omega_0 - \omega_1)t - i\theta) \\ \exp(i(\omega_0 - \omega_1)t + i\theta) & 0 \end{pmatrix} \ . \tag{10.10}$$

If the driving field is on resonance, $\omega_0 = \omega_1$:

$$\hat{H}_{rot} = \frac{\hbar\Omega}{2}(\cos(\theta)\hat{\sigma}_x + \sin(\theta)\hat{\sigma}_y) \ , \tag{10.11}$$

with a time evolution operator:

$$\hat{U}(t) = exp\left(-i\frac{\Omega t}{2}(\cos(\theta)\hat{\sigma}_x + \sin(\theta)\hat{\sigma}_y)\right) \ . \tag{10.12}$$

B. CASR: Calibration and variants

CASR is the main method of NMR-signal detection used in this thesis. A detailed overview of CASR can also be found in Glenn et al.[87] and Schmidt.[171]

B.1. CASR-basics

Heterodyne detection

The basic idea of CASR is the detection of a heterodyne beating of the signal frequency slightly detuned to the main peak of the DD-sequence's filter function. Looking at equation 4.10:

$$p_{\text{coherent}}(t) = \frac{1}{2}\left[1 - \cos\left(4\gamma B_{max} t \cos(\alpha)\right)\right] \ , \tag{10.13}$$

where we have neglected the small detuning $\delta f \ll f_0$. The strong dependence on the initial phase of the signal α with respect to the first $\pi/2$-pulse is obvious.

As seen in Fig. 10.2, CASR consists of several consecutive measurements, where each measurement is spaced an integer number N of $\Delta t = N/f_0$ apart. This leads to an change in the initial phase of measurement n: $\alpha_{n+1} = \alpha_n + \Delta t\, \delta f$ and in turn to a signal fluorescence oscillating at the beating-frequency δf.

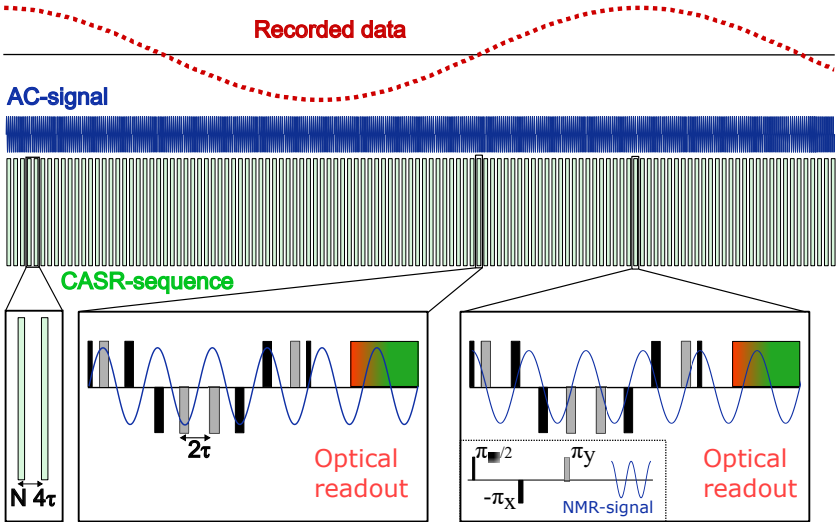

Figure 10.2.: **Coherently averaged synchronised readout**
A Sketch of the CASR sequence. The spacing of the individual DD-sequences is a multiple of a frequency close to the target AC-frequency (blue). The relative difference between the initial phase of the AC-frequency with respect to the start of each individual CASR-block (green rectangles), leads to an oscillation in the phase accumulation during each block. This in turn leads to an oscillation in the recorded fluorescence-data. The two inlets in the bottom right illustrate the two extreme cases: the first having a relative phase leading to minimal signal amplitude, the second leading to maximum signal amplitude.
This figure is also shown in chapter 4.

Variations of CASR

There are a few variations of CASR, the one described above was first shown in Glenn et al.[87] A very similar protocol called quantum heterodyne detection (Qdyne) described in Schmitt et al.[110,112,171] The only difference to the protocol above, is the removal of the detuning δf. Instead the phase acquisition between each measurement step comes from a separation $\Delta t = N/f_0 + \delta t$, which leads to a phase at measurement n: $\alpha_{n+1} = \alpha_n + \delta t\, f_0$. this scheme has the advantage of not losing sensitivity due to the small detuning away from the DD-sequence's filter function. Unfortunately it comes with some technical challenges described in section B.3.

A third protocol is used for mapping the initial phase of the sensing signal onto a constant oscillation amplitude.[111] This protocol has both conditions $\Delta t = k/f_0$ and $\delta f = 0$. For a signal

with time-independent relative phase $\alpha(t) = \alpha(0)$ each measurement would result in the same fluorescence amplitude. This is circumvented by oscillating the phase of the last $\pi/2$-pulse with a frequency f_{phase}. Effectively this switches between cosine and sine magnetometry at a frequency f_{phase}, leading to an oscillation of the NV-fluorescence with amplitude. This gives the ability to detect changes in the signal phase as a function of the CASR-amplitude.

B.2. CASR-calibration

The signal detected by the CASR-protocol can be estimated as described in chapter 6. Still it is of use to calibrate the experiment, not only to also determine its sensitivity.

To do so, the effects of an external field of constant amplitude $B_{ext} = b_{ext}\ \sin(\omega_{ext}t + \phi)$ is measured. Here b_{ext} is the fields amplitude, $\omega_{ext} = 2\pi\, f_0 + \delta\omega$ is the external fields known angular frequency and $\phi = 0$ is its phase. Neglecting finite pulse width, the accumulated phase due to the integrated magnetic field seen by the NV-centre can be calculated to be:

$$\begin{aligned}
\Delta\phi_{NV} &= \frac{2g\mu_B}{\hbar} B_{\text{integrated}} \\
&= \frac{2g\mu_B}{\hbar} \int_0^{2N\tau} |b_{ext}\ \sin(\omega_{ext}t)|dt \\
&= \frac{g\mu_B}{\hbar}\ \frac{b_{ext}}{\omega_{ext}} \left[\sin(\omega_{ext}\frac{\tau}{2}) - 2\sin(\omega_{ext}\frac{\tau}{4})\right] \\
&\approx \frac{2g\mu_B}{\hbar}\ \frac{b_{ext}}{\omega_{ext}}\ ,
\end{aligned} \tag{10.14}$$

where 2τ is the π-pulse spacing in the CPMG-like DD-sequence, μ_B is the Bohr-magneton and $g \approx 2$ is the electron g-factor. In the last step we have neglected the detuning and assumed $\omega_{ext} \approx 1/(4\tau)$.

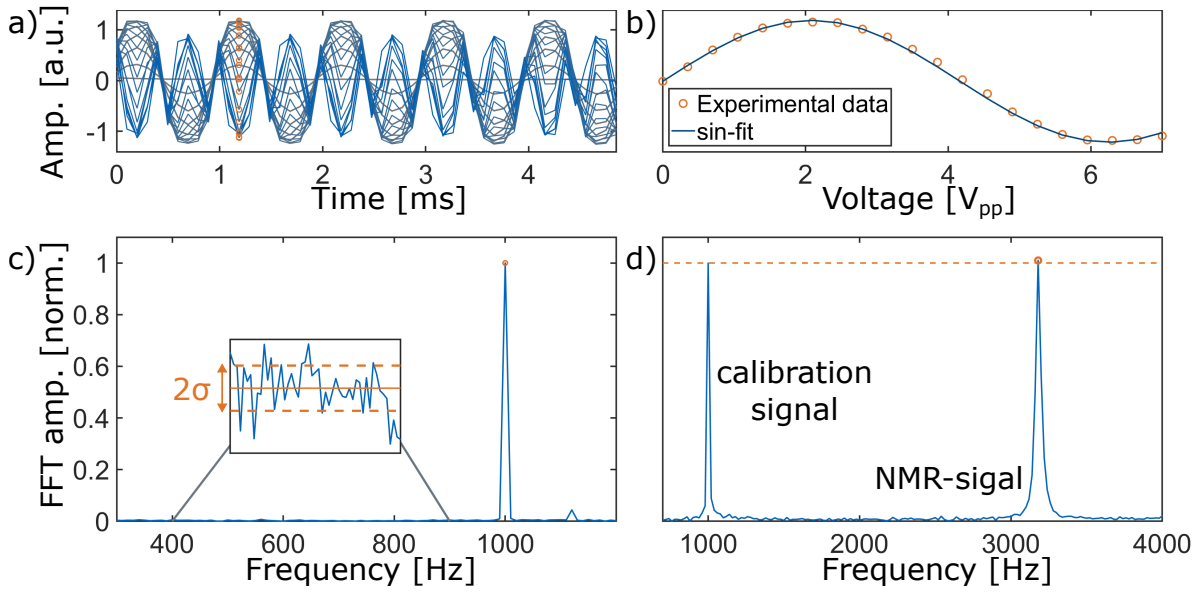

Figure 10.3.: **CASR calibration**
a): A calibration measurement, the first oscillations of the CASR experiment are plotted, with varying external field amplitude b_{ext}. **b)**: One of the anti-nodes is chosen, indicated by the orange circles in a). The anti-nodes' amplitudes are plotted as a function of the applied Volt at the calibration coil. And the magnetic field per applied Volt is calculated according to equation 10.14. **c)**: The voltage is set to generate a signal of $b_{ext} = 10$ nT, and averaged over a total time of 1 s. From this measurement the sensitivity of the experiment can be calculated, using the standard deviation of the complex noise-floor. **d)**: The NMR-signal size can be calculated by the relative integrals of the NMR and the calibration peak, which is approximated by the relative SNR for low bandwidth beaks.

The setup's sensitivity can be calculated using the experiment described in Fig. 10.3. The amplitude of the external field is swept, and the resulting maximum oscillation-frequency of the CASR signal-amplitude allows for the estimation of the calibration-signals amplitude in Tesla at the NV-ensemble position.

Averaging an external field of now known amplitude $b_{ext} = 10$ nT for 1 s, allows us to calculate the sensitivity according to:

$$\eta = b_{ext}/SNR\,. \tag{10.15}$$

Finally the NMR-signal amplitude can be calculated by the relative amplitude of the external signal and the NMR-signal, as seen in Fig. 10.3 c).

B.3. CASR: Technical challenges

In this section I want to outline two challenges of using CASR. The first is the problem of increasing the NV-ensembles dephasing time. Of course this is of interest, since the total number of π-pulses in the DD-sequence and therefor the interaction time of the NV-ensemble and the NMR-signal can be increased. This in turn leads to higher sensitivity, as described in chapter 2. Sadly the frequency bandwidth of the CASR spectrum is determined by the repetition frequency of measurements. Increasing the dephasing time leads to smaller bandwidths, which in turn makes finding the NMR frequency in the NV-NMR setup more difficult. In addition the setup is more sensitive to low frequency (< 1 kHz) noise, for example fluctuations in laser intensity, which means it might be more likely to be influenced by close by noise-frequencies in the frequency domain.

Overall the increase of the coherence time is still highly desirable!

A second minor issue is the problem of the AWGs granularity. Every AWG has a finite resolution, which in turn limits the number of frequencies f_0 at which the total measurement separation can be an integer multiple of $1/f_0$ as well as the number of frequencies that can be represented by the separation $\tau = \frac{1}{4f_0}$. For this reason it is difficult to implement the Qdyne protocol for NMR frequencies, since the exact frequencies $f_0 = \frac{1}{4\tau}$ that can be represented by the AWG seldom match the NMR-frequency.

C. Mathematical description of NMR

The goal of this chapter is to give a brief overview of NMR using a semi-classical description. I will follow the relevant chapters in Callaghan[92] and also Keeler,[94] so refer to their respective derivations for further information.

C.1. Semi-classical description of Lamor-precession

Limiting ourselves to the case of spin-$\frac{1}{2}$ nuclei, we can describe the ensemble of sample spins using the ensemble magnetization $\vec{M}$. This is possible since all spins will either be parallel or anti-parallel to $\vec{B}_0$. The angular momentum of the ensemble magnetization is $\vec{M}/\gamma$. The torque of the system is defined as:

$$\vec{L} = \frac{d\vec{M}}{dt} = \gamma\vec{M} \times \vec{B}_0 \, . \tag{10.16}$$

This leads to the Lamor-precession frequency of the system:

$$\omega_0 = \frac{\Delta\phi}{\Delta t} = \hbar\frac{\mu B_0 \sin(\theta)\Delta t}{L \sin(\theta)\delta t} = \hbar\gamma B_0 \, . \tag{10.17}$$

Here μ denotes the spins magnetic moment and θ the angle of nutation from the z-axis defined by $\hat{B}_0$. With this, we can move into the rotating frame and use a transverse driving field B_1 for spin manipulation as described in section 2.4.1.

C.2. Pure states, mixed states and the density matrix

The quantum-mechanical description of NMR builds on the concept of the density matrix $\rho = \sum_\Psi p_\Psi |\Psi\rangle \langle\Psi|$, where p_Ψ is the probability of the ensemble-state Ψ. This can be represented as a matrix with entries $\langle m| \rho |m'\rangle = \overline{a_m a^*_{m'}}$, where m, $m' \in 0, 1$ for a two-level system.
This leads to a number of important properties:

1. The diagonal elements $\langle m| \rho |m\rangle$ represent measurement probabilities and need to be real numbers with $\sum_m \langle m| \rho |m\rangle = Tr(\rho) = 1$.

2. ρ is Hermetian, so $\rho = \rho^\dagger$

3. If the system is in a known quantum state, e.g. after initialization, then $p_\Psi = 1$ for one given Ψ. This is called a pure state with the additional property $Tr(\rho^2) = Tr(\rho) = 1$.

If the density matrix of a system is not in a pure state, this means some information about

the system has been lost, e.g. through relaxation or dephasing. In the Bloch-picture pure states are on the surface of the Bloch-sphere. If the system is not in a pure state, the state is called "mixed".

It is worth mentioning, that the probabilities p_Ψ are not necessarily the same as the quantum-mechanical probabilities depending on a superposition state, but in general is a probability arising from the number of microstates of the system, akin to the discussion of polarization in chapter 4!

C.3. Quantum mechanical view of nutation

Looking at a spin-$\frac{1}{2}$-ensemble in a magnetic field $\vec{B}_0$, we can describe the initial state as:

$$\rho(0) = \begin{pmatrix} p_0 & 0 \\ 0 & p_1 \end{pmatrix} , \tag{10.18}$$

since only the excess spin polarization contributes to the signal, we write:

$$\rho(0) = \frac{1}{2}\begin{pmatrix} 1 & 0 \\ 0 & 1 \end{pmatrix} + \frac{1}{2}\begin{pmatrix} (p_0 - p_1) & 0 \\ 0 & -(p_0 - p_1) \end{pmatrix} . \tag{10.19}$$

If we now apply a $\pi/2$-pulse th the system:

$$\begin{aligned} \rho(\pi/2) &= \hat{U}^{pulse}(t_{pulse})\ \rho(0)\ \hat{U}^{pulse}(t_{pulse})^{-1} \\ &= \begin{pmatrix} \sqrt{2}^{-1} & i\sqrt{2}^{-1} \\ i\sqrt{2}^{-1} & \sqrt{2}^{-1} \end{pmatrix} \begin{pmatrix} (p_0 - p_1) & 0 \\ 0 & -(p_0 - p_1) \end{pmatrix} \begin{pmatrix} \sqrt{2}^{-1} & -i\sqrt{2}^{-1} \\ -i\sqrt{2}^{-1} & \sqrt{2}^{-1} \end{pmatrix} \\ &= \frac{1}{2}\begin{pmatrix} 1 & -i\,(p_0 - p_1) \\ i\,(p_0 - p_1) & 1 \end{pmatrix} . \end{aligned} \tag{10.20}$$

This means the population $|0\rangle$ has been mapped to a state $|\Psi\rangle = \sqrt{2}^{-1}|1\rangle + i\sqrt{2}^{-1}|0\rangle$ and the population formerly in $|1\rangle$ has been mapped to a state $|\Psi\rangle = i\sqrt{2}^{-1}|1\rangle + \sqrt{2}^{-1}|0\rangle$. The

Lamor-precession follows from the energy difference of the two levels of the superposition state, as described in section 2.1.

D. Overhauser polarization

Overhauser dynamic nuclear polarization (ODNP) is th e first way DNP has been shown.[96] The general idea of the method is to transfer the thermal polarization of spins with a high gyromagnetic ratio, mostly electron spins $\gamma_e = 28.025$ GHz/T, to spins with a lower gyromagnetic ratio, for example proton spins $\gamma_p = 42.577$ MHz/T. This is useful, since the gyromagnetic ratio determines the magnitude of the Zeeman-shift $\Delta E \alpha \gamma B_0$ and the thermal polarization of a spin ensemble follows from the Boltzmann-distribution, as described in chapter 4. In our experiments we use a $\sim$ 10 mM solution of Tetramethylpiperidinyloxyl (TEMPO) in water, where TEMPO contains a stable radical.

The free radicals diffuse within the sample and interact with the proton nuclear-spins, in an external magnetic field B_0:

$$H_0 = \omega_e S_z + \omega_p I_z + A S_z I_z + B S_z I_x \, , \tag{10.21}$$

where ω_e and ω_p are the electron and proton Lamor-frequencies, $\hat{I}$ and $\hat{S}$ are the nuclear and electron spin operators in the Zeeman-basis and A and B secular and pseudo-secular parts of the hyperfine-interaction. During the DNP-step, a strong driving field is applied at frequency ω_e with amplitude Ω, leading to a rotating frame Hamiltonian:

$$H_{rot} = \omega_p I_z + A S_z I_z + B S_z I_x + \Omega S_x \, . \tag{10.22}$$

So the driving frequency continuously transfers electron polarization between $|0\rangle$ and $|1\rangle$ state, which will lead to polarization transfer through single quantum transitions due to mixing arising from the B-term.

In a different approach, we can look at the relative population of each hyperfine level and

the magnetization of the electron ensemble M_z^S and proton ensemble M_z^I:[19]

$$\begin{aligned} &M_z^I \alpha (p_{\downarrow\uparrow} + p_{\uparrow\uparrow} - p_{\downarrow\downarrow} - p_{\uparrow\downarrow}) \\ &M_z^S \alpha (p_{\downarrow\uparrow} + p_{\downarrow\downarrow} - p_{\uparrow\uparrow} - p_{\uparrow\downarrow}) \, . \end{aligned} \tag{10.23}$$

Here $p_{e,n}$ refers to the population with spin projection of electron e and nuclear spin n respectively.

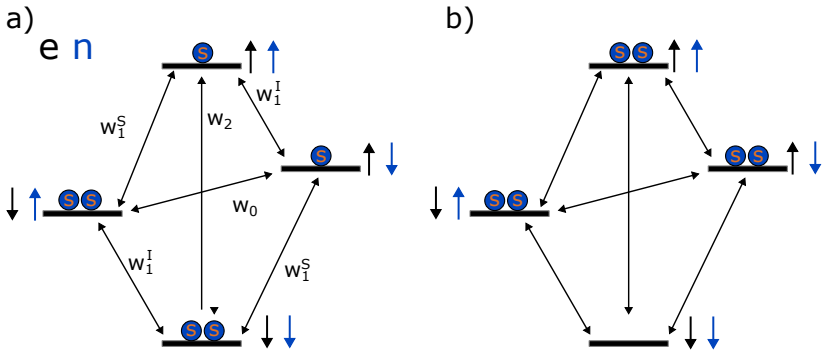

Figure 10.4.: **Overhauser polarization**
Sketch of a coupled electron-proton systems population before (**a)**) and after (**b)**) ODNP. Electron-spins are displayed as black and nuclear spins are displayed as blue arrows.

The change in nuclear and electron magnetization therefore depends on the change of the $p_{\downarrow\downarrow}$ and $p_{\uparrow\uparrow}$ respectively. it can be shown[19,172] that:

$$\frac{dM_z^I}{dt} = -(w_0 + 2w_1^I + w_2 + w^0)[M_z^I(t) - M_z^I(\infty)] - (w_2 - w_0)[M_z^S(t) - M_z^S(\infty)] \, , \tag{10.24}$$

where w_0, w_1^I and w_2 denote the transition probabilities shown in Fig. 10.4, $M(\infty)$ is the equilibrium magnetization and w^0 is a variable referring to all other relaxation and dephasing processes. After a long enough radiation to reach steady state conditions, typically on the order of $t_{st} \sim 0.1$ s, the change in proton magnetization can be written as:

$$M_z^I(t_{st}) - M_z^I(\infty) = -\frac{w_2 - w_0}{w_0 + 2w_1^I + w_2 + w^0}[M_z^S(t) - M_z^S(\infty)] \, . \tag{10.25}$$

The actual enhancement in strongly dependent on the sample species as well as the magnetic field operated at, since this derivation assumes a simple electron-nucleus system and neglects any other spins.

E. Geometry dependence of nano-scale NV-NMR

Since nano-scale NMR measures the root-mean-squared (RMS) field of the statistical polarized sample, there is no dependence on the sample-spin orientation due to the averaging.[89–91,95,173]

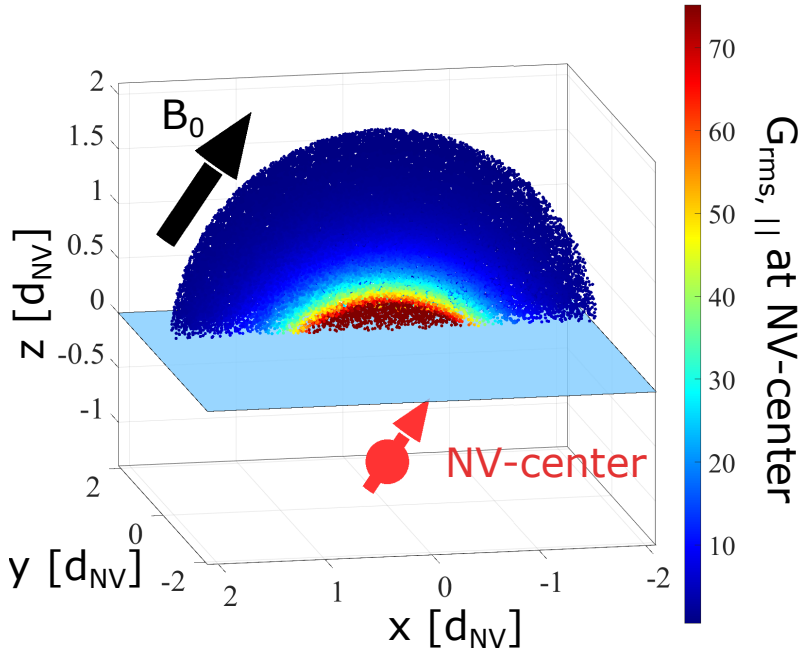

Figure 10.5.: **The sensitivity map for a statistical polarized sample**
Analytical results of the geometry dependence of a single NV-centre in a ⟨100⟩-cut diamond, measuring statistical polarization. The sample is only shown in half of the sample-filled space, for better visibility.

Similar to the micro-scale case, the number of sample spins increases with r^3 for each hemisphere of distance r from the NV-centre, while the dipolar field of each individual spin drops as $\frac{1}{r^3}$, leading to a net constant contribution of each shell. The overall dependence thus

only originates from two different parameters: **1)** The increase in sample spins per distance r means the statistical polarization of each of these shells is going to be progressively smaller. **2)** The first dot product in the dipolar field equation (see equation 4.1) $\vec{r} \cdot \hat{B}_0$ will lead to a varying contribution depending on the diamond cut.

The effects of this is illustrated in Fig. 10.5 Overall signal contribution of a spin at position $\vec{r}$ can be written as:[90]

$$\langle B^2 \rangle \approx \frac{1}{V_S} \int dV f(\vec{r})^2 \langle m_z^2 \rangle + (g(\vec{r}) \sin(\gamma))^2 \langle m_\perp^2 \rangle \ , \tag{10.26}$$

where $\langle X \rangle$ denotes an average over the variable X, m_z and $m_\perp$ are the parallel and orthogonal components of the sample-magnetization with respect to B_0 and γ is the angle between the diamond surface-normal and $\hat{B}_0$. The functions $f(\vec{r})$ and $g(\vec{r})$ are defined as:

$$\begin{aligned} f(\vec{r}) &= \frac{3\cos^2(\gamma) - 1}{r^3} \\ g(\vec{r}) &= \frac{3\cos(\gamma)}{r^3} \ . \end{aligned} \tag{10.27}$$

F. Diamond-growth: CVD and HPHT

The two prevalent methods of synthetic diamond creation are CVD and HPHT. Both function fundamentally different and result in very different end-products.

F.1. High pressure high temperature

The HPHT method uses high pressure (> 5 GPa) and high temperatures ($\approx$ 1250°C) to mimic the natural diamond formation.[43] Hereby graphite is dissolved with a seed-diamond and a metal catalyst, which increases the diamond growth rate and control over the growth process.[174] Nitrogen easily mixes into the dissolved carbon and is one of the most prevalent impurities in HPHT-grown diamonds,[43,49,174,175] which typically are of type I. This poses a problem for NV-NMR, due to a strong fluorescence from the bulk diamond compared to the comparatively shallow sensing-layer.

F.2. Plasma enhanced chemical vapour deposition

CVD grown diamonds have some major advantages compared to HPHT-grown diamonds. While more costly and slower to produce, the control over the growth process is much higher, allowing for isotopically enriched and basically defect free diamonds to be grown.[43,49] Typically a diamond-seed is exposed to methane-hydrogen-plasma, leading to homoepitaxial growth of the diamond. Hereby radicalised carbon atoms bond to the diamond surface, though the growth rate of CVD grown diamonds can vary drastically, depending on the diamond orientation.[43]

For mico-scale NV-diamonds, nitrogen is incorporated into the plasma, which leads to the growth of nitrogen-enriched diamond layers.

Compared to the HPHT-approach, CVD diamonds are typically of type IIa, which makes them favourable for NV-NMR experiments.

G. NV^0-centres and substitutional nitrogen

In all NV-ensembles, first nitrogen and vacancies are introduced to the diamond afterwards there is an additional annealing step, to convert the substitutional N-atoms (p-centres) into NV-centres. Increasing the conversion rate from p-centres to NV-centres is highly desirable, since p-centres are one of the main causes of magnetic noise in the diamond, reducing the dephasing time of the NV-centres and therefore the NV-NMR setups sensitivity.

The second most prevalent undesired nitrogen-defect is the uncharged NV^0 centre. Due to various optical and non optical conversion methods between NV^0 and NV^-, it is impossible to get completely rid of them in the diamond sample,[43,45,58] though these conversion processes can be understood and minimized. The extent of the NV^0-centres effect on NV-centre dephasing time is not completely understood, though too high concentrations will be detrimental. One of the major problems is, that the NV^0-centre is optically active at similar, though slightly lower wavelengths than the NV-centre. The NV^0-fluorescence can be filtered out partially using optical bandpass-filters.

H. Magnetic field dependence of the NV-fluorescence

The magnetic field dependence of an NV-centre can be seen in Fig. 10.6. initially, there is a sharp drop in NV-fluorescence, which originates from spin mixing of the non-aligned NV-centres, who's ZFS-splitting is no longer the dominant term for the spin-quantization axis.[58,176,177] The remaining sharp features correspond to several hyperfine transitions. The first feature at about 51.2 mT is attributed to an excited state level anti-crossing (ESLAC), which corresponds to an anti-crossing of the NV-centre's excited $m_s = -1$ and $m_s = 0$ state.[58,177] Next the feature at 59.0 mT is attributed to cross relaxation between the aligned an non-aligned NV-centres in the diamond. The last sharp feature is at 102.4 mT is the ground state level anti-crossing (GSLAC). It originates due to an anti crossing of the NV-centre's ground $m_s = -1$ and $m_s = 0$ state.[58,177]

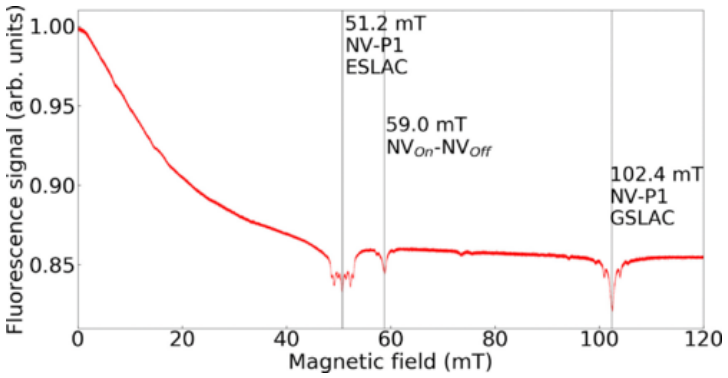

Figure 10.6.: **Normalized NV-fluorescence as a function of magnetic field**
Taken from reference[177] with permission of the American Physical Society.

I. Theory of IQ-mixers

As described in chapter 7, we mostly use our IQ-mixers for the up-conversion process. For this we connect the two AWG outputs to the mixer's I and Q channel:

$$\begin{aligned} I &= A_I \sin(\omega_I t + \phi_I) \\ Q &= A_Q \sin(\omega_Q t + \phi_Q) \,, \end{aligned} \tag{10.28}$$

where A_x and ω_x are the amplitude and angular frequency of the I and Q channel.

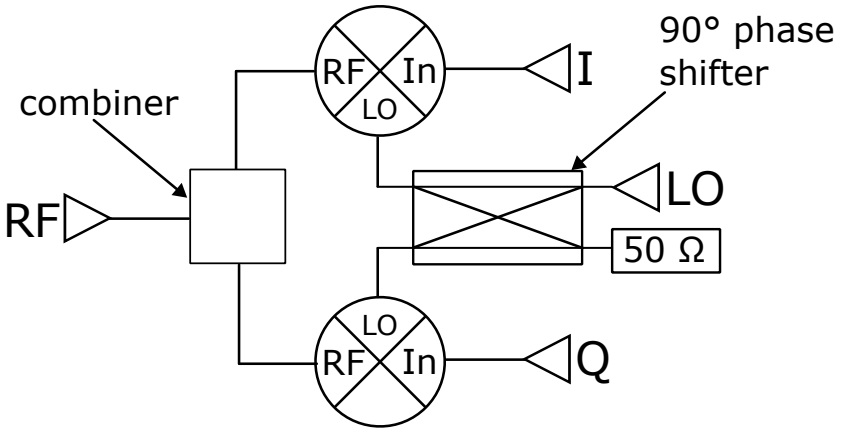

Figure 10.7.: **Schematic of an IQ-mixer**
I, Q and LO inputs are mixed as described in this section, resulting in the RF-output.

For our applications $A_I = A_Q \equiv A$, $\omega_I = \omega_Q \equiv \omega$ and $\phi \equiv \phi_I = \phi_Q - \pi/2$:

$$\begin{aligned} I &= A\ \sin(\omega\, t + \phi) \\ Q &= A\ \cos(\omega\, t + \phi)\ . \end{aligned} \tag{10.29}$$

The local oscillator (LO) input is connected to the signal source with amplitude A_{LO}, angular frequency ω_{LO} and phase $\phi_{LO} = 0$ set to 0 with out loss of generality. In the first step, the LO frequency enters an phase-splitter, so both I and Q channel mix with the LO frequency at a 90° offset. After the two mixers shown in Fig. 10.7, the resulting wave forms can be described as:

$$\begin{aligned} I_{\text{intermediate}} &= A_{LO}\, A\ \sin(\omega\, t + \phi)\, \sin(\omega_{LO}\, t) \\ &= A_{LO}\, A\, \frac{1}{2}(\cos((\omega_{LO} - \omega)\, t - \phi) - \cos((\omega_{LO} + \omega)\, t + \phi)) \\ Q_{\text{intermediate}} &= A_{LO}\, A\ \cos(\omega\, t + \phi)\, \cos(\omega_{LO}\, t) \\ &= A_{LO}\, A\, \frac{1}{2}(\cos((\omega_{LO} - \omega)\, t - \phi) + \cos((\omega_{LO} + \omega)\, t + \phi))\ . \end{aligned} \tag{10.30}$$

This corresponds to two frequency peaks around ω_{LO} separated by 2ω. Though the relative

phases of the peaks in the I and Q intermediate steps is different. This is obviously inefficient, since the power put into the splitter ends up on multiple frequencies instead of one. In the last step the two waveforms are combined. The resulting waveform at the radio frequency (RF) output can be described as:

$$\begin{aligned} \mathrm{RF} &= I_{\mathrm{intermediate}} + Q_{\mathrm{intermediate}} \\ &= A_{LO}\, A\, \cos((\omega_{LO} - \omega)\, t - \phi)\ . \end{aligned} \tag{10.31}$$

Removing the upper side-band from equation 10.30, leaving a single peak in the frequency space. Depending on the relative phase of I and Q channel the upper and or lower side-band can be removed. An even more detailed description of IQ mixers, mixers and how to work with them can be found in reference.[178]

Acknowledgments

I am deeply thankful to my supervisor Dominik Bucher, for guiding me through my PhD and countless discussions about various torments, which our experimental setup had in store for me. He was always available to help and guide me, while always leaving enough space to follow my own ideas and progress autonomously. His greatest quality though, might be his ability to assemble a team of people with great abilities and character, who make Bucherlab a workplace to look forward to going to, even on Mondays.

Many Thanks goes also to my colleagues Robin Allert and Nick Neuling, both of which were of immeasurable value during my PhD, assisting not only with valuable input but contributing essential key pieces to the experimental setup. Many thanks to them also for repeatedly explaining the mysterious world of chemistry to a physicist.

Not to forget Karl Briegel, who next to being of great support during my first publication was always available to talk about Gödel's incompleteness theorem or the future of Bitcoin.

Also many thanks to the Surface-NMR team: Kristina Liu, Roberto Rizzato, Fabian Freire and Joachim Leibold, being there for enjoyable conversation during lunch and coffee breaks, of which there were many.

I am thankful to my collaborators, especially Phillip Amrein, without whom the diffusion experiments would have taken aeons to come.

Last but not least many thanks goes to my lovely partner Lena Ziarnetzki who was my biggest support during stressful periods. Also my close family, Karl, Isabella and Merit Bruckmaier helping me relax and reminding me to put my mind of work when necessary.

Bibliography

[1] Davide Castelvecchi. Black hole pictured for first time — in spectacular detail. *Nature*, 568(7752):284–285, April 2019.

[2] Leah Crane. First image of our galaxy's black hole, 2022.

[3] B. P. Abbott, R. Abbott, T. D. Abbott, M. R. Abernathy, F. Acernese, K. Ackley, C. Adams, T. Adams, P. Addesso, R. X. Adhikari, V. B. Adya, C. Affeldt, M. Agathos, K. Agatsuma, N. Aggarwal, O. D. Aguiar, L. Aiello, A. Ain, P. Ajith, B. Allen, A. Allocca, P. A. Altin, S. B. Anderson, W. G. Anderson, K. Arai, M. A. Arain, M. C. Araya, C. C. Arceneaux, J. S. Areeda, N. Arnaud, and Arun et al. Observation of gravitational waves from a binary black hole merger. *Phys. Rev. Lett.*, 116:061102, Feb 2016.

[4] G. Aad, T. Abajyan, B. Abbott, J. Abdallah, S. Abdel Khalek, A.A. Abdelalim, O. Abdinov, R. Aben, B. Abi, M. Abolins, O.S. AbouZeid, H. Abramowicz, H. Abreu, B.S. Acharya, L. Adamczyk, D.L. Adams, T.N. Addy, J. Adelman, S. Adomeit, P. Adragna, T. Adye, and S. Aefsky et al. Observation of a new particle in the search for the standard model higgs boson with the ATLAS detector at the LHC. *Physics Letters B*, 716(1):1–29, September 2012.

[5] Immanuel Koenig, Abdul Qudoos Memon, and Klaus David. Energy consumption of the sensors of smartphones. In *ISWCS 2013; The Tenth International Symposium on Wireless Communication Systems*, pages 1–5, 2013.

[6] I. I. Rabi, J. R. Zacharias, S. Millman, and P. Kusch. A new method of measuring nuclear magnetic moment. *Physical Review*, 53(4):318–318, February 1938.

[7] Russell H Varian. Method and means for correlating nuclear properties of atoms and magnetic fields, US2561490A, 1948.

[8] E. L. Hahn. Spin echoes. *Physical Review*, 80(4):580–594, November 1950.

[9] NMR in Germany, list of NMR-facilities by the Gesellschaft Deutscher Chemiker. `https:\/\/www.gdch.de\/netzwerk-strukturen\/fachstrukturen\/magnetische-\/netzwerke-links\/nmrepr-in-deutschland.html#_c35432`. Accessed: 2022-06-24.

[10] Raluca M. Fratila and Aldrik H. Velders. Small-volume nuclear magnetic resonance spectroscopy. *Annual Review of Analytical Chemistry*, 4(1):227–249, July 2011.

[11] Vlad Badilita, Robert Ch. Meier, Nils Spengler, Ulrike Wallrabe, Marcel Utz, and Jan G. Korvink. Microscale nuclear magnetic resonance: a tool for soft matter research. *Soft Matter*, 8(41):10583, 2012.

[12] Piotr Lepucki, Aleksandr I. Egunov, Marco Rosenkranz, Renato Huber, Alaleh Mirhajivarzaneh, Dmitry D. Karnaushenko, Adam P. Dioguardi, Daniil Karnaushenko, Bernd Büchner, Oliver G. Schmidt, and Hans-Joachim Grafe. Self-assembled rolled-up microcoils for nL microfluidics NMR spectroscopy. *Advanced Materials Technologies*, 6(1):2000679, November 2020.

[13] Marco Grisi, Franck Vincent, Beatrice Volpe, Roberto Guidetti, Nicola Harris, Armin Beck, and Giovanni Boero. NMR spectroscopy of single sub-nl ova with inductive ultra-compact single-chip probes. *Scientific reports*, 7(1):1–8, 2017.

[14] C. L. Degen, F. Reinhard, and P. Cappellaro. Quantum sensing. *Rev. Mod. Phys.*, 89:035002, Jul 2017.

[15] Kristina S Liu, Alex Henning, Markus W Heindl, Robin D Allert, Johannes D Bartl, Ian D Sharp, Roberto Rizzato, and Dominik B Bucher. Surface NMR using quantum sensors in diamond. *Proceedings of the National Academy of Sciences*, 119(5):e2111607119, 2022.

[16] I. Lovchinsky, A. O. Sushkov, E. Urbach, N. P. de Leon, S. Choi, K. De Greve, R. Evans, R. Gertner, E. Bersin, C. Müller, L. McGuinness, F. Jelezko, R. L. Walsworth, H. Park, and M. D. Lukin. Nuclear magnetic resonance detection and spectroscopy of single proteins using quantum logic. *Science*, 351(6275):836–841, 2016.

[17] Christoph Müller, Xi Kong, J-M Cai, K Melentijević, A Stacey, M Markham, D Twitchen, J Isoya, S Pezzagna, J Meijer, et al. Nuclear magnetic resonance spectroscopy with single spin sensitivity. *Nature communications*, 5(1):1–6, 2014.

[18] A. O. Sushkov, I. Lovchinsky, N. Chisholm, R. L. Walsworth, H. Park, and M. D. Lukin. Magnetic resonance detection of individual proton spins using quantum reporters. *Phys. Rev. Lett.*, 113:197601, Nov 2014.

[19] Dominik B Bucher, David R Glenn, Hongkun Park, Mikhail D Lukin, and Ronald L Walsworth. Hyperpolarization-enhanced NMR spectroscopy with femtomole sensitivity using quantum defects in diamond. *Physical Review X*, 10(2):021053, 2020.

[20] Tejas S. Karande, Joo L. Ong, and C. Mauli Agrawal. Diffusion in musculoskeletal tissue engineering scaffolds: Design issues related to porosity, permeability, architecture, and nutrient mixing. *Annals of Biomedical Engineering*, 32(12):1728–1743, December 2004.

[21] Éric Sélard, A Shirazi-Adl, and Jill PG Urban. Finite element study of nutrient diffusion in the human intervertebral disc. *Spine*, 28(17):1945–1953, 2003.

[22] Reynold Spector. Nutrient transport systems in brain: 40 years of progress. *Journal of neurochemistry*, 111(2):315–320, 2009.

[23] Zhenwei Wei, Yangjie Li, R. Graham Cooks, and Xin Yan. Accelerated reaction kinetics in microdroplets: Overview and recent developments. *Annual Review of Physical Chemistry*, 71(1):31–51, April 2020.

[24] Jing Fan, Shuaijun Li, Ziqian Wu, and Zi Chen. Diffusion and mixing in microfluidic devices. In *Microfluidics for Pharmaceutical Applications*, pages 79–100. Elsevier, 2019.

[25] John Preskill. Quantum computing in the NISQ era and beyond. *Quantum*, 2:79, August 2018.

[26] μquans is a vendor for quantum-gravimeters. `https://www.muquans.com/product/absolute-quantum-gravimeter/`. Accessed: 2022-08-05.

[27] Qzabre is a vendor of sacnning tip NV-sensors. `https://qzabre.com`. Accessed: 2022-08-05.

[28] Richard P. Feynman. Quantum mechanical computers. *Foundations of Physics*, 16(6):507–531, June 1986.

[29] R Marx, AF Fahmy, John M Myers, W Bermel, and SJ Glaser. Realization of a 5-bit NMR quantum computer using a new molecular architecture. *arXiv preprint quant-ph/9905087*, 1999.

[30] CH Tseng, S Somaroo, Y Sharf, Emanuel Knill, Raymond Laflamme, Timothy F Havel, and David G Cory. Quantum simulation of a three-body-interaction Hamiltonian on an NMR quantum computer. *Physical Review A*, 61(1):012302, 1999.

[31] David P. DiVincenzo. The physical implementation of quantum computation. *Fortschritte der Physik*, 48(9-11):771–783, September 2000.

[32] Walther Gerlach and Otto Stern. Der experimentelle Nachweis der Richtungsquantelung im Magnetfeld. *Zeitschrift für Physik*, 9(1):349–352, December 1922.

[33] Marlan O. Scully and M. Suhail Zubairy. *Quantum Optics*. Cambridge University Press, September 1997.

[34] Frank A.L. Anet, Daniel J. OĹeary, Charles G. Wade, and Robert D. Johnson. NMR relaxation by the antisymmetric component of the shielding tensor: a longer transverse than longitudinal relaxation time. *Chemical Physics Letters*, 171(5-6):401–405, August 1990.

[35] P. Grodzinski. The history of diamond polishing. *Transactions of the Newcomen Society*, 28(1):203–205, January 1951.

[36] K. Nassau and J. Nassau. The history and present status of synthetic diamond. *Journal of Crystal Growth*, 46(2):157–172, February 1979.

[37] Rudolf Gross and Achim Marx. *Festkörperphysik*. Oldenbourg Wissenschaftsverlag Verlag, 2012.

[38] Graphitization of diamond at zero pressure and at a high pressure. *Proceedings of the Royal Society of London. A. Mathematical and Physical Sciences*, 328(1574):413–427, June 1972.

[39] Lanhua Wei, P. K. Kuo, R. L. Thomas, T. R. Anthony, and W. F. Banholzer. Thermal conductivity of isotopically modified single crystal diamond. *Phys. Rev. Lett.*, 70:3764–3767, Jun 1993.

[40] MR Salehpour and S Satpathy. Comparison of electron bands of hexagonal and cubic diamond. *Physical Review B*, 41(5):3048, 1990.

[41] I Aharonovich, S Castelletto, D A Simpson, C-H Su, A D Greentree, and S Prawer. Diamond-based single-photon emitters. *Reports on Progress in Physics*, 74(7):076501, June 2011.

[42] Sébastien Pezzagna and Jan Meijer. Quantum computer based on color centers in diamond. *Applied Physics Reviews*, 8(1):011308, March 2021.

[43] John F. Barry, Jennifer M. Schloss, Erik Bauch, Matthew J. Turner, Connor A. Hart, Linh M. Pham, and Ronald L. Walsworth. Sensitivity optimization for NV-diamond magnetometry. *Rev. Mod. Phys.*, 92:015004, Mar 2020.

[44] Dominik B. Bucher, Diana P. L. Aude Craik, Mikael P. Backlund, Matthew J. Turner, Oren Ben Dor, David R. Glenn, and Ronald L. Walsworth. Quantum diamond spectrometer for nanoscale NMR and ESR spectroscopy. *Nature Protocols*, 14(9):2707–2747, September 2019.

[45] Marcus W. Doherty, Neil B. Manson, Paul Delaney, Fedor Jelezko, Jörg Wrachtrup, and Lloyd C.L. Hollenberg. The nitrogen-vacancy colour centre in diamond. *Physics Reports*, 528(1):1–45, July 2013.

[46] F. Jelezko and J. Wrachtrup. Single defect centres in diamond: A review. *physica status solidi (a)*, 203(13):3207–3225, October 2006.

[47] M. W. Doherty, F. Dolde, H. Fedder, F. Jelezko, J. Wrachtrup, N. B. Manson, and L. C. L. Hollenberg. Theory of the ground-state spin of the NV^- center in diamond. *Phys. Rev. B*, 85:205203, May 2012.

[48] Robin D Allert, Karl D Briegel, and Dominik B Bucher. Advances in nano-and microscale NMR spectroscopy using diamond quantum sensors. *Chemical Communications*, 58(59):8165–8181, 2022.

[49] Jason M. Smith, Simon A. Meynell, Ania C. Bleszynski Jayich, and Jan Meijer. Colour centre generation in diamond for quantum technologies. *Nanophotonics*, 8(11):1889–1906, November 2019.

[50] Christopher M Breeding and James E Shigley. The "type" classification system of diamonds and its importance in gemology. *Gems & Gemology*, 45(2):96–111, 2009.

[51] Carlo Bradac, Weibo Gao, Jacopo Forneris, Matthew E. Trusheim, and Igor Aharonovich. Quantum nanophotonics with group IV defects in diamond. *Nature Communications*, 10(1), December 2019.

[52] Mathias H. Metsch, Katharina Senkalla, Benedikt Tratzmiller, Jochen Scheuer, Michael Kern, Jocelyn Achard, Alexandre Tallaire, Martin B. Plenio, Petr Siyushev, and Fedor Jelezko. Initialization and readout of nuclear spins via a negatively charged silicon-vacancy center in diamond. *Physical Review Letters*, 122(19), May 2019.

[53] V. A. Nadolinny, A. Yu. Komarovskikh, Yu. N. Palyanov, I. N. Kupriyanov, Yu. M. Borzdov, M. I. Rakhmanova, O. P. Yuryeva, and S. L. Veber. EPR study of germanium-vacancy defects in diamonds. *Journal of Structural Chemistry*, 57(5):1041–1043, September 2016.

[54] Takayuki Iwasaki, Yoshiyuki Miyamoto, Takashi Taniguchi, Petr Siyushev, Mathias H.

Metsch, Fedor Jelezko, and Mutsuko Hatano. Tin-vacancy quantum emitters in diamond. *Phys. Rev. Lett.*, 119:253601, Dec 2017.

[55] S. Ditalia Tchernij, T. Lühmann, T. Herzig, J. Küpper, A. Damin, S. Santonocito, M. Signorile, P. Traina, E. Moreva, F. Celegato, S. Pezzagna, I. P. Degiovanni, P. Olivero, M. Jakšić, J. Meijer, P. M. Genovese, and J. Forneris. Single-photon emitters in lead-implanted single-crystal diamond. *ACS Photonics*, 5(12):4864–4871, November 2018.

[56] Optical studies of the 1.945 eV vibronic band in diamond. *Proceedings of the Royal Society of London. A. Mathematical and Physical Sciences*, 348(1653):285–298, February 1976.

[57] G. D. Fuchs, V. V. Dobrovitski, R. Hanson, A. Batra, C. D. Weis, T. Schenkel, and D. D. Awschalom. Excited-state spectroscopy using single spin manipulation in diamond. *Phys. Rev. Lett.*, 101:117601, Sep 2008.

[58] Ádám Gali. Ab initio theory of the nitrogen-vacancy center in diamond. *Nanophotonics*, 8(11):1907–1943, September 2019.

[59] J H N Loubser and J A van Wyk. Electron spin resonance in the study of diamond. *Reports on Progress in Physics*, 41(8):1201–1248, August 1978.

[60] NIST value for the electron gyromagnetic ratio. `https://physics.nist.gov/cgi-bin/cuu/Value?gammae`. Accessed: 2022-06-29.

[61] S. Felton, A. M. Edmonds, M. E. Newton, P. M. Martineau, D. Fisher, D. J. Twitchen, and J. M. Baker. Hyperfine interaction in the ground state of the negatively charged nitrogen vacancy center in diamond. *Phys. Rev. B*, 79:075203, Feb 2009.

[62] L J Rogers, M W Doherty, M S J Barson, S Onoda, T Ohshima, and N B Manson. Singlet levels of th NV- centre in diamond. *New Journal of Physics*, 17(1):013048, January 2015.

[63] N. B. Manson, J. P. Harrison, and M. J. Sellars. Nitrogen-vacancy center in diamond: Model of the electronic structure and associated dynamics. *Phys. Rev. B*, 74:104303, Sep 2006.

[64] V. M. Acosta, A. Jarmola, E. Bauch, and D. Budker. Optical properties of the nitrogen-vacancy singlet levels in diamond. *Physical Review B*, 82(20), November 2010.

[65] Lucio Robledo, Hannes Bernien, Toeno van der Sar, and Ronald Hanson. Spin dynamics in the optical cycle of single nitrogen-vacancy centres in diamond. *New Journal of Physics*, 13(2):025013, February 2011.

[66] Florian M. Hrubesch, Georg Braunbeck, Martin Stutzmann, Friedemann Reinhard, and Martin S. Brandt. Efficient electrical spin readout of nv^- centers in diamond. *Phys. Rev. Lett.*, 118:037601, Jan 2017.

[67] Michal Gulka, Daniel Wirtitsch, Viktor Ivády, Jelle Vodnik, Jaroslav Hruby, Goele Magchiels, Emilie Bourgeois, Adam Gali, Michael Trupke, and Milos Nesladek. Room-temperature control and electrical readout of individual nitrogen-vacancy nuclear spins. *Nature Communications*, 12(1), July 2021.

[68] Philipp J Vetter, Alastair Marshall, Genko T Genov, Tim F Weiss, Nico Striegler, Eva F Großmann, Santiago Oviedo-Casado, Javier Cerrillo, Javier Prior, Philipp Neumann, et al. Zero- and low-field sensing with nitrogen-vacancy centers. *Physical Review Applied*, 17(4):044028, 2022.

[69] Masazumi Fujiwara and Yutaka Shikano. Diamond quantum thermometry: from foundations to applications. *Nanotechnology*, 32(48):482002, September 2021.

[70] Chu-Feng Liu, Weng-Hang Leong, Kangwei Xia, Xi Feng, Amit Finkler, Andrej Denisenko, Jörg Wrachtrup, Quan Li, and Ren-Bao Liu. Ultra-sensitive hybrid diamond nanothermometer. *National Science Review*, 8(5), August 2020.

[71] V. M. Acosta, E. Bauch, M. P. Ledbetter, A. Waxman, L.-S. Bouchard, and D. Budker. Temperature dependence of the nitrogen-vacancy magnetic resonance in diamond. *Phys. Rev. Lett.*, 104:070801, Feb 2010.

[72] Paolo Andrich, Jiajing Li, Xiaoying Liu, F. Joseph Heremans, Paul F. Nealey, and David D. Awschalom. Microscale-resolution thermal mapping using a flexible platform of patterned quantum sensors. *Nano Letters*, 18(8):4684–4690, July 2018.

[73] Yushi Nishimura, Keisuke Oshimi, Yumi Umehara, Yuka Kumon, Kazu Miyaji, Hiroshi Yukawa, Yutaka Shikano, Tsutomu Matsubara, Masazumi Fujiwara, Yoshinobu Baba, and Yoshio Teki. Wide-field fluorescent nanodiamond spin measurements toward real-time large-area intracellular thermometry. *Scientific Reports*, 11(1), February 2021.

[74] G. Kucsko, P. C. Maurer, N. Y. Yao, M. Kubo, H. J. Noh, P. K. Lo, H. Park, and M. D. Lukin. Nanometre-scale thermometry in a living cell. *Nature*, 500(7460):54–58, July 2013.

[75] Vladimir V. Soshenko, Stepan V. Bolshedvorskii, Olga Rubinas, Vadim N. Sorokin, Andrey N. Smolyaninov, Vadim V. Vorobyov, and Alexey V. Akimov. Nuclear spin gyroscope based on the nitrogen vacancy center in diamond. *Phys. Rev. Lett.*, 126:197702, May 2021.

[76] Edlyn V. Levine, Matthew J. Turner, Pauli Kehayias, Connor A. Hart, Nicholas Langellier, Raisa Trubko, David R. Glenn, Roger R. Fu, and Ronald L. Walsworth. Principles and techniques of the quantum diamond microscope. *Nanophotonics*, 8(11):1945–1973, September 2019.

[77] Matthew J. Turner, Nicholas Langellier, Rachel Bainbridge, Dan Walters, Srujan Meesala, Thomas M. Babinec, Pauli Kehayias, Amir Yacoby, Evelyn Hu, Marko Lončar, Ronald L. Walsworth, and Edlyn V. Levine. Magnetic field fingerprinting of integrated-circuit activity with a quantum diamond microscope. *Phys. Rev. Applied*, 14:014097, Jul 2020.

[78] P. Kehayias, E. V. Levine, L. Basso, J. Henshaw, M. Saleh Ziabari, M. Titze, R. Haltli, J. Okoro, D. R. Tibbetts, D. M. Udoni, E. Bielejec, M. P. Lilly, T.-M. Lu, P. D. D. Schwindt, and A. M. Mounce. Measurement and simulation of the magnetic fields from a 555 timer integrated circuit using a quantum diamond microscope and finite-element analysis. *Phys. Rev. Applied*, 17:014021, Jan 2022.

[79] Jean-Philippe Tetienne, Nikolai Dontschuk, David A. Broadway, Alastair Stacey, David A. Simpson, and Lloyd C. L. Hollenberg. Quantum imaging of current flow in graphene. *Science Advances*, 3(4), April 2017.

[80] Alec Jenkins, Matthew Pelliccione, Guoqiang Yu, Xin Ma, Xiaoqin Li, Kang L. Wang, and Ania C. Bleszynski Jayich. Single-spin sensing of domain-wall structure and dynamics in a thin-film skyrmion host. *Physical Review Materials*, 3(8), August 2019.

[81] A. Dussaux, P. Schoenherr, K. Koumpouras, J. Chico, K. Chang, L. Lorenzelli, N. Kanazawa, Y. Tokura, M. Garst, A. Bergman, C. L. Degen, and D. Meier. Local dynamics of topological magnetic defects in the itinerant helimagnet FeGe. *Nature Communications*, 7(1), August 2016.

[82] P. Welter, J. Rhensius, A. Morales, M. S. Wörnle, C.-H. Lambert, G. Puebla-Hellmann, P. Gambardella, and C. L. Degen. Scanning nitrogen-vacancy center magnetometry in large in-plane magnetic fields. *Applied Physics Letters*, 120(7):074003, February 2022.

[83] L. Rondin, J. P. Tetienne, S. Rohart, A. Thiaville, T. Hingant, P. Spinicelli, J. F. Roch, and V. Jacques. Stray-field imaging of magnetic vortices with a single diamond spin. *Nature Communications*, 4(1):2279, July 2013.

[84] Dominik Schmid-Lorch, Thomas Häberle, Friedemann Reinhard, Andrea Zappe, Michael Slota, Lapo Bogani, Amit Finkler, and Jörg Wrachtrup. Relaxometry and dephasing imaging of superparamagnetic magnetite nanoparticles using a single qubit. *Nano Letters*, 15(8):4942–4947, July 2015.

[85] Felipe Perona Martínez, Anggrek Citra Nusantara, Mayeul Chipaux, Sandeep Kumar Padamati, and Romana Schirhagl. Nanodiamond relaxometry-based detection of free-radical species when produced in chemical reactions in biologically relevant conditions. *ACS Sensors*, 5(12):3862–3869, December 2020.

[86] Fabian A. Freire-Moschovitis, Roberto Rizzato, Anton Pershin, Moritz R. Schepp, Robin D.

Allert, Lina Todenhagen, Martin S. Brandt, Adam Gali, and Dominik B. Bucher. Diamagnetic electrolytes reduce surface noise at near-surface spin defects in diamond. Manuscript submitted for publication.

[87] David R. Glenn, Dominik B. Bucher, Junghyun Lee, Mikhail D. Lukin, Hongkun Park, and Ronald L. Walsworth. High-resolution magnetic resonance spectroscopy using a solid-state spin sensor. *Nature*, 555(7696):351–354, March 2018.

[88] Fleming Bruckmaier, Karl D. Briegel, and Dominik B. Bucher. Geometry dependence of micron-scale NMR signals on NV-diamond chips. *Journal of Magnetic Resonance Open*, 8-9:100023, December 2021.

[89] H. J. Mamin, M. Kim, M. H. Sherwood, C. T. Rettner, K. Ohno, D. D. Awschalom, and D. Rugar. Nanoscale nuclear magnetic resonance with a nitrogen-vacancy spin sensor. *Science*, 339(6119):557–560, January 2013.

[90] Carlos A. Meriles, Liang Jiang, Garry Goldstein, Jonathan S. Hodges, Jeronimo Maze, Mikhail D. Lukin, and Paola Cappellaro. Imaging mesoscopic nuclear spin noise with a diamond magnetometer. *The Journal of Chemical Physics*, 133(12):124105, 2010.

[91] Daniel Abrams, Matthew E Trusheim, Dirk R Englund, Mark D Shattuck, and Carlos A Meriles. Dynamic nuclear spin polarization of liquids and gases in contact with nanostructured diamond. *Nano letters*, 14(5):2471–2478, 2014.

[92] Paul T. Callaghan. *Translational Dynamics and Magnetic Resonance*. Oxford University Press, September 2011.

[93] B. E. Herzog, D. Cadeddu, F. Xue, P. Peddibhotla, and M. Poggio. Boundary between the thermal and statistical polarization regimes in a nuclear spin ensemble. *Applied Physics Letters*, 105(4):043112, July 2014.

[94] OW Sørensen. *James Keeler: Understanding NMR Spectroscopy*. Wiley Online Library, 2006.

[95] T. Staudacher, F. Shi, S. Pezzagna, J. Meijer, J. Du, C. A. Meriles, F. Reinhard, and J. Wrachtrup. Nuclear magnetic resonance spectroscopy on a (5-nanometer)3 sample volume. *Science*, 339(6119):561–563, 2013.

[96] F. A. L. Anet and A. J. R. Bourn. Nuclear magnetic resonance spectral assignments from nuclear overhauser effect. *Journal of the American Chemical Society*, 87(22):5250–5251, November 1965.

[97] Nithya Arunkumar, Dominik B. Bucher, Matthew J. Turner, Patrick TomHon, David Glenn, Sören Lehmkuhl, Mikhail D. Lukin, Hongkun Park, Matthew S. Rosen, Thomas Theis, and Ronald L. Walsworth. Micron-scale NV-NMR spectroscopy with signal amplification by reversible exchange. *PRX Quantum*, 2:010305, Jan 2021.

[98] R Rizzato, F Bruckmaier, KS Liu, SJ Glaser, and DB Bucher. Polarization transfer from optically pumped ensembles of N-V centers to multinuclear spin baths. *Physical Review Applied*, 17(2):024067, 2022.

[99] A.J. Healey, L.T. Hall, G.A.L. White, T. Teraji, M.-A. Sani, F. Separovic, J.-P. Tetienne, and L.C.L. Hollenberg. Polarization transfer to external nuclear spins using ensembles of nitrogen-vacancy centers. *Phys. Rev. Applied*, 15:054052, May 2021.

[100] David A Broadway, Jean-Philippe Tetienne, Alastair Stacey, James DA Wood, David A Simpson, Liam T Hall, and Lloyd CL Hollenberg. Quantum probe hyperpolarisation of molecular nuclear spins. *Nature communications*, 9(1):1–8, 2018.

[101] Friedemann Reinhard. Nanoscale sensing and quantum coherence. *Nanoscale Quantum Optics*, 204:145, 2020.

[102] H. Y. Carr and E. M. Purcell. Effects of diffusion on free precession in nuclear magnetic resonance experiments. *Phys. Rev.*, 94:630–638, May 1954.

[103] Shlomi Kotler, Nitzan Akerman, Yinnon Glickman, and Roee Ozeri. Nonlinear single-spin spectrum analyzer. *Phys. Rev. Lett.*, 110:110503, Mar 2013.

[104] Terry Gullion, David B Baker, and Mark S Conradi. New, compensated carr-purcell sequences. *Journal of Magnetic Resonance (1969)*, 89(3):479–484, October 1990.

[105] Zhenyu Wang, Jorge Casanova, and Martin B. Plenio. Enhancing the robustness of dynamical decoupling sequences with correlated random phases. *Symmetry*, 12(5):730, May 2020.

[106] Genko T. Genov, Daniel Schraft, Nikolay V. Vitanov, and Thomas Halfmann. Arbitrarily accurate pulse sequences for robust dynamical decoupling. *Phys. Rev. Lett.*, 118:133202, Mar 2017.

[107] Joonhee Choi, Hengyun Zhou, Helena S. Knowles, Renate Landig, Soonwon Choi, and Mikhail D. Lukin. Robust dynamic Hamiltonian engineering of many-body spin systems. *Phys. Rev. X*, 10:031002, Jul 2020.

[108] Nithya Arunkumar, Kevin S Olsson, Jner Tzern Oon, Connor Hart, Dominik B Bucher, David Glenn, Mikhail D Lukin, Hongkun Park, Donhee Ham, and Ronald L Walsworth. Quantum logic enhanced sensing in solid-state spin ensembles. *arXiv preprint arXiv:2203.12501*, 2022.

[109] Abdelghani Laraoui, Florian Dolde, Christian Burk, Friedemann Reinhard, Jörg Wrachtrup, and Carlos A. Meriles. High-resolution correlation spectroscopy of 13c spins near a nitrogen-vacancy centre in diamond. *Nature Communications*, 4(1), April 2013.

[110] Simon Schmitt, Tuvia Gefen, Felix M. Stürner, Thomas Unden, Gerhard Wolff, Christoph Müller, Jochen Scheuer, Boris Naydenov, Matthew Markham, Sebastien Pezzagna, Jan Meijer, Ilai Schwarz, Martin Plenio, Alex Retzker, Liam P. McGuinness, and Fedor Jelezko. Submillihertz magnetic spectroscopy performed with a nanoscale quantum sensor. *Science*, 356(6340):832–837, May 2017.

[111] Chen Zhang, Durga Dasari, Matthias Widmann, Jonas Meinel, Vadim Vorobyov, Polina Kapitanova, Elizaveta Nenasheva, Kazuo Nakamura, Hitoshi Sumiya, Shinobu Onoda, et al.

Quantum-assisted distortion-free audio signal sensing. *Nature communications*, 13(1):1–10, 2022.

[112] J. M. Boss, K. S. Cujia, J. Zopes, and C. L. Degen. Quantum sensing with arbitrary frequency resolution. *Science*, 356(6340):837–840, May 2017.

[113] Liang Jiang, JS Hodges, JR Maze, Peter Maurer, JM Taylor, DG Cory, PR Hemmer, Ronald Lee Walsworth, Amir Yacoby, Alexander S Zibrov, et al. Repetitive readout of a single electronic spin via quantum logic with nuclear spin ancillae. *Science*, 326(5950):267–272, 2009.

[114] Nabeel Aslam, Matthias Pfender, Philipp Neumann, Rolf Reuter, Andrea Zappe, Felipe Fávaro de Oliveira, Andrej Denisenko, Hitoshi Sumiya, Shinobu Onoda, Junichi Isoya, et al. Nanoscale nuclear magnetic resonance with chemical resolution. *Science*, 357(6346):67–71, 2017.

[115] NIST value for the proton gyromagnetic ratio. `https://physics.nist.gov/cgi-bin/cuu/Value?gammap`. Accessed: 2022-07-11.

[116] C Munuera-Javaloy, A Tobalina, and J Casanova. High-resolution NMR spectroscopy at large fields with nitrogen vacancy centers. *arXiv preprint arXiv:2205.04150*, 2022.

[117] Guoqing Wang, Yi-Xiang Liu, Jennifer M. Schloss, Scott T. Alsid, Danielle A. Braje, and Paola Cappellaro. Sensing of arbitrary-frequency fields using a quantum mixer. *Phys. Rev. X*, 12:021061, Jun 2022.

[118] Jonas Meinel, Vadim Vorobyov, Boris Yavkin, Durga Dasari, Hitoshi Sumiya, Shinobu Onoda, Junichi Isoya, and Jörg Wrachtrup. Heterodyne sensing of microwaves with a quantum sensor. *Nature Communications*, 12(1), May 2021.

[119] Jonas Meinel, Minsik Kwon, Durga Dasari, Hitoshi Sumiya, Shinobu Onoda, Junichi Isoya, Vadim Vorobyov, and Jörg Wrachtrup. Quantum heterodyne sensing of nuclear spins via double resonance. *arXiv preprint arXiv:2205.10182*, 2022.

[120] Lilian Childress and Jean McIntyre. Multifrequency spin resonance in diamond. *Phys. Rev. A*, 82:033839, Sep 2010.

[121] Gwendolyn N. Chmurny and David I. Hoult. The ancient and honourable art of shimming. *Concepts in Magnetic Resonance*, 2(3):131–149, July 1990.

[122] S. Ashhab, J. R. Johansson, A. M. Zagoskin, and Franco Nori. Two-level systems driven by large-amplitude fields. *Phys. Rev. A*, 75:063414, Jun 2007.

[123] Zhecheng Wang, Fei Kong, Pengju Zhao, Zhehua Huang, Pei Yu, Ya Wang, Fazhan Shi, and Jiangfeng Du. Picotesla magnetometry of microwave fields with diamond sensors. *Science advances*, 8(31):eabq8158, 2022.

[124] Paul Räcke, Daniel Spemann, Jürgen W. Gerlach, Bernd Rauschenbach, and Jan Meijer. Detection of small bunches of ions using image charges. *Scientific Reports*, 8(1), June 2018.

[125] W. Schnitzler, N. M. Linke, R. Fickler, J. Meijer, F. Schmidt-Kaler, and K. Singer. Deterministic ultracold ion source targeting the heisenberg limit. *Physical Review Letters*, 102(7), February 2009.

[126] D. N. Jamieson, C. Yang, T. Hopf, S. M. Hearne, C. I. Pakes, S. Prawer, M. Mitic, E. Gauja, S. E. Andresen, F. E. Hudson, A. S. Dzurak, and R. G. Clark. Controlled shallow single-ion implantation in silicon using an active substrate for sub-20-keV ions. *Applied Physics Letters*, 86(20):202101, May 2005.

[127] Takahiro Shinada, Shintaro Okamoto, Takahiro Kobayashi, and Iwao Ohdomari. Enhancing semiconductor device performance using ordered dopant arrays. *Nature*, 437(7062):1128–1131, October 2005.

[128] J. O. Orwa, C. Santori, K. M. C. Fu, B. Gibson, D. Simpson, I. Aharonovich, A. Stacey, A. Cimmino, P. Balog, M. Markham, D. Twitchen, A. D. Greentree, R. G. Beausoleil, and S. Prawer. Engineering of nitrogen-vacancy color centers in high purity diamond by ion implantation and annealing. *Journal of Applied Physics*, 109(8):083530, 2011.

[129] Kenichi Ohno, F. Joseph Heremans, Lee C. Bassett, Bryan A. Myers, David M. Toyli, Ania C. Bleszynski Jayich, Christopher J. Palmstrøm, and David D. Awschalom. Engineering shallow spins in diamond with nitrogen delta-doping. *Applied Physics Letters*, 101(8):082413, August 2012.

[130] Mouzhe Xie, Xiaofei Yu, Lila V. H. Rodgers, Daohong Xu, Ignacio Chi-Durán, Adrien Toros, Niels Quack, Nathalie P. de Leon, and Peter C. Maurer. Biocompatible surface functionalization architecture for a diamond quantum sensor. *Proceedings of the National Academy of Sciences*, 119(8):e2114186119, 2022.

[131] John M Abendroth, Konstantin Herb, Erika Janitz, Tianqi Zhu, Laura A Völker, and Christian L Degen. Single nitrogen-vacancy-NMR of amine-functionalized diamond surfaces. *arXiv preprint arXiv:2202.03969*, 2022.

[132] Eisuke Abe and Kento Sasaki. Tutorial: Magnetic resonance with nitrogen-vacancy centers in diamond—microwave engineering, materials science, and magnetometry. *Journal of Applied Physics*, 123(16):161101, 2018.

[133] Stephen J. DeVience, Linh M. Pham, Igor Lovchinsky, Alexander O. Sushkov, Nir Bar-Gill, Chinmay Belthangady, Francesco Casola, Madeleine Corbett, Huiliang Zhang, Mikhail Lukin, Hongkun Park, Amir Yacoby, and Ronald L. Walsworth. Nanoscale NMR spectroscopy and imaging of multiple nuclear species. *Nature Nanotechnology*, 10(2):129–134, January 2015.

[134] F. Ziem, M. Garsi, H. Fedder, and J. Wrachtrup. Quantitative nanoscale MRI with a wide field of view. *Scientific Reports*, 9(1), August 2019.

[135] P. Kehayias, A. Jarmola, N. Mosavian, I. Fescenko, F. M. Benito, A. Laraoui, J. Smits, L. Bougas, D. Budker, A. Neumann, S. R. J. Brueck, and V. M. Acosta. Solution nuclear magnetic resonance spectroscopy on a nanostructured diamond chip. *Nature Communications*, 8(1), August 2017.

[136] Janis Smits, Joshua T. Damron, Pauli Kehayias, Andrew F. McDowell, Nazanin Mosavian, Ilja Fescenko, Nathaniel Ristoff, Abdelghani Laraoui, Andrey Jarmola, and Victor M. Acosta. Two-dimensional nuclear magnetic resonance spectroscopy with a microfluidic diamond quantum sensor. *Science Advances*, 5(7):eaaw7895, 2019.

[137] Keisuke Oshimi, Yushi Nishimura, Tsutomu Matsubara, Masuaki Tanaka, Eiji Shikoh, Li Zhao, Yajuan Zou, Naoki Komatsu, Yuta Ikado, Yuka Takezawa, Eriko Kage-Nakadai, Yumi Izutsu, Katsutoshi Yoshizato, Saho Morita, Masato Tokunaga, Hiroshi Yukawa, Yoshinobu Baba, Yoshio Teki, and Masazumi Fujiwara. Glass-patternable notch-shaped microwave architecture for on-chip spin detection in biological samples. *Lab on a Chip*, 22(13):2519–2530, 2022.

[138] Robin D Allert, Fleming Bruckmaier, Nick R Neuling, Fabian A Freire-Moschovitis, Kristina S Liu, Claudia Schrepel, Philip Schätzle, Peter Knittel, Martin Hermans, and Dominik B Bucher. Microfluidic quantum sensing platform for lab-on-a-chip applications. *arXiv preprint arXiv:2209.01651*, 2022.

[139] N. Neuling and D. B. Bucher. Single cell NMR using quantum sensors in diamond. Manuscript in preperation.

[140] Alain Vlassenbroek, Jean Jeener, and Paul Broekaert. Macroscopic and microscopic fields in high-resolution liquid NMR. *Journal of Magnetic Resonance, Series A*, 118(2):234–246, 1996.

[141] Wei Dong and CA Meriles. Indirect detection of NMR via geometry-dependent dipolar fields, revisited. *Journal of Magnetic Resonance*, 186(2):330–336, 2007.

[142] Sujatha Vathyam, Sanghyuk Lee, and Warren S Warren. Homogeneous NMR spectra in inhomogeneous fields. *Science*, 272(5258):92–96, 1996.

[143] R Bowtell, S Gutteridge, and C Ramanathan. Imaging the long-range dipolar field in structured liquid state samples. *Journal of Magnetic Resonance*, 150(2):147–155, 2001.

[144] D.I Hoult and R.E Richards. The signal-to-noise ratio of the nuclear magnetic resonance experiment. *Journal of Magnetic Resonance (1969)*, 24(1):71–85, October 1976.

[145] Josef Granwehr, Jeffry T Urban, Andreas H Trabesinger, and Alexander Pines. NMR detection using laser-polarized xenon as a dipolar sensor. *Journal of Magnetic Resonance*, 176(2):125–139, 2005.

[146] Malcolm H Levitt. Demagnetization field effects in two-dimensional solution NMR. *Concepts in Magnetic Resonance*, 8(2):77–103, 1996.

[147] James F. Gillooly, Andrew Hein, and Rachel Damiani. Nuclear DNA content varies with cell size across human cell types. *Cold Spring Harbor Perspectives in Biology*, 7(7):a019091, July 2015.

[148] Bernard T. Kelly, Jean-Christophe Baret, Valerie Taly, and Andrew D. Griffiths. Miniaturizing chemistry and biology in microdroplets. *Chemical Communications*, (18):1773, 2007.

[149] H. Gudbjartsson and S. Patz. NMR diffusion simulation based on conditional random walk. *IEEE Transactions on Medical Imaging*, 14(4):636–642, 1995.

[150] Dmitry Budker and Michael Romalis. Optical magnetometry. *Nature Physics*, 3(4):227–234, apr 2007.

[151] L Rondin, J-P Tetienne, T Hingant, J-F Roch, P Maletinsky, and V Jacques. Magnetometry with nitrogen-vacancy defects in diamond. *Reports on Progress in Physics*, 77(5):056503, may 2014.

[152] A. Dréau, M. Lesik, L. Rondin, P. Spinicelli, O. Arcizet, J.-F. Roch, and V. Jacques. Avoiding power broadening in optically detected magnetic resonance of single NV defects for enhanced dc magnetic field sensitivity. *Phys. Rev. B*, 84:195204, Nov 2011.

[153] J. M. Taylor, P. Cappellaro, L. Childress, L. Jiang, D. Budker, P. R. Hemmer, A. Yacoby,

R. Walsworth, and M. D. Lukin. High-sensitivity diamond magnetometer with nanoscale resolution. *Nature Physics*, 4(10):810–816, sep 2008.

[154] B. J. Shields, Q. P. Unterreithmeier, N. P. de Leon, H. Park, and M. D. Lukin. Efficient readout of a single spin state in diamond via spin-to-charge conversion. *Phys. Rev. Lett.*, 114:136402, Mar 2015.

[155] Spec sheet for G&H AOM. `https://gandh.com`. Accessed: 2022-08-25.

[156] Jens Gottmann, Martin Hermans, Nikolai Repiev, and Jürgen Ortmann. Selective laser-induced etching of 3d precision quartz glass components for microfluidic applications—up-scaling of complexity and speed. *Micromachines*, 8(4), 2017.

[157] F. Bruckmaier, R. Allert, N. Neuling, P. Amrein, S. Littin, M. Zaitsev, and D. B. Bucher. Spatially resolved PGSE diffusion measurements on the micro-scale using diamond based quantum sensors. Manuscript in preperation.

[158] P. Amrein, F. Bruckmaier, S. Littin, D. B. Bucher, and M. Zaitsev. Design and fabrication of gradient coils for NV-NMR. Manuscript in preperation.

[159] E. O. Stejskal and J. E. Tanner. Spin diffusion measurements: Spin echoes in the presence of a time-dependent field gradient. *The Journal of Chemical Physics*, 42(1):288–292, January 1965.

[160] J. E. Tanner and E. O. Stejskal. Restricted self-diffusion of protons in colloidal systems by the pulsed-gradient, spin-echo method. *The Journal of Chemical Physics*, 49(4):1768–1777, August 1968.

[161] Filip Szczepankiewicz, Carl-Fredrik Westin, and Markus Nilsson. Gradient waveform design for tensor-valued encoding in diffusion MRI. *Journal of Neuroscience Methods*, 348:109007, January 2021.

[162] Davy Sinnaeve. The stejskal-tanner equation generalized for any gradient shape-an

overview of most pulse sequences measuring free diffusion. *Concepts in Magnetic Resonance Part A*, 40A(2):39–65, March 2012.

[163] R. Mills. Self-diffusion in normal and heavy water in the range 1-45.deg. *The Journal of Physical Chemistry*, 77(5):685–688, March 1973.

[164] Kenneth R. Harris and Lawrence A. Woolf. Pressure and temperature dependence of the self diffusion coefficient of water and oxygen-18 water. *Journal of the Chemical Society, Faraday Transactions 1: Physical Chemistry in Condensed Phases*, 76(0):377, 1980.

[165] P.S. Tofts, D. Lloyd, C.A. Clark, G.J. Barker, G.J.M. Parker, P. McConville, C. Baldock, and J.M. Pope. Test liquids for quantitative MRI measurements of self-diffusion coefficient in vivo. *Magnetic Resonance in Medicine*, 43(3):368–374, March 2000.

[166] A. Kusumi, Y. Sako, and M. Yamamoto. Confined lateral diffusion of membrane receptors as studied by single particle tracking (nanovid microscopy). effects of calcium-induced differentiation in cultured epithelial cells. *Biophysical Journal*, 65(5):2021–2040, November 1993.

[167] Friedrich Wagner, Frederik B. Laun, Tristan A. Kuder, Anna Mlynarska, Florian Maier, Jonas Faust, Kerstin Demberg, Linus Lindemann, Boris Rivkin, Armin M. Nagel, Mark E. Ladd, Klaus Maier-Hein, Sebastian Bickelhaupt, and Michael Bach. Temperature and concentration calibration of aqueous polyvinylpyrrolidone (PVP) solutions for isotropic diffusion MRI phantoms. *PLOS ONE*, 12(6):e0179276, June 2017.

[168] Ghoncheh Amouzandeh, Thomas L. Chenevert, Scott D. Swanson, Brian D. Ross, and Dariya I. Malyarenko. Technical note: Temperature and concentration dependence of water diffusion in polyvinylpyrrolidone solutions. *Medical Physics*, 49(5):3325–3332, March 2022.

[169] David J.T. Hill, Andrew K. Whittaker, and Zainuddin. Water diffusion into radiation crosslinked PVA–PVP network hydrogels. *Radiation Physics and Chemistry*, 80(2):213–218, February 2011.

[170] Quantum sensing market evaluation. `https://www.prnewswire.com/news-releases/global-quantum-sensors-market-evolution-report-2022.-2031-featuring.bosch-coldquanta-element-6-honeywell-m-squared-lasers-muquans-nist.-qlm-qzabre--single-quantum-301551905.html`. Accessed: 2022-08-05.

[171] Simon Schmitt. *Nanoscale magnetic spectroscopy with colour centres in diamond*. Dissertation, University of Ulm, 2020.

[172] I. Solomon. Relaxation processes in a system of two spins. *Phys. Rev.*, 99:559–565, Jul 1955.

[173] Linh M. Pham, Stephen J. DeVience, Francesco Casola, Igor Lovchinsky, Alexander O. Sushkov, Eric Bersin, Junghyun Lee, Elana Urbach, Paola Cappellaro, Hongkun Park, Amir Yacoby, Mikhail Lukin, and Ronald L. Walsworth. NMR technique for determining the depth of shallow nitrogen-vacancy centers in diamond. *Phys. Rev. B*, 93:045425, Jan 2016.

[174] Inga A Dobrinets, Victor G Vins, and Alexander M Zaitsev. *HPHT-treated diamonds*. Springer, 2016.

[175] Ulrika FS D'Haenens-Johansson, Andrey Katrusha, Kyaw Soe Moe, Paul Johnson, and Wuyi Wang. Large colorless hpht-grown synthetic gem diamonds from new diamond technology, russia. *Gems & Gemology*, 51(3):260–279, 2015.

[176] Huijie Zheng, Georgios Chatzidrosos, Arne Wickenbrock, Lykourgos Bougas, Reinis Lazda, Andris Berzins, Florian Helmuth Gahbauer, Marcis Auzinsh, Ruvin Ferber, and Dmitry Budker. Level anti-crossing magnetometry with color centers in diamond. In *Slow Light, Fast Light, and Opto-Atomic Precision Metrology X*, volume 10119, pages 115–122. SPIE, 2017.

[177] Reinis Lazda, Laima Busaite, Andris Berzins, Janis Smits, Florian Gahbauer, Marcis Auzinsh, Dmitry Budker, and Ruvin Ferber. Cross-relaxation studies with optically detected magnetic resonances in nitrogen-vacancy centers in diamond in external magnetic field. *Phys. Rev. B*, 103:134104, Apr 2021.

[178] A. R. Abadal. *Calibration of an IQ mixer for continuous and pulsed modulation*. Semesterarbeit, Eidgenössische Technische Hochschule Zürich, 2014.